BUOYANCY DRIVEN FLOW

AND

METHANE HYDRATE SYSTEMS

By

DARRELL ANDREW TERRY

Bachelor of Science in Oceanography (Physical)
University of Washington
Seattle, Washington
1973

Master of Science in Aeronautics and Astronautics
University of Washington
Seattle, Washington
1976

Submitted to the Faculty of the
Graduate College of the
Oklahoma State University
in partial fulfillment of
the requirements for
the Degree of
DOCTOR OF PHILOSOPHY
May 2019

BUOYANCY DRIVEN FLOW

AND

METHANE HYDRATE SYSTEMS

Dissertation Approved:

Dr. Camelia C. Knapp

Dissertation Adviser

Dr. Priyank Jaiswal

Dr. James H. Knapp

Dr Runar Nygaard

Outside Member.

ACKNOWLEDGEMENTS

School of the Earth, Ocean, and Environment (SEOE)
University of South Carolina

Dr. Camelia C. Knapp, Chair
Dr. Warren T. Wood, Outside Member
Dr. Alicia Wilson
Dr. Tom Owens
Dr. James H. Knapp
Olga Nedorub, Dr. Olusoga Martins Akintunde, Erin Derrick, Craig Cunningham, John Ollman, David Herman, Khalid Almutairi, Ross Cao, Essam Saeid, Ali Aljanabi, and Dawod Almayahi
Elizabeth Yankovsky, Amanda Quigley Williams, and Gokce Astekin
Kelly Hamilton, Charlene Wilson-Profit, Jae Choi, and Stephanie Bradley
USC Library Staff and Interlibrary Loan
State of South Carolina
University of South Carolina

Boone Pickens School of Geology (BPSOG)
Oklahoma State University

Dr. Camelia C. Knapp, Chair
Dr. Runar Nygaard, Outside Member
Dr. Priyank Jaiswal
Dr. James H. Knapp
Dr. Warren T. Wood, Special Advisor
Dr. Mohamed Abdel-Salam, Graduate Program Advisor
Salman Abassi, Babak Shabani, Georgina Lukoczki, Jenny Meng, Luel Emishaw, Ross Cao, Estefanny Davalos Elizondo, Seyi Sholanki, Sabrina Halli, Alejandra Torres, Mary Tkach, and David Herman
Sandy Earls, Joan Ragland, and Tim Sickbert
Oklahoma State University, Alumni
Oklahoma State University

Three Very Special Thank You's

Gokce Astekin, Dr. Camelia C. Knapp, Dr. Mohamed Abdel-Salam

Name: DARRELL ANDREW TERRY

Date of Degree: MAY 2019

Title of Study: BUOYANCY DRIVEN FLOW AND METHANE HYDRATE SYSTEMS

Major Field: GEOLOGY (Marine Geophysics)

Abstract: Marine gas hydrates have been studied intensely for more than five decades under the assumption that deep ocean basins lack the methane necessary to generate significant volumes of gas hydrates. Contrary to this, the deep waters of the Aleutian Basin in the Bering Sea alone are estimated to contain globally significant volumes of methane in gaseous and hydrate forms in velocity-amplitude (VAMP) structures. After a brief introduction to hydrate stability and seismic data acquisition, the Dissertation is divided into four parts:

Part 1. A unified effective medium model is developed to incorporate the endpoints of perfectly smooth and infinitely rough sphere components, and allow partitioning between rough and smooth grains. We incorporate the unified model into the framework for gas hydrates in unconsolidated sediments using both pore-fluid and rock matrix configurations for grain placement. The model resolves conflicting results of previous investigation from the 2002 Mallik gas hydrates projects.

Part 2. Conventional semblance for seismic velocity analysis does not have the resolving power of subspace methods due to the inclusion of the noise-signal space in conventional semblance. After nearly three decades, subspace techniques still receive little use in seismic applications due to high computational costs. We develop an approach for seismic velocity spectra based on computing the temporal covariance data matrix as an intermediate step to efficiently compute the Eigenvectors of the spatial covariance data matrix.

Part 3. The use of single channel far offset seismic images is investigated for what appears to be a more reliable, cost-effective indicator for the presence of bottom simulating reflectors than traditional CDP processing or AVO analysis. This non-traditional approach is taken to be more relevant to gas hydrate imaging. Results indicate BSRs are more easily identifiable from single channel far offset seismic images than from traditional CDP displays.

Part 4. The Aleutian Basin, though atypical from the traditional model of marine gas hydrates, provides a unique opportunity to investigate the role of buoyancy driven flow in deep water sediments and marine gas hydrate deposits. Evidence of large subbottom "VAMP" structures, abundance of structures, and presence of bottom-simulating reflectors, suggest cellular convection within the Aleutian Basin. We provide a basic stability analysis to calculate the Rayleigh-Darcy number for methane in a porous medium heated from below.

TABLE OF CONTENTS

TABLE OF CONTENTS (Continued)

Chapter Page

LIST OF TABLES

Table Page

LIST OF FIGURES

Introduction

Figure Page

Chapter I: A Unified Effective Medium Model for Gas Hydrates in Sediments

Figure Page

LIST OF FIGURES (Continued)

Chapter II: Subspace Solutions for Seismic Velocity

Figure Page

Chapter III. Identification of Bottom Simulating Reflectors in Far Offset Seismic Images

Figure Page

Chapter IV. Stability Analysis of VAMP-Hydrate Systems in the Central Aleutian Basin

Figure Page

INTRODUCTION

PART I: MOTIVATION

Naturally occurring methane-hydrates have been the subject of study and interest since their prediction and discovery in the late 1960s. Over many decades it has been observed that marine gas hydrates are found in the shallow sediments in the deep ocean along continental margins, usually the upper reaches of the continental slopes. Though conditions exist for the formation of hydrates in the deep ocean basins, significant amounts of marine gas hydrates have not been expected to be found in deep ocean basins due to a general lack of methane availability. Contrary to this assertion are the velocity-amplitude anomaly (VAMP) structures found in the deep waters of the Bering Sea, and in particular, in the Aleutian and Bowers Basins at water depths greater than 3700 m (Scholl and Cooper, 1978; Rearic et al, 1988; Barth et al, 2006; 2009; Scholl et al, 2009).

Exploration in the Aleutian Basin began with the review of U.S. naval data in the 1960s and has progressed through several active campaigns of single and multi-channel seismic data collections, site observations during the Ocean Drilling Program, and

GLORIA sonar surveys of the ocean floor physiography and backscatter (Karl et al, 1996). More recently, a new set of multi-channel seismic lines were collected as part of the U. S. participation in the Extended Continental Shelf Project (Ng and Martinson, 2011; Scholl et al, 2012; Christeson and Barth, 2015)

Presence of bottom-simulating reflectors (BSR), evidence of the large and anomalous sub-bottom VAMP structures, and abundance of the structures, suggest methane resources in globally significant quantities just within the central Aleutian Basin (Barth et al, 2009; Scholl et al, 2009). Furthermore, long available measurements of heat flow show anomalous moderately high values throughout the Aleutian Basin and other basins of the Bering Sea (Foster, 1962; Watanabe et al, 1977; Cooper et al, 1987). Though the methane-hydrate structures of the Aleutian Basin are atypical from the traditional model of marine gas hydrates, the Aleutian Basin provides a unique opportunity to investigate the role of buoyancy-driven flow in the formation and distribution of marine gas hydrates. In this research we investigate buoyancy-stability calculations in the shallow sediments of a deep ocean basin to develop an understanding of the conditions and dynamics of the VAMP structures in the central Aleutian Basin.

The four chapters of this dissertation informally divide the dissertation into two parts, the first part being to build quantitative modeling tools. The first part, Chapters 1 and 2, encompasses mathematical topics in rock physics and velocity analysis. Chapter 1 specifically shows that the Dvorkin-Nur rough sphere model is mathematically identical the rough sphere endpoint of the Walton (1987) model, and proposes a unified effective medium model (Terry and Knapp, 2018, i.e. Chapter 1). In Chapter 2 we explore the use of Eigen/covariance approaches to calculate a semblance velocity map. We show the

temporal covariance data matrix can be used to efficiently compute the spatial covariance data matrix. Then using only the first Eigenvalue we can more precisely define the semblance velocity than with conventional semblance.

The second part, Chapters 3 and 4, describes topics related to the most recently acquired seismic data set to better understand the macro scale processes of bottom simulating reflectors (BSR) and velocity amplitude anomalies (VAMP). The latter two chapters are largely qualitative explorations of the most recently acquired multi-channel seismic data set from the central Aleutian Basin. The first of these, Chapter 3, proposes that single channel far offset image displays are more informative for identifying the presence of bottom simulating reflectors than the two most prevalently used techniques, the CDP stack and AVO analysis. The second, Chapter 4, explores the seismic imagery to identify patterns to the presence of BSRs to propose that cellular convection may be the mechanism that gives rise to the VAMP structures and determines their special distribution. This chapter also presents calculations of the Rayleigh number to show that the necessary condition is met; suggesting cellular convection is feasible, but certainly not confirmed.

In this subsection we explained our motivation. In the remaining sections we review kinetics of hydrate formation, the geology and geophysics of the study area of a recent seismic data collection MGL1111, provide an overview of the MGL1111 data set from the central Aleutian Basin of the Bering Sea, provide an introduction to the final products used in our analysis.

The four chapters of this dissertation are:

Chapter 1: A unified effective medium model for gas hydrates in sediments

Chapter 2: Subspace analysis for stacking velocity

Chapter 3: Identification of bottom simulating reflectors in far offset seismic images

Chapter 4: Stability analysis of VAMP-hydrate systems in the central Aleutian Basin

PART II: HYDRATE STABILITY

Gas hydrates are solid ice-like structures that contain CH_4 and other hydrocarbon gases in a water molecule cage. They are stable as solids at high pressure and low temperature conditions. Each solid volume of gas hydrate contains up to 164 volumes of gas when dissociated at standard temperature and pressure conditions. Gas hydrates are known to exist in 3 molecular structures, mostly commonly Types I and II, and sometimes in Type H (also called Type III). Gas hydrates are found in biogenic and thermogenic forms.

Hydrate Stability Conditions

Calculations for a hydrate stability curve are shown in Figure 1 based on Lu and Sultan (2008, eqn. 9). For reasons that are not fully understand the curve for pure water usually provides the match with actual in situ data. This formulation is in good agreement with calculations based on Sloan (1998). Another useful formulation, the Trebble-Bishnoi equation-of-state as provides an improved version of van der Walls type equation-of-state (Bishnoi et al, 1989).

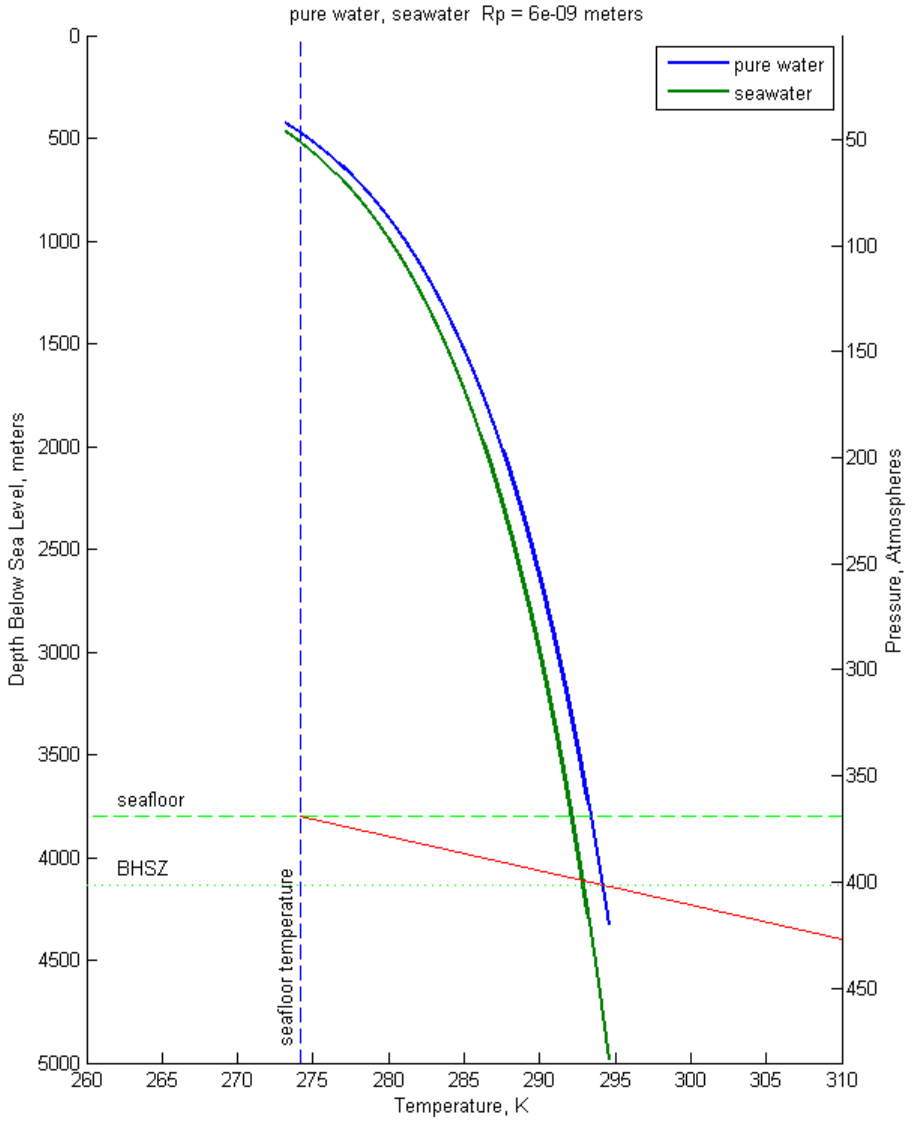

Figure 1. Hydrate stability curve for the central Aleutian Basin. Curves calculated from Lu and Sultan (2008, eqn. 9). Values are in agreement with other models (Sultan et al, 2004; Sloan, 1998).

Gas hydrate stability zone (GHSZ), or hydrate stability zone, refers to a zone between upper and lower depths at which methane clathrates naturally exist as a solid in the Earth's crust. In the case of marine gas hydrates, the upper boundary is usually the

ocean bottom, and the lower boundary is usually identified on seismic records as a bottom simulating reflector (BSR), a reflector with polarity reversed from the ocean bottom reflector.

Biogenic and Thermogenic Forms

Natural gas formed due to the transformation of organic matter by tiny microorganisms is referred to biogenic natural gas. Thermogenic natural gas originates as a result of chemical reactions that occur without the presence of microorganisms triggered by the application of extreme heat and pressure usually associated with formation of conventional oil and gas resources.

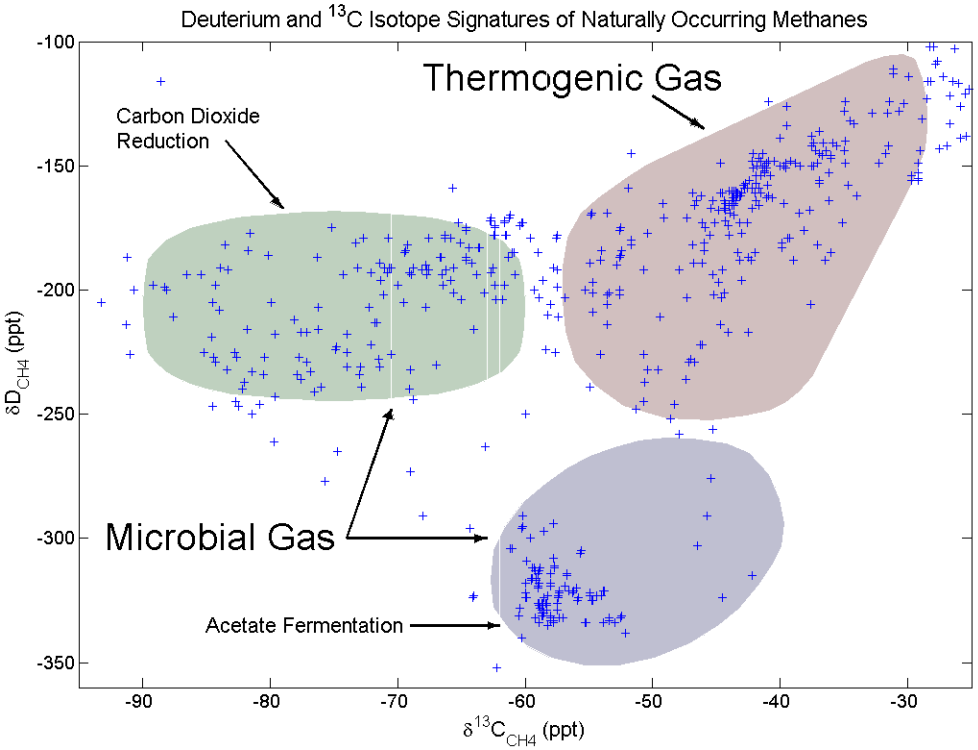

Figure 2. Deuterium and ^{13}C Isotope Signatures.

PART III: TECTONIC HISTORY OF THE BERING SEA AREA

As background we briefly describe the tectonic environment of the Bering Sea region (physiography, plate tectonic history, and heat flow measurements) and outline the seismic evidence for the presence of VAMP structures. Each contributes to our interest in multi-phase convective flow in porous media and motivates our hypothesis for this research.

Tectonic History

The Bering Sea encompasses a broad marginal sea to the north of the Aleutian Islands arc separating Alaska on the east from the Koryak Mountains and the Kamchatka Peninsula of Russian Siberia on the west (Figure 2). Geographically the Bering Sea is underlain by a broad continental shelf in the northern and northeastern parts of the Bering Sea contributing nearly half of the its surface area., and by three deep basins with a 3,200-3,400 m high escarpment on the northeast that separates the basins from the wide continental shelf and margin of North America off Alaska (Scholl et al, 1968). This marginal sea is bounded on the south by the Aleutian Islands, and by the Alaska Peninsula on the southeast.

The Bering Sea Basin is typical of other marginal basins surrounding the Pacific Ocean (Cooper et al, 1979). Sediments 2 to 9 km thick, mostly Cenozoic, are impounded behind an outer island arc represented by the Aleutian Ridge. Though the overlying sedimentary deposits are predominantly continental, the geologic and geophysical data suggest the crustal structure is oceanic and may have been part of the North Pacific Ocean prior to the Late Mesozoic, 60 to 70 Ma (Cooper et al, 1979). The tectonic history

of the Bering Sea results from evolution of the oceanic and continental plates encompassing and surrounding the North Pacific over the past 100 million years (Shor, 1964; Atwater, 1970; Byrne, 1979; Cooper et al, 1977, 1979, 1992; Rea and Dixon, 1983; Wallace and Engebretson, 1984; Engebretson et al, 1984).

The Bering Sea encompasses a broad marginal sea to the north of the Aleutian Islands arc separating Alaska on the east from the Koryak Mountains and the Kamchatka Peninsula of Russian Siberia on the west (Figure 3). Geographically the Bering Sea is underlain by a broad continental shelf in the northern and northeastern parts of the Bering Sea contributing nearly half of the its surface area., and by three deep basins with a 3,200-3,400 m high escarpment on the northeast that separates the basins from the wide continental shelf and margin of North America off Alaska (Scholl et al, 1968). This marginal sea is bounded on the south by the Aleutian Islands, and by the Alaska Peninsula on the southeast. One of the first extensive studies (Scholl et al, 1968) used published Russian charts, and unpublished and published studies from the U.S. Coast and Geodetic Survey and the U.S. Naval Oceanographic Office. These early studies focused on the continental shelf and margin areas.

Physiography

The deep water of the Bering Sea is divided into three physiographic areas; Aleutian, Bowers, and Komandorsky Basins (Scholl et al, 1975). During the mid-1970s the U. S. Geological Survey conducted surveys for resource potential, and found concentrations of methane and potential for hydrocarbon production if sufficiently high heat flow and sediment thicknesses (Cooper et al, 1979) are present. The three deep basins are separated by two aseismic ridges. Shown in Figure 3, Bowers Ridge loops

north from the Aleutian Ridge, and Shirshov Ridge juts southward from the Siberian mainland (Scholl et al, 1975).

The Beringian continental margin sweeps in a 2,400-km long arc from Cape Kamchatka to the tip of the Alaska Peninsula, and separates the deep basins from the shelves of the Bering Sea (Scholl et al, 1975) with a drop off of greater than 2000 m. A more complete description of the submerged physiography of this vast area is found in several publications including Nichols and Perry (1966). Karl et al (1996) provides a detailed analysis of the GLORIA imagery and the 3.5 kHz seismic reflection data, revealing that the deep expanse of the Aleutian basin is very flat and featureless. The Bering Sea Basin is typical of other marginal basins surrounding the Pacific Ocean (Cooper et al, 1979). Sediments 2 to 9 km thick, mostly Cenozoic, are impounded behind an outer island arc represented by the Aleutian Ridge (Figure 3). Though the overlying sedimentary deposits are predominantly continental, the geologic and geophysical data

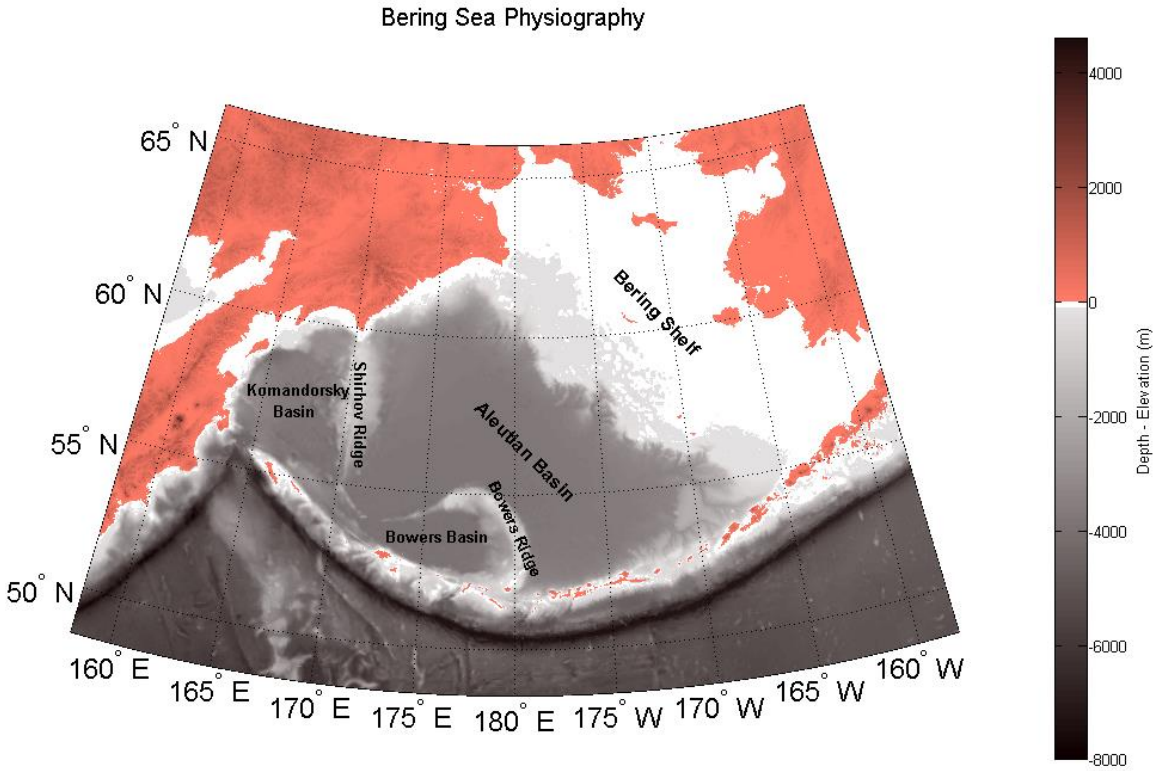

Figure 3. General index map of Bering Sea basin and the Bering Shelf. Based on Scholl and Cooper (1978).

suggest the crustal structure is oceanic and may have been part of the North Pacific Ocean prior to the Late Mesozoic, 60 to 70 Ma (Cooper et al, 1979).

Tectonics

The tectonic history of the Bering Sea results from evolution of the oceanic and continental plates encompassing and surrounding the North Pacific over the past 100 million years (Shor, 1964; Cooper et al, 1987; Wallace and Engebretson, 1984; Engebretson et al, 1984). Backward reconstructions have been used to estimate the age, original size, and past movement of the paleo Kula Plate (Atwater, 1970; DeLong, et al, 1978; Byrne, 1979; Rea and Dixon, 1983; Lonsdale, 1988). A remnant of this plate likely forms the igneous basement of the deep Aleutian and Bowers Basins of the Bering Sea (Marlow and Cooper, 1983). The Kula Plate, believed to have originated 90 to 80 Ma from splitting of the old Farallon Plate, covered a large extent of the North Pacific Ocean. Motion of this paleo Kula Plate was generally to the north with subduction along the North American coast that included British Columbia, southern Alaska, and the Beringian continental margin (Alaskan and Russia). A spreading ridge separated the Kula Plate from the Pacific Plate; however, the boundary with the Farallon Plate has not been well defined.

With the end of the Mesozoic (60 Ma), initial development of the Aleutian Ridge fractured the Kula Plate (Cooper et al, 1979). At about 56 to 55 Ma the Kula Plate subduction jumped from the Alaskan and Russian continental margins to the Aleutian Arc (Scholl et al, 1983, 1989), thereby trapping part of the Kula Plate to the north of the new arc (Marlow and Cooper, 1983). Cooper et al (1992) postulates that during this period of major Kula-Farallon-Pacific plate reorganization (Lonsdale, 1988) further

regional extension initiated volcanism and seafloor spreading in the Aleutian Basin. This may include growth of the Bowers and Shirshov (Figure 3) submarine ridges within the Bering Sea Basin. A large shift in the direction of the Pacific plate motion at 42 MA seemingly had a major impact on the Aleutian/Bering Sea region. At 40 Ma the Kula Plate became part of the Pacific Plate. Sediments, largely terrigenous, have been continuously delivered to the Aleutian and Bowers Basins since the Late Mesozoic; the sedimentary record is largely flat-lying (Cooper et al, 1979). Various problems and alternative solutions to this model are offered in Scholl et al (1975).

Heat Flow

Several heat flow measurements (Cooper et al, 1979) have been reported from the Bering Sea Basin (Foster, 1962; Erickson, 1973; Watanabe et al, 1977; Marshall et al, 1978). Watanabe et al, (1977) reported heat flow values for the Aleutian Basin. Cooper et al (1977) correlated high heat flow measurements with broad magnetic anomalies in the central and eastern Aleutian Basin, and attributes their presence to the higher subcrustal temperatures.

Observed heat flow values in the Aleutian Basin are moderately high with an average value of 1.44$\pm$ microcal.sq m/sec (Cooper et al, 1979; Watanabe et al, 1977). Thermal conductivity is given to be 2.5 mcal/sec/deg C (Erickson, 1973). A thermal gradient at 58 deg C/km is sufficient to reach onset of hydrocarbon generation at shallow sub-bottom depths of 0.9 to 1.9 km. Because the sediment thickness in the Aleutian Basin ranges from 2 to 9 km, temperatures suitable for biogenic and thermogenic degradation of organic matter may be found throughout the basin (Cooper et al 1979).

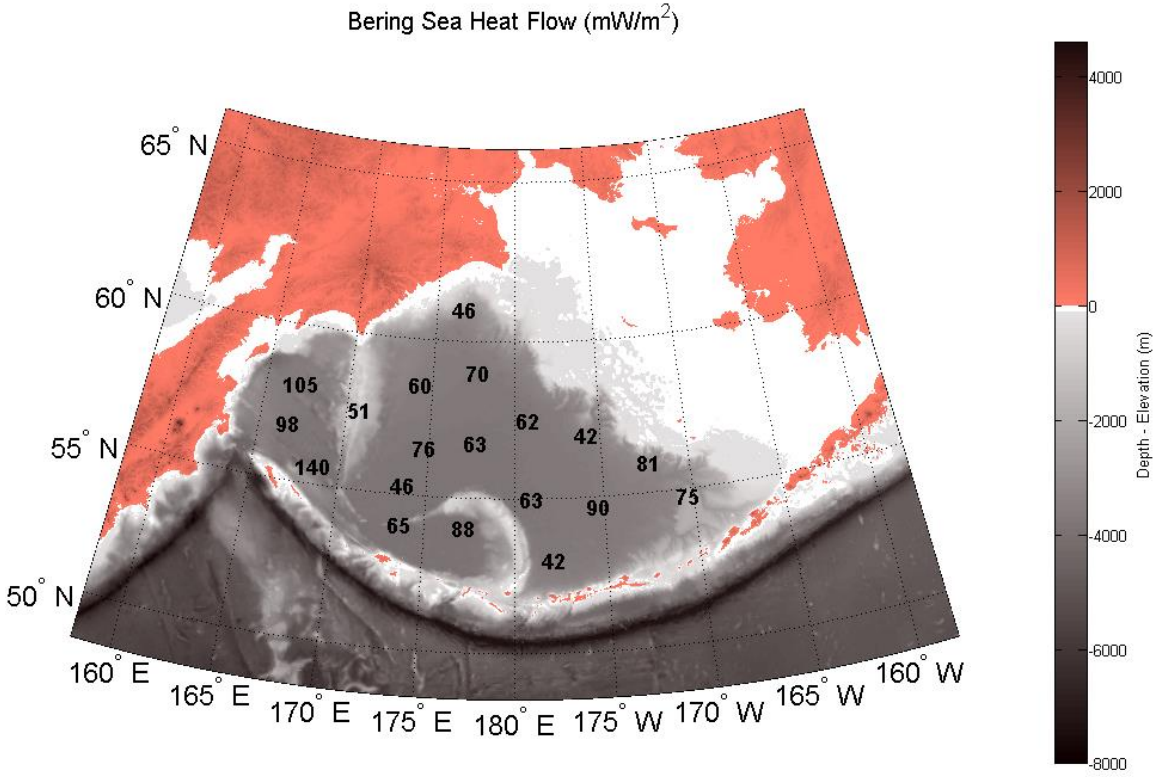

Figure 4. Heat flow map of the Bering Sea basin after Scholl et al (2009).

Corrected heat flow values and their associated thermal gradients are estimated to be 20 to 25 percent larger (Cooper et al, 1977).

Seismic Evidence of Plume Structures

Velocity amplitude anomaly (VAMP) structures have been well known in the central Aleutian Basin of the Bering Sea for a long time (Scholl and Hart, 1993). Scholl and Cooper (1978) first identified the association of velocity anomalies and high amplitude reflections in the Bering Sea basins (in data from the U. S. Naval Oceanographic Office collected in 1972) and offered speculation about their origin and geologic significance. The velocity amplitude anomalies were identified as columns of push-down concave reflections below a regionally extensive bottom simulating reflector (BSR) in association with one or more high amplitude reflections recorded up to 100 m above the BSR in the sediment column; the latter is sometimes referred to as a seismic pull-up in contrast to the former being referred to as seismic push-down. For brevity Scholl and Cooper (1978) have referred to these velocity-anomaly and reflection-amplitude associations as VAMPs.

It is believed the chimney structures transport low-velocity, gas-charged fluids toward the sea floor; and are responsible for the widespread recording of VAMP structures in the Bering Sea Basin (Scholl et al, 2009). The U. S. Navy profiles established the common association of domed (or arched) reflections, phase inverted high-amplitude reflection horizons, and an underlying column of down-bowed concave reflections as distinct structures (Scholl and Cooper, 1978).

The source of the thermogenic gas to support the VAMP structures is speculated to be local pooling at sub-bottom depths of 800 to 1000 meters (Scholl and Stevenson,

1990). The known concentration of VAMPs is greatest beneath the Bering Abyssal Plain that occupies the central region of the Aleutian Basin (Scholl and Cooper, 1978). The central basin's sedimentary section is regionally thinnest, typically 2 to 4 km thick, whereas along the perimeter the section is 4 to 8 km thick (Scholl and Cooper, 1978). The sedimentary section is speculated to overly a basaltic oceanic crust of Early Cretaceous age (Scholl and Cooper, 1978). Prior to 1977, more than 350 VAMPs were identified on single- and 24-fold reflection seismic profiles (Scholl and Cooper, 1978). Today nearly 1000 VAMPs have been mapped with more than 12,000 estimated to exit (Rearic et al, 1988; Scholl et al, 2009). What is commonly now believed to be a gas hydrate associated BSR at a two-way time between 0.45 and 0.50 seconds (equal to sub-bottom depth of 400 m) identifies the depth of the apparent structural relief topping a chimney with seismic push-downs. Many of the VAMP structures are associated with basement highs.

A second conspicuous change in reflection character, that mimics the contour of the overlying sea floor, is identified by Scholl and Creager (1973) and Hein et al (1978). Seismically, also, identified as a BSR (Scholl et al, 2009), this represents a diagenetic boundary, resulting from dissolution of biogenic silica (opal-A) and re-precipitation of crystalline silica (opal-CT). This diagenetic boundary is marked by a distinct decrease in both porosity and permeability (Lee, 1973). At ODP Site 188, porosity drops from 58 percent to 32 percent and the permeability decreases from 35 to 0.1 (Creager et al, 1973). The lateral continuity of the diagenetically altered mudstone unit in the Aleutian basin may regionally restrict upward migration of deeply buried thermo-catalytic hydrocarbons. More detailed definitions of the major types of BSRs are found in Berndt et al (2004).

PART IV: ACQUISITION OF SEISMIC DATA IN THE CENTRAL ALEUTIAN BASIN

Multi-channel seismic data was recently acquired from the central Aleutian Basin as part of the third round of the Law-of-the-Sea Treaty. In this section we discuss the acquisition and pre-processing of the seismic data. Then we discuss our motivation for investigating single channel seismic images and how to display the data for maximum definition of the geological structures in the data. This data set was first described in Scholl et al (2012). Subsequently, multi-channel CDP processing of the seismic data are described in Christeson and Barth (2015) and Yankovsky et al (2015).

The area of this study encompasses the central Aleutian Basin of the Bering Sea. The box of the inset to Figure 2 outlines this area and the main figure shows the ship tracks for the fifteen multi-channel seismic lines of MGL1111. Collection of the data in August 2011 was part of the U. S. Extended Continental Shelf Project. MGL1111 was designed to use marine geophysics in the Gulf of Alaska to determine geologic framework, including crustal nature and sediment thickness within and beyond the U.S. Exclusive Economic Zone, from the 2000 m isobath to 350 nm from the territorial baselines.

More specifically, the collection of multi-channel seismic data from the central Aleutian Basin was designed to investigate plume structures in the enclosed abyssal basin. Though the plume structures were originally identified in sonar records in the mid 1960s, and though there are believed to be more than 12,000 plume structures in the area, the region remains largely unexplored. Studies and speculation lead to a tentative

conclusion that the plumes are of thermogenic origin with the basin filled with sediments having thicknesses from 4 to 12 km.

Seismic Data Acquisition

The MCS1111 data was collected aboard the R/V Marcus G. Langseth. The main features of the acquisition included an 8,000 meter hydrophone array with 636 channels on a 12.5 meter spacing. The source airgun array of 6,600 cu. in. volume was fired at 2,000 psi every 50 meters. Source offset from first receiver group was 162 m; water .

Location and Description of Seismic Data

The multi-channel seismic data, along with additional geophysical data sets, were acquired in August 2011 aboard the R/V Marcus G. Langseth expedition MGL1111. The area of our study encompasses the central Aleutian Basin of the Bering Sea. The box of Figure 5 (a) outlines the survey area within the Bering Sea and the Figure 5 (b) shows the ship tracks for the fifteen multi-channel seismic lines of MGL1111. This data, and the gravity and magnetic data to also be used in the study, were collected in August 2011 as part of the Extended Continental Shelf Project. The main features of the acquisition included an 8,000 meter hydrophone array with 636 channels with 12.5 meter spacing and an airgun array of 6100 cu. in. volume fired at 2,000 psi every 50 meters. See Table I for a summary of the acquisition parameters and Table II for a summary of the multi-channel seismic lines.

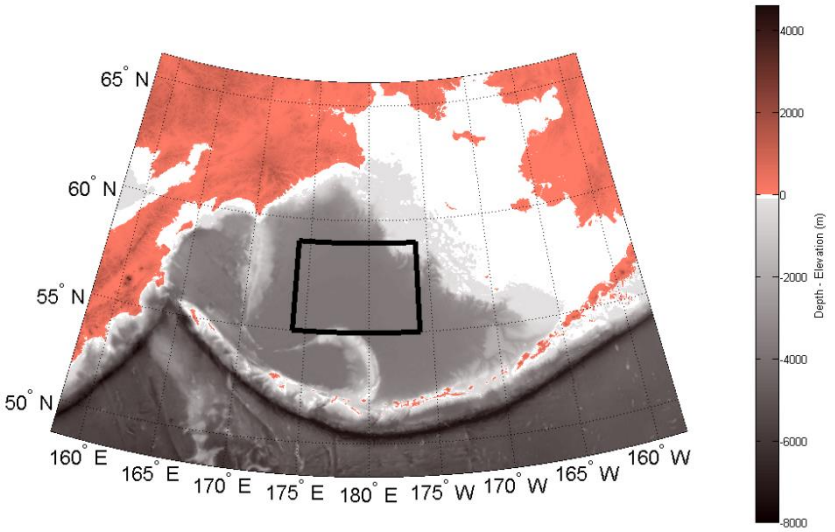

a)

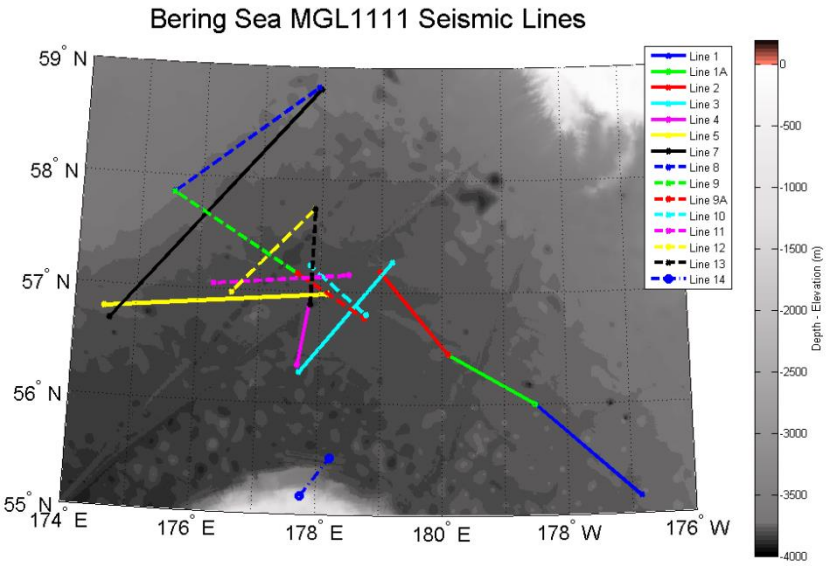

b)

Figure 5. Bathymetric map of the central Aleutian Basin with tracks for the newly acquired seismic lines. Bathymetry, update V15.1, courtesy of the Global Topography Project, University of California at San Diego; MGL1111 tracks courtesy of U. S. Geological Survey and Marine Geoscience Data System, LDEO, Columbia U.

depths varied near 3,800 m except for MCS14. Specific details of the configuration are found in the cruise reports (Ng and Martinson, 2011).

Targets of interest range from the ocean bottom down to a two-way travel time of 6,100 ms, approximately 1 sec below the ocean bottom. At an average velocity of 1,500 m/sec, this is another 750 m depth from the ocean surface, or total depth of 4,550 m.

The Third Round for implementing the Law of the Sea Treaty has prompted the U. S. State Department to scientifically support claims to additional undersea areas. Pertinent to this, under sponsorship of the U. S. State Department, the U. S. Geological Survey with additional support from the Naval Research Laboratory acquired multi-channel seismic lines in the central Aleutian Basin.

TABLE I. Acquisition Parameters, Bering Sea Seismic Data, MGL1111, August 2011

Acquisition Data::			
Platform Name	R/V Marcus G. Langseth		
Acquisition Parameters:		Receiver Parameters:	
Acquisition Parameter Name	MGL1111_ACQ0011	Receiver Type	Hydrophone Receiver
Survey Datum		Receiver Make/Model	NA/NA
Shot Interval (meters)		Number of Channels	636
Sample Interval (microseconds)		Cable Length (meters)	7050
Record Length (seconds)		Cable Depth (meters)	9
		Group Spacing (meters)	12.5
Source Parameters:		Source to Near Channel (meters)	162
Source Type	Air Gun		
Source Male/Model	BOLT/Bolt		
Source Volume (cu in)	6600		
Source Pressure (psi)	2000		
Source Depth (meters)	9		
Source of data: Marine Geoscience Data System (MGDS), Lamont Doherty Earth Observatory, Columbia University			
Telephone: 1-845-365-8895			
e-mail: infoo@marine-geo.org			
Expedition: MGL1111			
Chief Scientist: Ginger Barth, U. S. Geological Survey, Menlo Park, California			
Co-Chief Scientist: Warren Wood, NRL, Stennis Space Center, Mississippi			

TABLE II. Summary of Multichannel Seismic Lines, MGL1111

Seq. Number	Line Number	Reels	Shot Points (SP)	No. of SPs	Unnumb. SPs	Missing SPs
1	MCS01	1-6	719-3505	2787	---	---
2	MCS01A	7-11	1007-3006	2000	1255,1546	---
3	MCS02	12-16	1009-3139	2131	3055,3060-3061	---
4	MCS03	17-22	689-3563	2875	---	---
5	MCS04	23-26	1089-2589	1501	1575-1578,1616-1620	---
6	TRN05	27	1053-1351	299 (290)	1254,1263-1264, 1351	1074-1082
7	MCS05	28-37	843-5296	4454	962-963,1014-1017	---
8	MCS07	38-50	926-7099	6174 (6171)	959,965-966,983-985,4674,4681-4684,7055,7099	3180,3182,3673
9	MCS08	51-58	1464-4992	3529	1600,1824,1825, 1835,2830	---
10	MCS09	59-65	1036-3965	2930 (2911)	1228-1229,1693 1st 1630 = 1629	1627,1275-1292
11	MCS09A	66-69	1012-2617	1606	---	---
12	MCS10	70-73	905-2379	1475	1108,1159,1160	---
13	TRN11	75-76	996-1809	814	---	---
14	MCS11	77-82	920-3626	2707	2620-2622,2669-2670	---
15	TRN12	83	1011-1377	367	---	---
16	MCS12	84-88	971-3314	2344	---	---
17	MCS13	89-92	1089-2985	1897 (1889)	1099,1175-1177	1218-1225
22	MCS14	93-95	908-1877	970	---	---

PART V: PROCESSING AND ANALYSIS OF SEISMIC DATA

Any seismic data set contains a huge amount of information that is underutilized. Our motivation is to extract as much information and better understand the information content of the full data set. The seismic data from MGL1111 has been processed at three different sites for high resolution velocity analysis (U.S. NRL), CDP stacking (U.S. Geological Survey), and single channel, far offset seismic images (USC/OSU). An overview is provided below for each effort.

High Resolution Velocity Analysis (NRL)

Dr. Warren Wood at the Naval Research Laboratory at the Stennis Space Center, Mississippi constructed a high resolution velocity analysis time section for the Cyrano VAMP on MCS01 (Scholl et al, 2012).

CDP Processing and Stacking (USGS and University of Texas Institute for Geophysics)

The seismic reflection data acquired during cruise MGL1111in the central Aleutian Basin is shown in Christeson and Barth (2015). The CDP stacked data is publically available from Academic Seismic Portal at the University of Texas, Institute of Geophysics (Sliter et al, 2011).

Review of Single Channel Imagery

Seismic Common Depth-Point (CDP) processing has been extensively developed over more than six decades, and with current 3D acquisition systems and post-acquisition processing, is integrated across exploration and production environments. Seismic CDP processing led many of the developments in multi-channel signal processing yet does not take full advantage of the information content of seismic data available from modern state-

of-the-art acquisition systems. New concepts that are more objective in approach, based on phenomenology and truly multichannel, are needed to address the increasing exploration demands of large seismic data sets and more subtle target objectives.

Current CDP processing is designed to locate traditional hydrocarbon resources. Deficiencies of traditional CDP processing include use of small offset angles to facilitate stacking. The stacking processing itself may introduce artifacts in the resulting image. In addition, AVO analysis, as discussed above, may require difficult to apply corrections that may further complicate the analysis. Our processing approach discussed below tries to minimize the effect of these issues by using the furthest offset angles available and minimizing any signal processing that could introduce artifacts into the seismic image.

Our targets are shallower than commercial objectives, and the quest for understanding the information content is much broader. As shown below, angle offsets are much greater for the targets of our interest. An angle of 30.0 degrees is met at offset 162 m plus 2032 m of the receiver array for a depth of 3,800 m and at offset 162 m plus 2,465 m of the receiver array for a depth of 4,550 m. Assume an average water depth of 3,800 m, the near offset has an angle of approximately 2.44 degrees; the far offset has an angle of approximately 64.90 degrees for a depth of 4,550. Assume an average target depth of 4,550 m, the near offset has an angle of approximately 2.04 degrees; the far offset has an angle of approximately 60.71 degrees. Before focusing on the application, we make a detour to understand how the data was pre-processed from the field data.

Pre-processing. The MGL1111 seismic data was recorded in SEGD format with the navigation data in P190 format. We downloaded the data sets from the Marine Geoscience Data System hosted at Lamont-Doherty Earth Observatory of Columbia University (Barth et

al, 2011). Additional details and notes are available in the documentation by Ng and Martinson (2011). Upon receipt the seismic and navigation data sets were merged and converted to SEGY format. The data consists of 15 multi-channel seismic lines as shown in Figure 5 and Table II.

Processing approach. For initial review we generated single channel seismic images for the nearest and farthest offset channels. For display we applied a wide bandpass filter to remove cable noise for displays of both the single channel seismic sections and the shot gathers. In all displays of the seismic data below we use a linear gray scale clipped at ± 7.0. This value was chosen to provide the greatest definition of the stratigraphic structures recognized in the data sets. Negative and positive clippings are displayed with yellow and red, respectively. This choice for the clipping value has been very fortuitous to define major horizontal layer boundaries and the BSRs.

Display of Seismic Images

Though qualitative rather than quantitative, the visual display of seismic data is an important source of geological and geophysical information. Here we provide visual displays of 2D seismic lines from MGL1111 and discuss the insight these images provide. In this section we provide comment on visual display of the 2D seismic lines from MGL1111 lines. Since the streamer cable has 636 receiver groups potentially 636 single channel images could be produced for each 2D seismic line. For this demonstration we have chosen to focus on the near offset (Channel 636) and the far offset (Channel 1). This has proven useful for improved identification of bottom simulating reflectors. Each seismic image is displayed as a 2,000 ms window starting just above the water bottom. For the near offset images, the window starts at 5,000 ms. The window starts at 7,000 ms for the far offset

images to account for the longer travel time. Max and min seismic amplitude values ± 7.0 are chosen for display to provide maximum definition of the local features, and to color the largest absolute values; yellow is chosen for the largest negative values and red for the largest positive values. In the single channel seismic displays, the near offset (Channel 636) and far offset (Channel 1) midpoints are offset, or shifted, from each other by a distance that corresponds to 79 shotgathers.

The result or conclusion has been to recognize that much information content can be lost when CDP processing is applied to assess presence of bottom simulating reflectors. With much surprise these single channel seismic images may prove to be a valuable tool for reconnaissance to detect the presence of methane hydrates.

REFERENCES

Atwater T. 1970. Implications of plate tectonics for the Cenozoic tectonic evolution of western North America. Geological Society of America Bulletin. 81, 3513-3536.

Barth G., Childs J. and Wood, W., 2013. Multi-Channel Seismic Shot Data from the Bering Sea acquired during the R/V Marcus G. Langseth expedition MGL1111 (2011). Interdisciplinary Earth Data Alliance (IEDA). doi:10.1594/IEDA/318037.

Barth G. A., Scholl D. W. and Childs J. R.; 2006. Possible deep-water gas hydrate accumulations in the Bering Sea. Fire in the Ice, Methane Hydrate Newsletter 6, (3), 10-11.

Barth G. A., Scholl D. W. and Childs J. R., 2009. Bering Sea Velocity-amplitude anomalies: Exploring the distribution of natural gas and gas-hydrate indicators. In: Natural Gas Hydrates – Energy Resource Potential and Associated Geologic Hazards, American

Association of Petroleum Geologists Memoir, Vol. 89 (ed. T. Collett, A. Johnson, C. Knapp and R. Boswell), pp. 324-349.

Berndt C., Bunz S., Clayton T., Mienert J. and Saunders M. 2004. Seismic character of bottom simulating reflectors: examples from the mid-Norwegian margin. Marine and Petroleum Geology 21, 723-733.

Bishnoi P. R., Gupta A. K., Englezos P., and Kalogerakis N., 1989. Multiphase equilibrium flash calculations for systems containing gas hydrates. Fluid Phase Equilibria. 53, 97-104.

Byrne T., 1979. Late Paleocene demise of the Kula-Pacific spreading center. Geology 7, (7), 341-344.

Christeson G. L. and Barth G. A., 2015. Aleutian basin oceanic crust. Earth and Planetary Science Letters 426, 167-175

Cooper A. K., Marlow M.S. and Scholl D.W., 1977. The Bering Sea – A multifarious marginal basin. In: Island Arcs, Deep Sea Trenches and Back-Arc Basins, (ed. M. Talwani and W. C. Pitman), American Geophysical Union, pp. 437-450.

Cooper A. K., Marlow M. S. and Scholl D. W., 1987. Geologic framework of the Bering Sea crust (Chapter Five). Geology and Resource Potential of the Western North America and Adjacent Ocean basins – Beaufort Sea to Baja California, Circum.-Pacific Council for Energy and Mineral Resources, pp. 73-102.

Cooper A. K., Marlow M. S., Scholl D. W. and Stevenson, A. J., 1992. Evidence for Cenozoic crustal extension in the Bering Sea region. Tectonics 11 (4), 719-731.

Cooper A. K., Scholl D. W., Marlow M. S., Childs J.R., Redden G. D., Kvenvolden K. A. and Stevenson A. J., 1979. Hydrocarbon potential of Aleutian Basin, Bering Sea. American Association of Petroleum Geologists Bulletin 63 (11), 2070-2087.

Engebretson D. C., Cox, A. and Gordon, R. G., 1984. Relative Motions Between Oceanic Plates of the Pacific Basin. Journal of Geophysical Research 89, (B12), 10291-10310.

Foster T. D., 1962. Heat-flow measurements in the Northeast Pacific and in the Bering Sea. Journal of Geophysical Research 67, (7), 2991-2993.

Hein J. R., Scholl D. W., Barron J. A., Jones M. G. and Miller J., 1978. Diagenesis of Late Cenozoic diatomaceous deposits and formation of the bottom simulating reflector in the southern Bering Sea. Sedimentology 25, (2), 155-181.

Ng D. and Martinson D., 2011. RV Langseth Data Reduction Summary, MGL1111, Dutch Harbor, AK – Dutch Harbor, AK, Not Final, V1.2, 2011-09-02. Lamont Doherty Earth Observatory, Columbia University, 64 pp, +5 Appendices.

Karl H. A., Carlson P. R. and Gardner, J. V., 1996. Aleutian Basin of the Bering Sea. In: Geology of the United States Seafloor: The View from Gloria. (ed. J. V. Gardner, M. E. Field and D. C. Twichell), Cambridge University Press, 374 pp.

Lee H. J., 1973. Measurements and estimates of engineering and other physical properties, Leg 19. Initial Reports of the Deep Sea Drilling Project, Vol. 19. U. S. Government Printing Office, pp. 701-719.

Lonsdale, P., 1988. Paleogene history of the Kula plate: Offshore evidence and onshore implications. *Geol. Soc. Amer. Bull.*, v 100, n. 5, p. 733-754.

Lu Z. and Sultan N., 2008. Empirical expressions for gas hydrate stability law, its volume fraction and mass-density at temperatures 273.15K to 290.15 K. Geochemical J. 42, (2), 163-175.

Marshall V. B., Cooper, A. K. and Childs J. R., 1978. Recent heat flow measurements in the Aleutian basin, Bering Sea (abs). *EOS Trans*., v. 59, p. 384.

Nichols H. and Perry R. B., 1966. Bathymetry of the Aleutian arc, Alaska. U. S. Dept. Commerce, Environmental Sci. Services Admin., Coast and Geod. Survey, Mon. 3, scale 1:400,000, 6 maps.

Rea D.K. and Dixon J.M., 1983. Late Cretaceous and Paleogene tectonic evolution of the North Pacific Ocean. Earth and Planetary Science Letters 65, (1), 145-166.

Rearic D.M., Williams S.R., Carson P.R. and Hall R.K., 1988. Acoustic evidence for gas-charged sediment in the abyssal Aleutian Basin, Bering Sea, Alaska. Department of the Interior, U. S. Geological Survey, Open-File Report 88-577.

Scholl D.W., Barth G.A. and Childs J.R., 2009. Why hydrate-linked velocity-anomaly structures are common in the Bering Sea Basin: A hypothesis. In: Natural Gas Hydrates – Energy Resource Potential and Associated Geologic Hazards, American Association of Petroleum Geologists Memoir, Vol. 89 (ed. T. Collett, A. Johnson, C. Knapp and R. Boswell), pp. 308-323.

Scholl D. W., Buffington E. C. and Hopkins D. M.; 1968. Geologic history of the continental margin of North America in the Bering Sea. Marine Geology 6, 297-330.

Scholl D. W. and Cooper A. K., 1978. VAMPs – Possible hydrocarbon-bearing structures in Bering Sea basin. American Association of Petroleum Geologists Bulletin 62 (12), 2481-2488.

Scholl D. W. and Creager J. S., 1973. Geologic synthesis of Leg 19 (DSDP); Far North Pacific, and Aleutian Ridge, and Bering Sea. Initial Reports of the Deep Sea Drilling Project, Vol. 19. U. S. Government Printing Office, pp. 897-913.

Scholl D. W. and Hart P. E., 1993. Velocity and amplitude structures on seismic-reflection profiles – Possible massive gas-hydrate deposits und underlying gas accumulations in the Bering Sea Basin. In: The Future of Energy Gases, Professional Paper 1570 (ed. D. G. Howell), pp. 331-351, U. S. Geological Survey.

Scholl D. W. and Stevenson A. J., 1990. Was the Aleutian Basin more enclosed, its deeps oxygen deficient, and the geothermal gradient steepened in the Middle Tertiary? Implications for the petroleum potential of the Bering Sea (abs). Fifth Circum-Pacific Energy and Mineral Resources Conference, Honolulu, HI, 29 July-3 August 1990, p. 1000.

Shor G.G., 1964. Structure of the Bering Sea and the Aleutian Ridge. Marine Geology 1, 213-219.

Sliter R., Barth G., Wood W. T. and Childs, J., 2011. Processed multi-channel seismic data in the Bering Sea acquired during R/V Marcus G. Langseth expedition MGL1111 (2011). Academic Seismic Portal at UTIG, Marine Geoscience Data System. http://dx.doi.org/10.1594/IEDA/500056

Sloan Jr. E. D., 1998. Clathrate Hydrates of Natural Gases, Second. Marcel Dekker.

Sultan N, Foucher J. P., Cochonat P., Tonnerre T., Bourillet J. F., Ondreas H., Cauquil E. and Grauls D., 2004. Dynamics of gas hydrate: case of the Congo continental slope. Marine Geology 206, 1-18.

Terry D. A. and Knapp, C. C.; 2018. A Unified Effective Medium Model for Gas Hydrates in Sediments. Geophysics, 83 (6), MR317–MR332, 13 Figures, 1 Table.

Wallace W.K. and Engebretson D.C. 1984. Relationships between plate motions and Late Cretaceous to Paleogene magmatism in southwestern Alaska. Tectonics 3, (2), 295-315.

Walton K., 1987. The effective elastic moduli of a random packing of spheres: Journal of the Mechanics and Physics of Solids, **35**, 213-226.

Watanabe T., Langseth M. G. and Anderson R. N., 1977. Heat flow in back-arc basins of the western Pacific. In: Island Arcs, Deep Sea Trenches and Back-Arc Basins (ed. M Talwani and W. C. Pitman), American Geophysical Union, pp. 137-161.

Yankovsky E. A., Terry D. A. and Knapp C. C., 2015. Seismic and gravity evidence for methane-hydrate systems in the central Aleutian Basin. International Journal of Earth Science and Geophysics 1 (1), 1-8.

CHAPTER I

A UNIFIED EFFECTIVE MEDIUM MODEL FOR GAS HYDRATES IN SEDIMENTS

Terry, Darrell A.; Knapp, Camelia C.; 2018. A Unified Effective Medium Model for Gas Hydrates in Sediments. Geophysics, 83 (6), MR317–MR332, 13 Figures, 1 Table.

Accepted: 24 July 2018

This paper is an expansion of an Extended Abstract presented at the 2018 SEG Rock Physics and Digital Rock Application Workshop, 22-23 May 2018, Beijing, China.

ABSTRACT

A unified effective medium model is developed to incorporate the endpoints of perfectly smooth and infinitely rough sphere components, and allow partitioning between rough and smooth grains. We incorporate the unified model into the framework for gas hydrates in unconsolidated sediments using both pore-fluid and rock matrix configurations for grain placement while reviewing other developments that have taken place in the last four decades. The unified rock matrix model is validated with data available from the 2002 Mallik gas hydrates project well 5L-38. Gas hydrate saturation and neutron porosity logs from this well are used to generate synthetic compressional and

shear wave velocity models for several values of the friction coefficient. First, we overlaid crossplots of compressional versus shear wave velocities for synthetic and measured velocities, and compared the match until a good choice was found for the friction coefficient. Second, we plot the synthetic velocities as separate logs of compressional and shear wave velocities for each friction coefficient; the synthetic velocity logs were then overlaid on the measured velocities calculated from the sonic logs. Results of a direct comparison of the synthetic and measured velocity logs provided valuable insights into the validation of the unified effective medium model. Recognizing the significance of the Hertz-Mindlin type effective medium models for gas hydrates in unconsolidated sediments, we incorporate the previous efforts into a single "unified" model and define a common nomenclature. Though we attempted to assign a single friction coefficient value to each Hydrate Window, it is not surprising that in a real and heterogeneous environment the value might vary with depth as it does here at the larger spatial scales. Here we demonstrate and quantitatively estimate that gas hydrates in sediments are well predicted with a friction coefficient closer to a smooth sphere model than a rough sphere model.

KEYWORDS: rock physics, algorithm, modeling, bulk modulus, shear modulus, gas hydrates

1.1 INTRODUCTION

Hertz-Mindlin theory (Mindlin, 1949; Brandt, 1955; Duffy and Mindlin, 1957; Deresiewicz, 1958) is frequently referenced as underlying various versions of effective medium models for unconsolidated rocks in the past thirty years (Digby, 1981; Walton,

1978, 1987; Dvorkin and Nur, 1996; Helgerud, 2001; Jenkins et al, 2005). Understanding development of the effective medium models from Hertz-Mindlin theory is hindered by differing nomenclature and notation among the various references. Since the main focus of this paper is to define a unified effective medium model for sediments saturated with gas hydrates, a short history is warranted to provide common nomenclature, notation, and context.

Sava and Hardage (2006a, b) describe a Hertz-Mindlin model based on Dvorkin and Nur (1996) and Walton's (1987) smooth model. Walton's perfectly smooth sphere model is offered to better explain the low shear strengths and high Vp/Vs ratios observed in deepwater multicomponent seismic data. They consider Walton's smooth model theory "particularly appropriate for highly unconsolidated sediments at low effective pressure where grain rotation and slip along grain boundaries are likely to occur."

Jenkins et al. (2005) has shown that the Walton (1987) model, consisting of equations for infinitely rough and perfectly smooth spheres, can be consolidated into a single mathematical model using a partitioning parameter to specify the percentage of particles that are rough spheres with the remaining spheres being smooth. In order to compare the versions of effective medium models at issue, we use a previously developed framework for gas hydrates in unconsolidated sediments (Helgerud et al., 1999; Helgerud, 2001).

1.2 EFFECTIVE MEDIUM MODELS

We reproduce the equations of the two most widely used effective medium models for unconsolidated sediments (Walton, 1987; Dvorkin and Nur, 1996). Then, we develop the mathematical equations for the pore-fluid and rock matrix models (see Figure

1) but restrict ourselves only to making predictions for the rock-matrix grain model since it is the only grain model that well matches the Mallik data as shown in Dai et al. (2004, 2008a) and Xu et al. (2004). Bulk and shear moduli and densities used in calculations are given in Table 1.

1.2.1 Physical Basis of Hertz-Mindlin Effective Medium Models

Hertz theory (Mindlin, 1949, p. 259, eqn. 1) provides that two elastic bodies pressed together with a force will form a contact surface elliptic in shape (see Walton, 1987, Figure 1); the normal pressure on the contact surface of the ellipse is modeled by the equation

$$p = \frac{3P_z}{2\pi ab}\left(1 - \frac{x^2}{a^2} - \frac{y^2}{b^2}\right)^{1/2}. \tag{1}$$

Hertz-Mindlin theory (Mindlin, 1949) considers the addition of a monotonically increasing tangential force across the contact surface. Mindlin (1949, Figure 1) proceeds to find the resulting tangential and torsional compliances. More specifically, the equation for the tangential compliance without slip (Mindlin, 1949, p. 263, eqn. 77) is

$$C_x' = \frac{\delta_x'}{2P_x} = \frac{3\lambda + 4\mu}{16\mu(\lambda + \mu)a} = \frac{2 - \nu}{8\mu a}. \tag{2}$$

The tangential compliance with slip (Mindlin, 1949, p. 264, eqn. 103) is

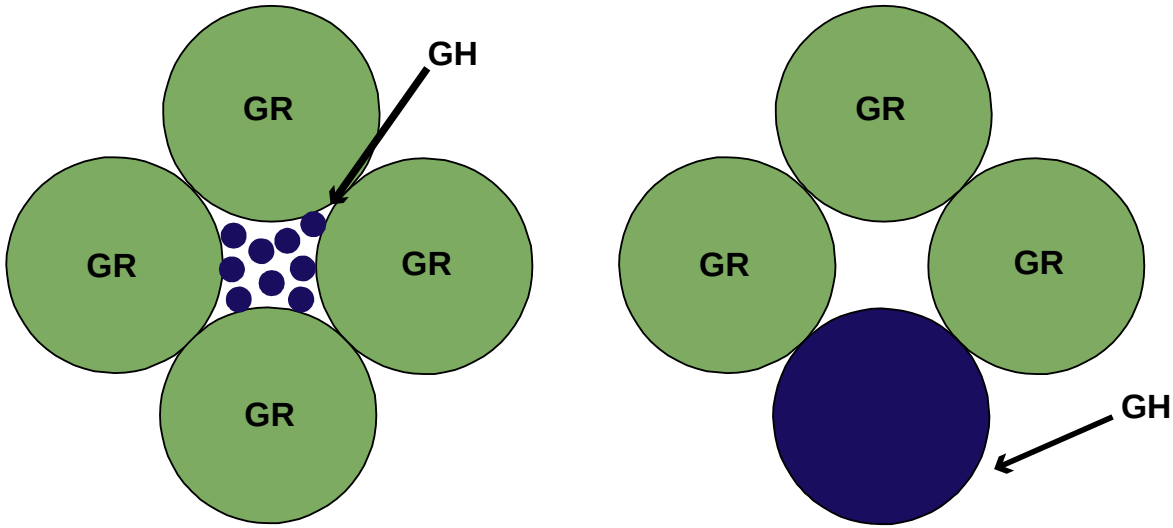

(a) Pore-Fluid Model (b) Rock Matrix Model

Figure 1. Model configurations for gas hydrates in unconsolidated sediments: (a) pore-fluid model in which the gas hydrate is homogeneously distributed throughout the pore space, (b) rock matrix model in which the gas hydrate is part of the rock matrix and contributes to the stiffness of the rock matrix.

In the Hertz-Mindlin model (Mindlin, 1949), first the spheres are pressed together, then a tangential force is applied under an assumption of no slip at the contact surface.

1.2.2 Walton Models

Two closely related models are presented in Walton (1987) in which the normal and shear deformations are applied simultaneously. For infinitely rough spheres under hydrostatic strain (Walton, 1987, eqn. 4.10), the effective moduli are

$$\lambda^* = \frac{\phi k C(-e)^{1/2}}{10\pi^2 B(2B+C)} = \frac{C}{10(2B+C)}\left(\frac{3\phi^2 k^2 p}{\pi^4 B^2}\right)^{1/3}, \tag{4}$$

$$\mu^* = \frac{\phi k(5B+C)(-e)^{1/2}}{10\pi^2 B(2B+C)} = \frac{(5B+C)}{10(2B+C)}\left(\frac{3\phi^2 k^2 p}{\pi^4 B^2}\right)^{1/3}, \tag{5}$$

where

$$B = \frac{1}{4\pi}\left\{\frac{1}{\mu} + \frac{1}{\lambda+\mu}\right\}, \tag{6}$$

$$C = \frac{1}{4\pi}\left\{\frac{1}{\mu} - \frac{1}{\lambda+\mu}\right\}. \tag{7}$$

For perfectively smooth spheres under hydrostatic strain (Walton, 1987, eqn. 4.16), the effective moduli are

$$\lambda^* = \mu^* = \frac{\phi k(-e)^{1/2}}{10\pi^2 B} = \frac{1}{10}\left(\frac{3\phi^2 k^2 p}{\pi^4 B^2}\right)^{1/3}, \tag{8}$$

Alternatively, the effective bulk modulus, $k^* = \lambda^* + \frac{2}{3}\mu^*$ is given in the form (Walton, 1987, eqn. 4.18)

$$k^* = \frac{1}{6}\left(\frac{3\phi^2 k^2 p}{\pi^4 B^2}\right)^{1/3}. \quad (9)$$

In solutions of physical interest the contact area is small relative to the size of the body, and except in some neighborhood of the contact area, surface displacements are negligible. Though the model was developed for the case of purely normal compression; "results are expected to apply for the more general oblique compression" (Walton, 1987, p. 218).

1.2.3 Dvorkin - Nur Model

Dvorkin and Nur (1996, eqn. 4) and Dvorkin et al. (1999, eqn. 1) developed their contact model for unconsolidated sands on the Hertz-Mindlin model (Cordon et al., 2006). For infinitely rough spheres, the effective moduli are written in the form

$$K_{HM} = \left[\frac{k^2(1-\phi_c)^2 G^2}{18\pi^2(1-\nu)^2} P\right]^{1/3}, \quad (10)$$

$$G_{HM} = \frac{5-4\nu}{5(2-\nu)}\left[\frac{3k^2(1-\phi_c)^2 G^2}{2\pi^2(1-\nu)^2} P\right]^{1/3}. \quad (11)$$

This Hertz-Mindlin model, calculated at the critical porosity, is extended to other porosities using modified Hashin-Shtrikman bounds (Hashin and Shtrikman, 1963; Dvorkin and Nur, 1996). See Equations 17 thru 20 below for the resulting dry-rock effective moduli. This model also accounts for the pressure dependence normally observed in unconsolidated sands.

1.2.4 Jenkins Update (Extended Walton Model)

Jenkins et al. (2005, eqns. 1 and 2) provide an update to the Walton (1987) model by consolidating the mathematical presentation of the infinitely rough and perfectly smooth sphere models into a single expression, as

$$\lambda^E = \frac{kv}{5\pi}\frac{\mu}{(1-\nu)}\left[\frac{3\pi}{2}\frac{(1-\nu)}{vk}\frac{p}{\mu}\right]^{1/3}\frac{[2-\nu-2\alpha(1-\nu)]}{(2-\nu)}, \tag{12}$$

$$\mu^E = \frac{kv}{5\pi}\frac{\mu}{(1-\nu)}\left[\frac{3\pi}{2}\frac{(1-\nu)}{vk}\frac{p}{\mu}\right]^{1/3}\frac{[2-\nu+3\alpha(1-\nu)]}{(2-\nu)}. \tag{13}$$

In this so-called extended Walton model, Jenkins et al. (2005) introduced the friction coefficient α. In this update, $\alpha = 0.0$ and $\alpha = 1.0$, respectively, are the end states of a perfectly smooth sphere (frictionless interaction) and an infinitely rough sphere (or no-slip). For completeness, we note the effective bulk modulus is written

$$K^E = \lambda^E + \frac{2}{3}\mu^E. \tag{14}$$

1.2.5 Extended Effective Medium Model

Though the Dvorkin and Nur (1996) model is likely more frequently referenced than Walton (1987), it has occasionally been noted that the Dvorkin and Nur (1996) model overpredicts the compressional wave velocity and significantly overpredicts the shear wave velocity (Dai et el, 2004; Sava and Hardage, 2006a, b). In the Hertzian model (Mindlin, 1949), used by Dvorkin and Nur (1996), the compressive and tangential forces are assumed to be applied sequentially; in Walton's model, the force calculations are set up or applied simultaneously. It was not appreciated at the time of development that the Dvorkin-Nur model could be algebraically converted to the infinitely rough sphere model

of Walton. The different assumptions have a minimal impact with respect to the infinitely rough spheres, but not for the smooth sphere model of Walton.

We adopt the approach of the extended Walton model (Jenkins et al., 2005) to use as our effective medium model, but use the nomenclature from Dvorkin and Nur (1996). Similar to Dvorkin and Nur (1996), an expression for bulk modulus is used in place of the Lamé coefficient. Therefore, the "extended" Hertz-Mindlin effective medium model is written

$$K_{HM} = \left[\frac{k^2(1-\phi_c)^2 G^2}{18\pi^2(1-\nu)^2} P\right]^{1/3}, \tag{15}$$

$$G_{HM} = \frac{1}{5}\left[\frac{3k^2(1-\phi_c)^2 G^2}{2\pi^2(1-\nu)^2} P\right]^{1/3} \frac{[2-\nu+3\alpha(1-\nu)]}{(2-\nu)}. \tag{16}$$

The parameter k, the average number of contacts per particle (or coordination number), is actual plus near (Bernal and Mason, 1960; Scott, 1960). For sediment made up of more than one grain material, Hill's average (Hill, 1952) is used to calculate the moduli.

The coordination number continues to be an issue of uncertainty. Based on arguments in Murphy (1982, p. 52) and the model in Mavko et al. (1998, p. 150, Figure 5.2.2), the coordination number is shown to average 8.5 over the small range of porosities from 0.36 to 0.40. Recent studies (Dutta, 2009; Zhang et al., 2013) argue that results comparable to statistical model results from Jenkins et al. (2005) can be obtained with the extended Walton model by incorporating the coodination number as a function of porosity or pressure. For this work we set the coordination number to 8.5 (actual plus near), and address this issue in more detail in Appendix A.

1.3 GAS HYDRATES IN UNCONSOLIDATED SEDIMENTS

We consider the baseline model for unconsolidated sediments without hydrate. Then we apply modifications for hydrate formation within the unconsolidated sediments.

1.3.1 Baseline Model for Unconsolidated Sediments

To implement the extended effective medium model we adopt the framework for unconsolidated sediments (Dvorkin and Nur, 1996; Helgerud, 2001). Then we apply the modified Hashin-Shtrikman bounds to the Hertz-Mindlin model. For unconsolidated sediments we chose to use a critical porosity of 0.40, corresponding to the porosity of a random loose packing of spheres. Here we outline those bounds as defined in Helgerud (2001).

Hashin-Shtrikman Bounds

Dvorkin and Nur (1996) show that unconsolidated sands are best described using Hertz-Mindlin contact theory (Mindlin, 1949) in combination with the modified Hashin-Shtrikman lower bound. Unconsolidated sands are mechanically held together by the confining pressure. For uncemented materials the practice has been to define the critical porosity (somewhere between 0.36 to 0.40 for unconsolidated sands) based on random packing to predict the effective dry frame moduli. Then modified Hashin-Shtrikman bounds can be applied to predict the effective-dry frame moduli at porosities away from the critical porosity. In the presence of uncertainty of the geometry and phase behavior Hashin-Shtrikman bounds have been shown to be the most restrictive possible (Hashin and Shtrikman, 1963). Separating into regions above and below the critical porosity, the equations for the effective dry-rock moduli are as follows:

Porosity $\phi < \phi_c$

$$K_{Dry} = \left[\frac{\phi/\phi_c}{K_{HM} + \frac{4}{3}G_{HM}} + \frac{1-\phi/\phi_c}{K + \frac{4}{3}G_{HM}}\right]^{-1} - \frac{4}{3}G_{HM}, \quad (17)$$

$$G_{Dry} = \left[\frac{\phi/\phi_c}{G_{HM} + \frac{G_{HM}}{6}\left(\frac{9K_{HM}+8G_{HM}}{K_{HM}+2G_{HM}}\right)} + \frac{1-\phi/\phi_c}{G + \frac{G_{HM}}{6}\left(\frac{9K_{HM}+8G_{HM}}{K_{HM}+2G_{HM}}\right)}\right]^{-1} . \quad (18)$$
$$- \frac{G_{HM}}{6}\left(\frac{9K_{HM}+8G_{HM}}{K_{HM}+2G_{HM}}\right)$$

Porosity $\phi > \phi_c$

$$K_{Dry} = \left[\frac{(1-\phi)/(1-\phi_c)}{K_{HM} + \frac{4}{3}G_{HM}} + \frac{(\phi-\phi_c)/(1-\phi_c)}{K + \frac{4}{3}G_{HM}}\right]^{-1} - \frac{4}{3}G_{HM}, \quad (19)$$

$$G_{Dry} = \left[\frac{(1-\phi)/(1-\phi_c)}{G_{HM} + \frac{G_{HM}}{6}\left(\frac{9K_{HM}+8G_{HM}}{K_{HM}+2G_{HM}}\right)} + \frac{(\phi-\phi_c)/(1-\phi_c)}{\frac{G_{HM}}{6}\left(\frac{9K_{HM}+8G_{HM}}{K_{HM}+2G_{HM}}\right)}\right]^{-1} . \quad (20)$$
$$- \frac{G_{HM}}{6}\left(\frac{9K_{HM}+8G_{HM}}{K_{HM}+2G_{HM}}\right)$$

We also include the following definitions:

Gassmann's Equations

Though most commonly used in fluid substitution studies, Gassmann's equations (Gassmann, 1952, original German language source; Mavko et al., 1998, p. 168; Han and Batzle, 2004, p. 398) are used here to calculate the saturated effective medium moduli from the dry frame moduli. Most of the effect of a passing wave is realized in the bulk modulus because the pressure wave causes a volume deformation that stiffens the frame;

shear deformation does not produce a similar effect. This is seen in Gassmann's equations given here in their typical form:

$$K_{Sat} = K\frac{\phi K_{Dry} - (1+\phi)\frac{K_f K_{Dry}}{K} + K_f}{(1-\phi)K_f + \phi K - \frac{K_f K_{Dry}}{K}}, \tag{21}$$

$$G_{Sat} = G_{Dry}. \tag{22}$$

Velocity equations

$$V_p = \sqrt{\frac{K_{Sat} + \frac{4}{3}G_{Sat}}{\rho_B}}, \tag{23}$$

$$V_s = \sqrt{\frac{G_{Sat}}{\rho_B}}. \tag{24}$$

Bulk density

$$\rho_B = \phi\rho_w + (1-\phi)\rho_{solid}. \tag{25}$$

With this baseline model for unconsolidated sediments we can compare calculated compressional and shear wave velocities for the infinitely rough and perfectly smooth sphere models with the extended Walton model as rewritten above. Modifications to the model are needed to consider gas hydrates. For our model, configurations with gas hydrates in unconsolidated sediments, we adopt the pore-fluid and rock matrix models from Helgerud et al. (1999) and Helgerud (2001). The equations and description are given below.

1.3.2 Pore-Fluid Configuration

The pore-fluid model requires replacing the fluid bulk modulus with

$$K_f = \left[\frac{S_w}{K_w} + \frac{(1 - S_w)}{K_h}\right]^{-1}, \tag{26}$$

and updating the calculation of the bulk density as follows,

$$\rho_B = \phi\left[(1 - S_h)\rho_f + S_h\rho_h\right] + (1 - \phi)\rho_{solid}. \tag{27}$$

1.3.3 Rock Matrix Configuration

Modifications to the baseline model are more extensive for the rock matrix model. First a reduced porosity is defined

$$\phi_r = \phi S_w = \phi(1 - S_h). \tag{28}$$

Then the grain moduli are recalculated using Hill's average (Hill, 1952) of the hydrate and mineral components using

$$K = \frac{1}{2}\left(f_h K_h + [1 - f_h]K_s + \left[\frac{f_h}{K_h} + \frac{(1 - f_h)}{K_s}\right]^{-1}\right), \tag{29}$$

$$G = \frac{1}{2}\left(f_h G_h + [1 - f_h]G_s + \left[\frac{f_h}{G_h} + \frac{(1 - f_h)}{G_s}\right]^{-1}\right), \tag{30}$$

where

$$f_h = \frac{\phi(1 - S_w)}{1 - \phi S_w}. \tag{31}$$

Then the calculation for bulk density is updated using

$$\rho_B = \phi_r\rho_f + (1 - \phi_r)\rho_{r-solid}. \tag{32}$$

1.4 APPLICATION OF MODEL TO MALLIK WELL

Previous studies and validation of effective medium models have been conducted using well log data from the Mallik gas hydrates project well 2L-38 (Cordon et al., 2006). The unified model with a rock matrix configuration for unconsolidated sands is applied to Mallik data to assess the model's capability to predict rock properties. We apply the model to the well log data from Mallik 5L-38 since this well provides an extensive set of logs available in digital form. For Mallik 5L-38 the analysis is carried out in two steps; first to determine the friction coefficient, then to model the velocity logs to refine the estimate of the friction coefficient.

1.4.1 Mallik 5L-38 Logs

For the more recent Mallik 5L-38 production well, we provide a detailed study with the unified model. The data for the Mallik 5L-38 well logs, documented in Dallimore and Collett (2005), was downloaded from an included CD (Compact Disc). The data sets used in validation of the model include the sonic, gas hydrate saturation, and thermal neutron porosity logs. In Figure 2 we display the data used with the unified model.

Sonic Logs

Data sets were available for a single compressional sonic sensor and each of two shear sonic sensor configurations, referred to as Lower and Upper. As a crossplot, the two shear sonic datasets are almost indistinguishable from each other, and therefore only results for the Upper sensor configuration are shown here. Figure 2 (a) shows the sonic logs for both the P-wave and the S-wave.

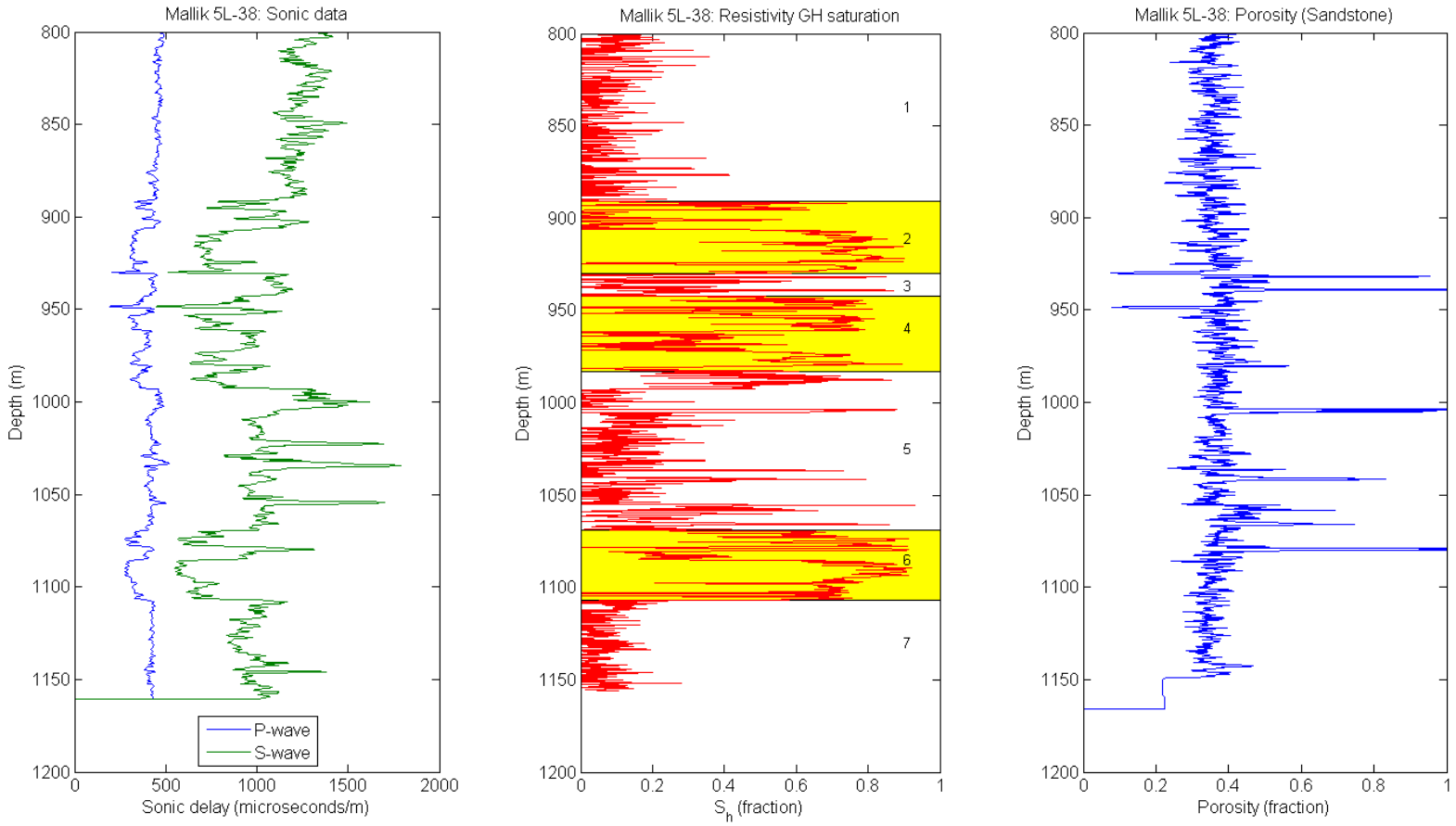

a) b) c)

Figure 2. Mallik 5L-38 well logs from Dallimore and Collett (2005): a) sonic logs; b) gas hydrate saturation log; and c) thermal neutron porosity log. In b) the yellow regions mark the gas hydrate windows.

Gas Hydrate Saturation Logs

Figure 2(b) shows the gas hydrate saturation logs documented in Collett et al. (2005). The gas hydrate saturation log was computed using an Archie – resistivity formula for the Lower and Upper dipole sensors, then averaged. For this analysis, note that we have numbered the windows from top to bottom as 1 thru 7. The overall gas hydrate zone, designated in Collett et al (2005), is identified as being from depth 891 m to 1,107 m. The three specific gas hydrate Windows (2, 4, and 6), highlighted in yellow on the gas hydrate saturation data of Figure 2 (b), are from 891 thru 931 m; 942 thru 983 m; and 1,069 thru 1,107 m (Collett et al., 2005, Figure 1, oversize). Here Windows 1, 3, 5, and 7 are the Non-hydrate Windows.

Thermal Neutron Porosity Log (Sandstone)

In the remaining subplot, Figure 2 (c), the thermal neutron porosity log is presented as interpreted for sandstone (Collett et al, 2005). The neutron porosity log shows a consistent band of porosity between 20 and 45 percent (pore fractions 0.2 and 0.45).

1.5 METHODOLOGY AND APPROACH

To validate the unified model the gas hydrate saturation and the neutron porosity logs are used as input to generate synthetic values of compressional and shear wave velocities that are to be compared with the velocities obtained from the measured sonic logs. Two approaches are used to visualize the results of the calculations. First, velocity crossplots of compressional versus shear wave velocities are constructed with the measured velocities plotted on top of the modeled velocities. In a second step, the compressional and shear wave velocities are plotted separate from each other as logs with

depth; again, the measured velocities are plotted on top of the modeled velocities adjusting the friction coefficient until an appropriate match is determined.

1.5.1 Expanded View of Porosity

More in-depth views of the porosity log are provided in Figure 3. In Figure 3 a) a running average window of 101 points is superimposed over the porosity log along with the standard deviation from the calculation. The running average window length was chosen after carefully reviewing both larger and smaller values. Larger averaging windows caused the porosity data to be much too blocky; with smaller averaging windows causing the curve to quickly become noisy. The intent has been to use a smoothened version of the porosity as input to the model; however, experiments have shown that the best matches of synthetic velocities to the logs calculated from the measured sonic logs are achieved using the unedited porosity data. Reducing the noise spikes by averaging introduces significant discrepancies when trying to match modeled and measured velocity logs. Immediately below, this is addressed in more detail; first notice the porosity plots are expanded for the Hydrate Windows in the other subplots of Figure 3; i.e. Figures 3 b), c), and d), respectively, provide close up views of the porosity logs for the gas hydrate regions 2, 4, and 6.

Specific examples of the problems encountered using the average porosity curve, applicable to compressional and shear model velocities, include the following:

1) Hydrate Window 2: Spike in velocity at 930 m depth not captured; artificially truncates low velocity sections 896-890 m and 902-906 m depth at higher values.
2) Hydrate Window 4: Spike in velocity at 948 m depth not properly captured.

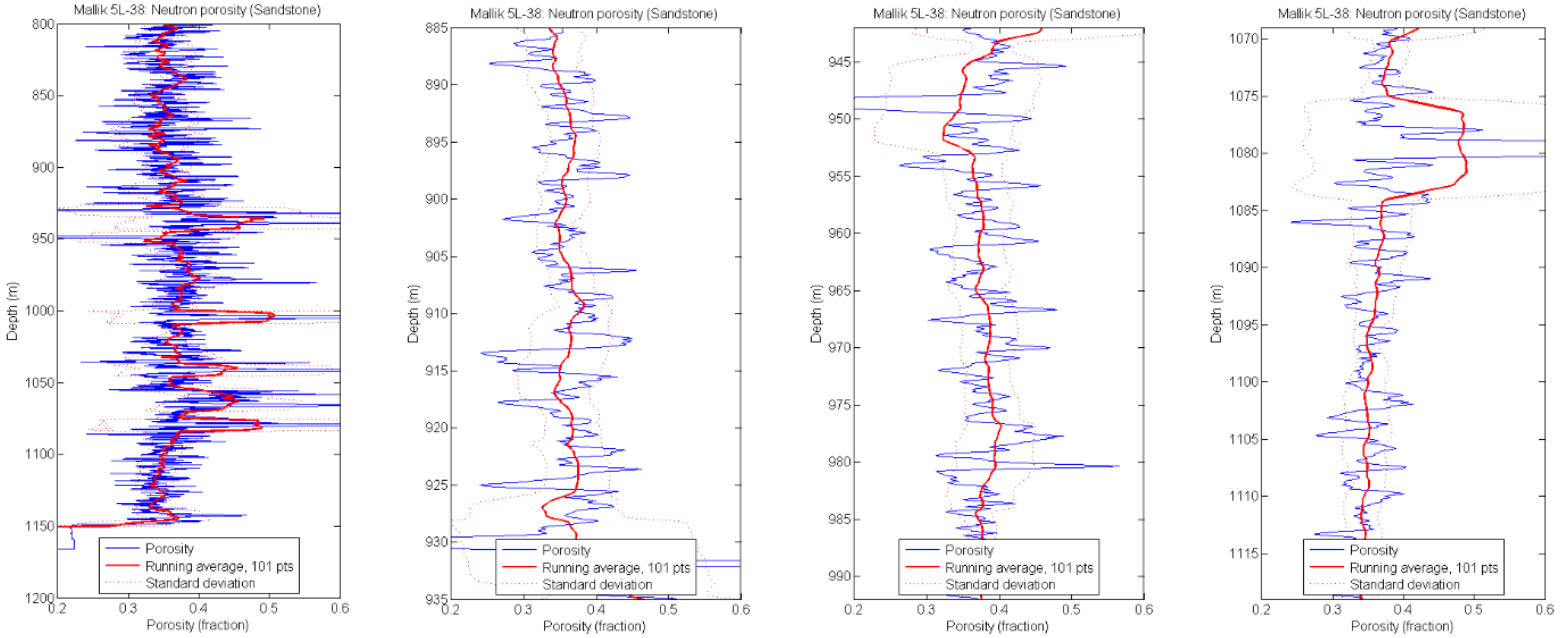

Figure 3. Mallik 5L-38 neutron porosity well log from Dallimore and Collett (2005): a) porosity log (blue) with 101 point averaging window and standard deviations (red) overlaid; b) Hydrate Window 2 expanded; c) Hydrate Window 4 expanded; and d) Hydrate Window 6 expanded.

3) Hydrate Window 6: Discontinuity or rapid change in velocity at 1079 m depth is not properly captured.

1.5.2 Velocity Crossplots

A series of velocity crossplots in Figures 4, 5, and 6 are used to demonstrate that crossplots of compressional versus shear wave velocities are a good way to verify that the unified model can successfully simulate these velocities, and can be compared against the velocities calculated from the measured sonic logs. The gas hydrate saturation and porosity logs are used as input to the unified model. For each of the 3 Hydrate Windows, 2, 4, and 6 (Figures 4, 5, and 6), model calculations are shown for 6 values of the friction parameter; the best match in these Hydrate Windows is for $\alpha = 0.2$. This could be because the grains are relatively smooth or that the grain material is soft.

In Figure 7 the unified model predictions are compared for the Non-hydrate Windows 1, 3, 5, and 7. Only model calculations for $\alpha = 0.2$ are shown. For 3 of the 4 windows, it is clear that the unified model does not match the measured pressure and shear wave velocities. Non-hydrate Window 5 of Figure 7 c), however, does show a linear trend comparable to the known hydrate windows; the linear trend here in Figure 7 c) is wider than would be expected, potentially the window may contain enough hydrate to change the trend.

1.5.3 Velocity Logs

The calculated compressional and shear wave velocities, from Figures 4, 5, and 6, are also displayed as velocity logs and are compared against the velocity logs created from the measured sonic logs. These results are shown in Figures 8, 9, and 10. Again we get good agreement, but obtain some surprising differences relative to the results from the

velocity crossplots previously discussed. In the previous results above, all three Hydrate Windows seemed to match with $\alpha = 0.2$. Here, in general $\alpha = 0.2$ is good for Hydrate Windows 2 and 6, but $\alpha = 0.4$ for the pressure wave. The match in each of the Hydrate Windows varies depending on the section of the Hydrate Window, suggesting that the character of the hydrate may in fact change with depth in the well.

Log comparisons are shown in Figure 11 for the unified model predictions against the measured velocity logs for the Non-hydrate Windows. Again, for these Non-hydrate Windows, only $\alpha = 0.2$ results are shown. There seems to be little correlation between the measured and modeled data sets.

1.6 DISCUSSION

The critical porosity of unconsolidated sands varies in the range from 0.36 to 0.40 (Dvorkin and Nur, 1996), so, assuming unconsolidated sediments, we set $\phi_c = 0.40$ and use a coordination number of $k = 8.5$. When using the gas hydrate saturation and porosity logs to drive the model, we base the pressure on the log depth; otherwise the model curves are predicted assuming a depth of 1000 m. To extend our calculations to other porosities our model includes modified lower and upper Hashin-Shtrikman bounds (Dvorkin and Nur, 1996). Gas hydrate parameters are as follows (Dai et al., 2004): For the bulk modulus we have $K = 5.6$ GPa; the shear modulus is $\mu = 2.4$ GPa; the density is $\rho = 0.90$ g/cc. In the unified model the clay/Quartz ratio is $40/60$, slightly higher than the $37/63$ used in Xu et al. (2004).

Xu et al. (2004) and others have noted the tendency of effective medium models to overestimate S-wave velocities at high gas hydrate saturations. Sava and Hardage (2006b) have suggested the smooth sphere model of Walton (1987) as the solution to the

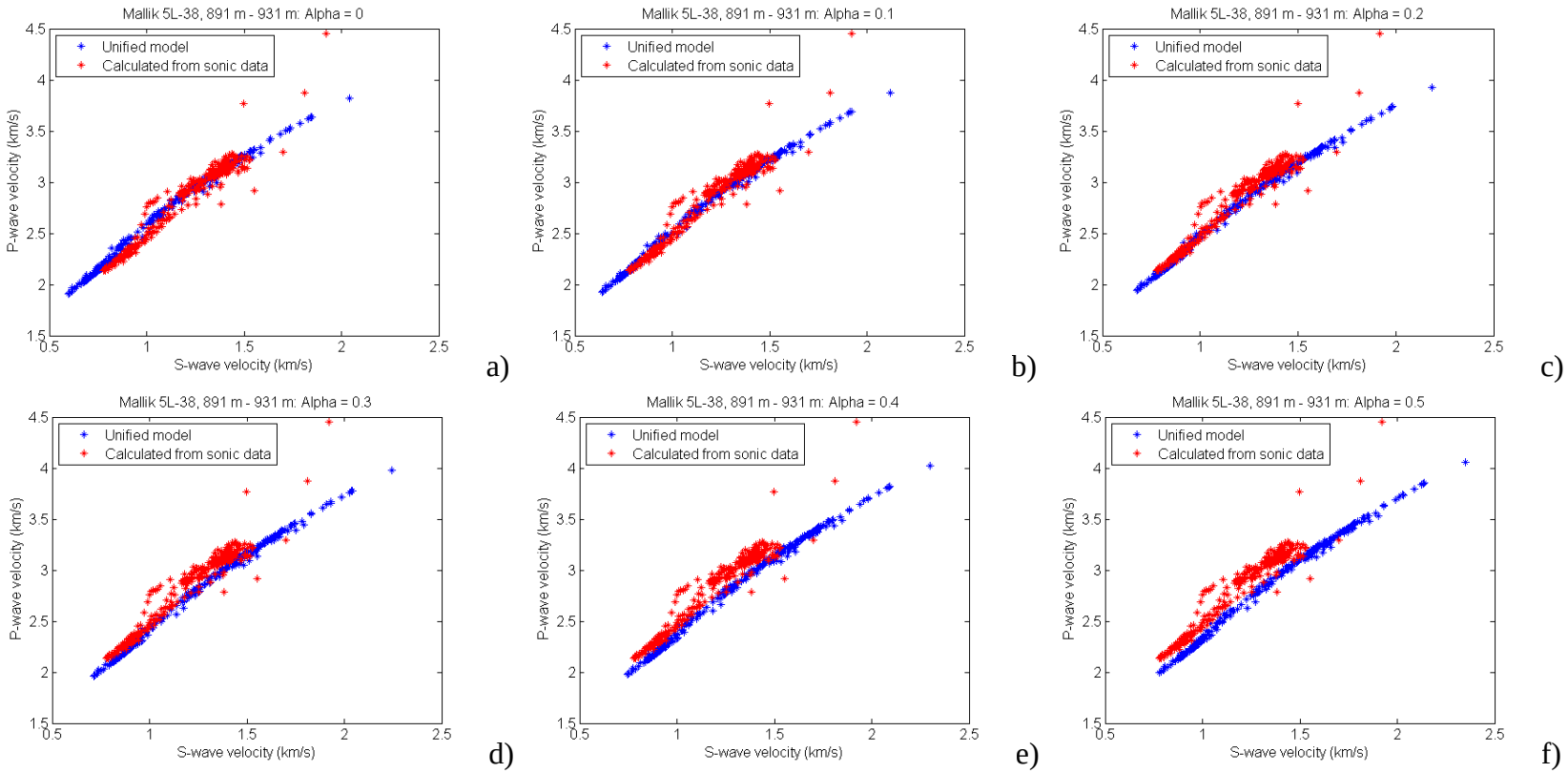

Hydrate Window 2

Figure 4. Crossplots of compressional versus shear wave velocities for Mallik 5L-38 well for gas hydrate Window 2, depths 891 m thru 931 m. Velocity values (red), calculated from the sonic logs, are overlaid onto predicted unified model velocity values (blue) for six values of the friction coefficient: a) $\alpha = 0.0$; b) $\alpha = 0.1$; c) $\alpha = 0.2$; d) $\alpha = 0.3$; e) $\alpha = 0.4$; and f) $\alpha = 0.5$. Measured sonic log values are from Dallimore and Collett (2005).

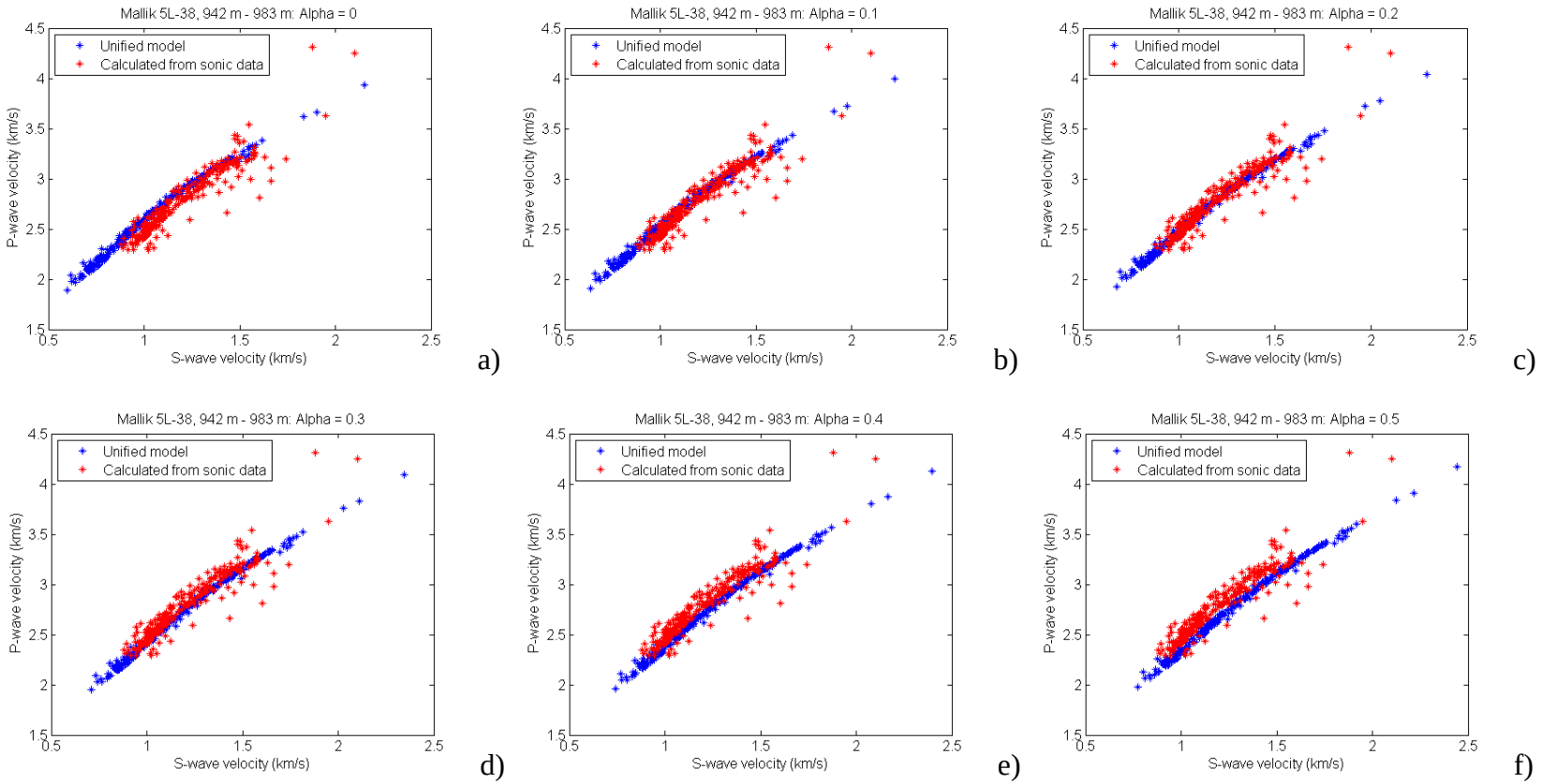

Hydrate Window 4

Figure 5. Crossplots of compressional versus shear wave velocities for Mallik 5L-38 well for gas hydrate Window 4, depths 942 m thru 983 m. Velocity values (red), calculated from the sonic logs, are overlaid onto predicted unified model velocity values (blue) for six values of the friction coefficient: a) $\alpha = 0.0$; b) $\alpha = 0.1$; c) $\alpha = 0.2$; d) $\alpha = 0.3$; e) $\alpha = 0.4$; and f) $\alpha = 0.5$. Measured sonic log values are from Dallimore and Collett (2005).

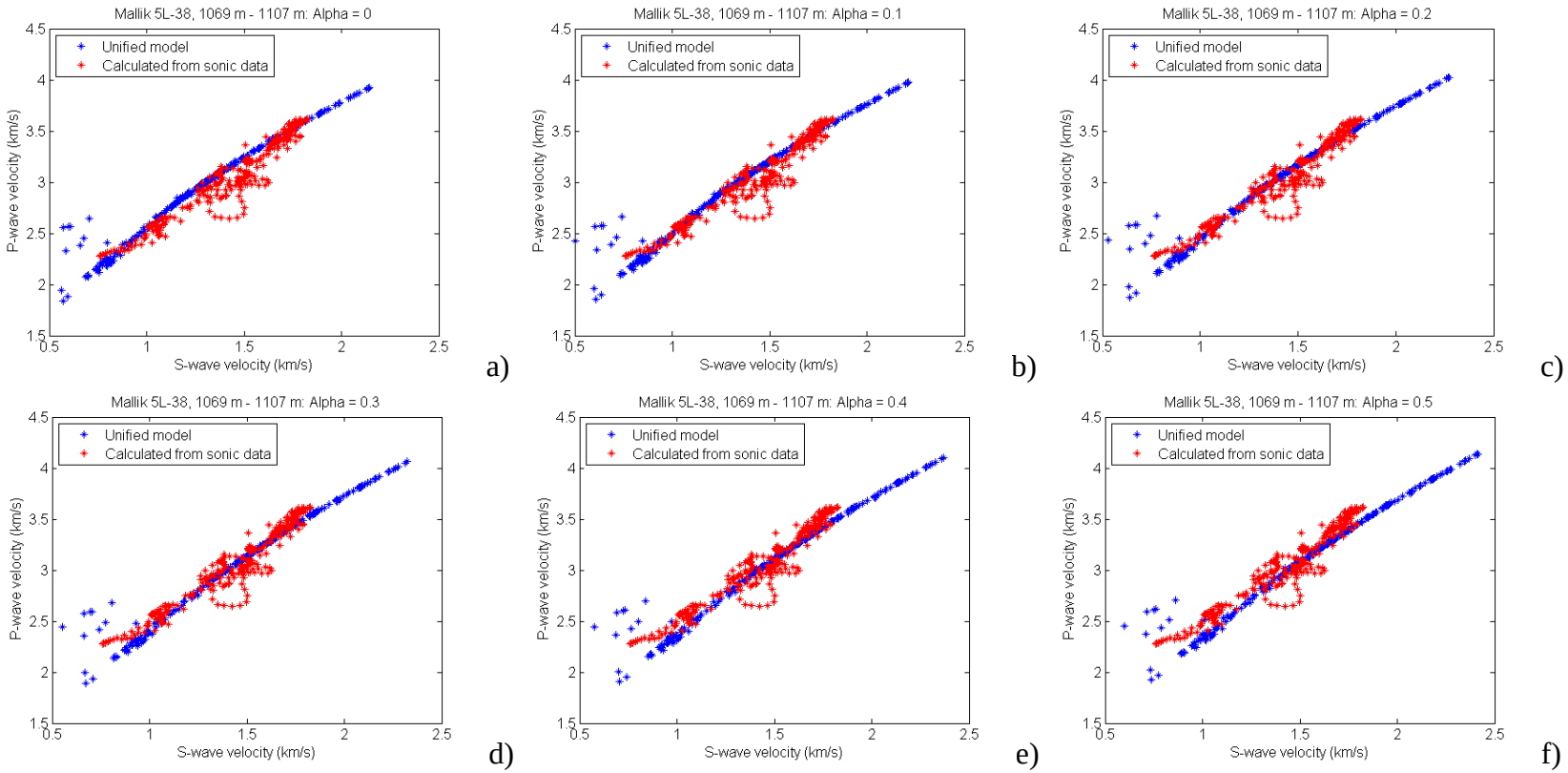

Hydrate Window 6

Figure 6. Crossplots of compressional versus shear wave velocities for Mallik 5L-38 well for gas hydrate Window 6, depths 969 m thru 1,107 m. Velocity values (red), calculated from the sonic logs, are overlaid onto predicted unified model velocity values (blue) for six values of the friction coefficient: a) $\alpha = 0.0$; b) $\alpha = 0.1$; c) $\alpha = 0.2$; d) $\alpha = 0.3$; e) $\alpha = 0.4$; and f) $\alpha = 0.5$. Measured sonic log values are from Dallimore and Collett (2005).

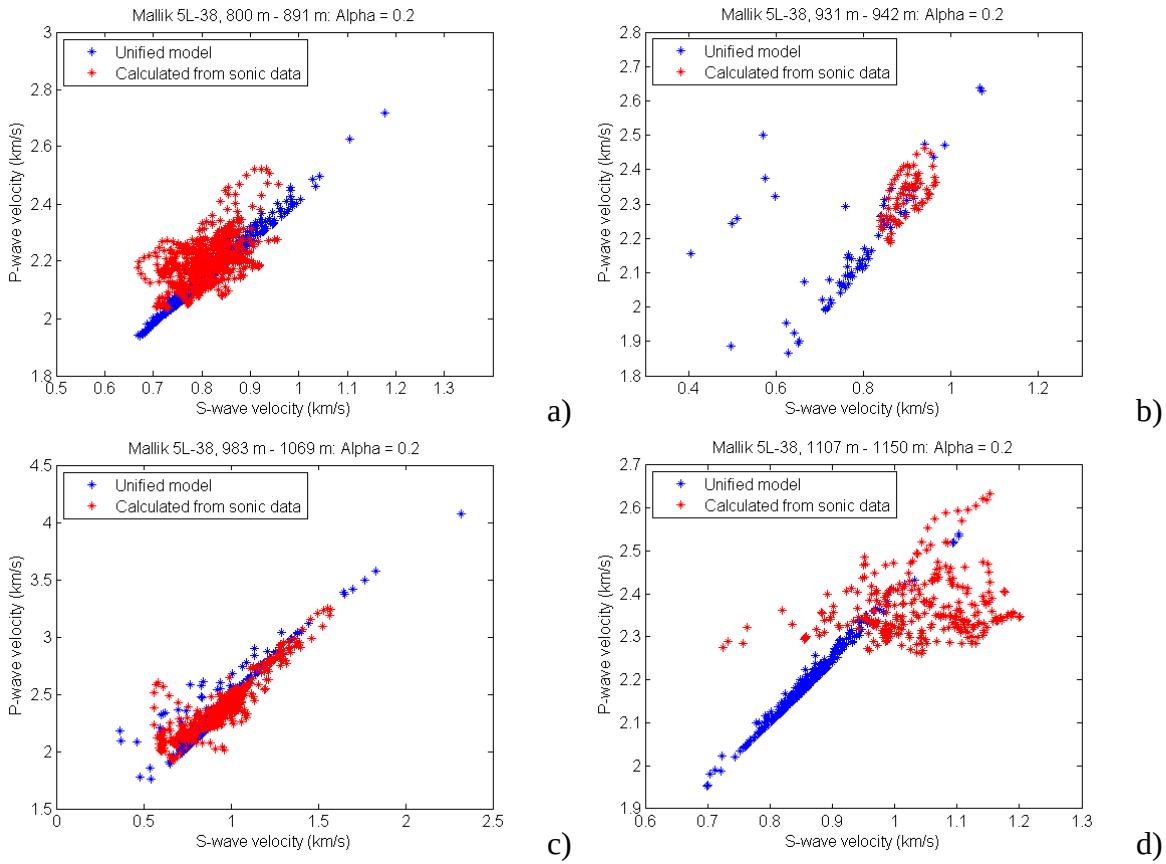

Non-Hydrate Windows 1, 3, 5, and 7

Figure 7. Crossplots of compressional versus shear wave velocities for Mallik 5L-38 well for Non-hydrate Windows. Velocity values (red), calculated from the sonic logs, are overlaid onto predicted unified model velocity values (blue) for a friction coefficient of $\alpha = 0.2$: a) Non-hydrate Window 1, 800-891 m; b) Non-hydrate Window 3, 931 -942 m; c) Non-hydrate Window 5, 983-1069 m; and d) Non-hydrate Window 7, 1107-1150 m. Measured sonic log values are from Dallimore and Collett (2005).

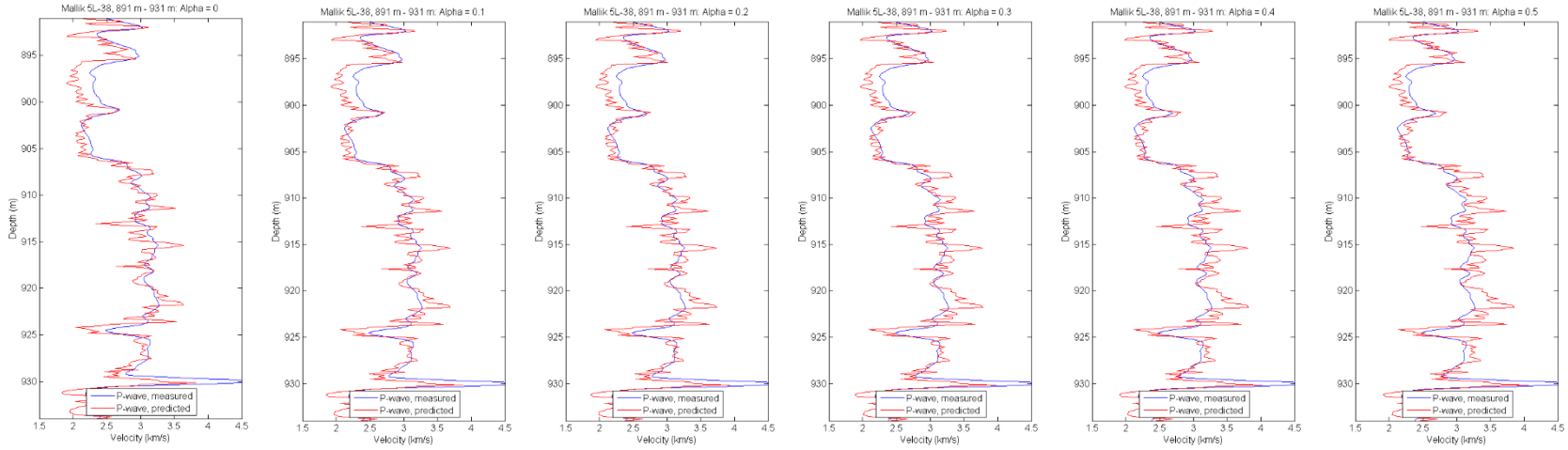

a)

Hydrate Window 2 for P-wave

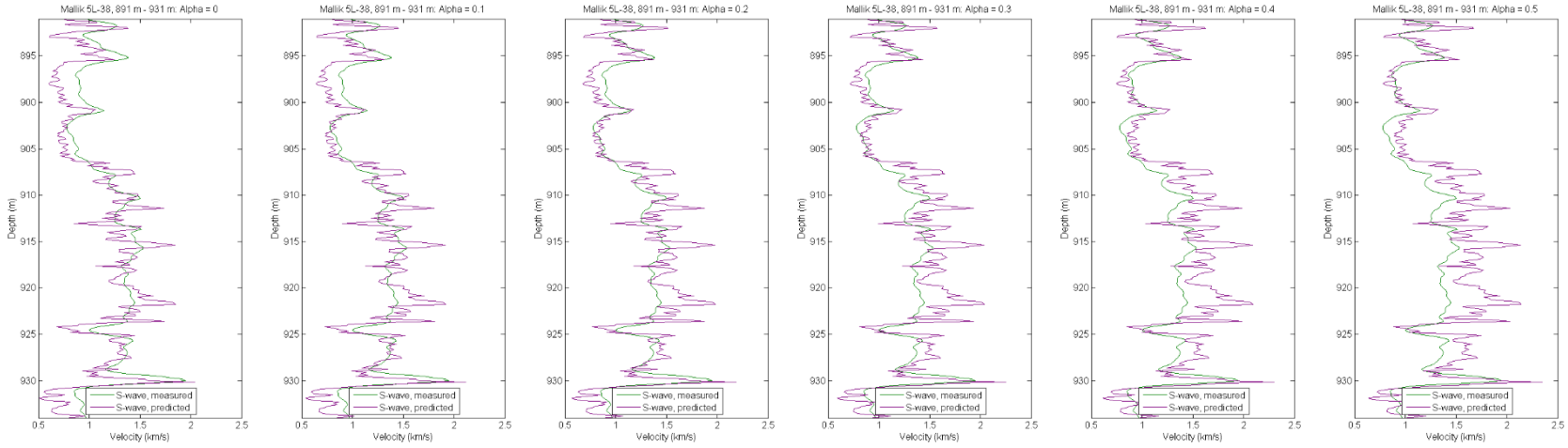

b)

Hydrate Window 2 for S-wave

Figure 8. Comparison of measured and predicted velocity logs for Hydrate Window 2 of Mallik 5L-38 for six values of the friction coefficient from $\alpha = 0.0$ to $\alpha = 0.5$: a) for compressional wave data, the simulated logs (red), generated by the unified model using the gas hydrate saturation (Archie-average resistivity) and porosity logs as inputs, are overlaid onto the velocities (blue) calculated directly from the measured sonic logs; b) for shear wave data, the simulated logs (purple), generated by the unified model using the gas hydrate saturation (Archie-average resistivity) and porosity logs as inputs, are overlaid onto the velocities (green) calculated directly from the measured sonic logs.

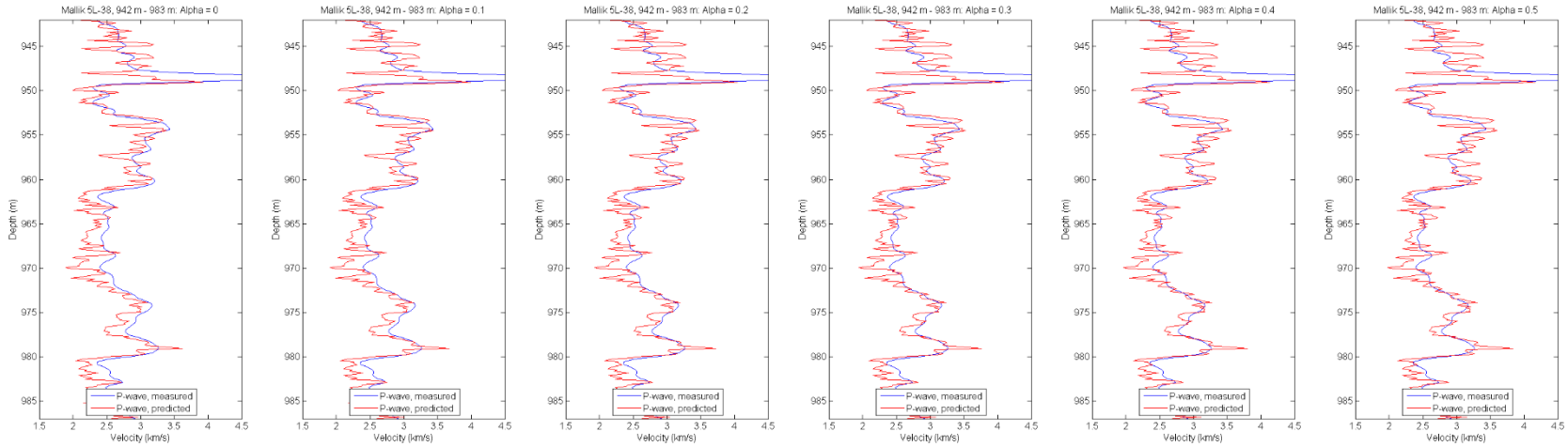

a)

Hydrate Window 4 for P-wave

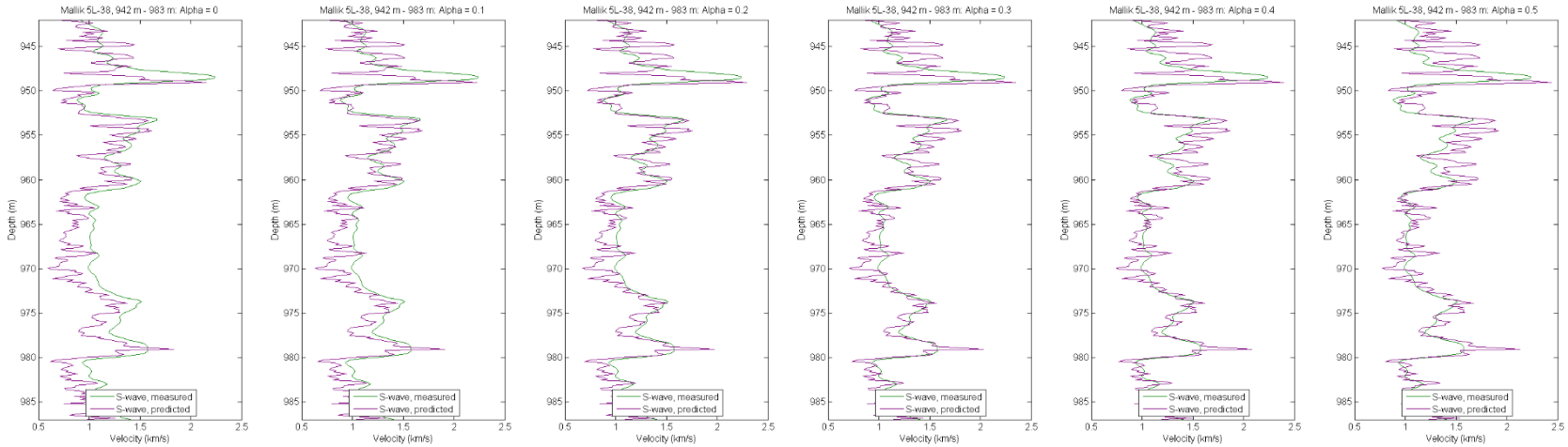

b)

Hydrate Window 4 for S-wave

Figure 9. Comparison of measured and predicted velocity logs for Hydrate Window 4 of Mallik 5L-38 for six values of the friction coefficient from $\alpha = 0.0$ to $\alpha = 0.5$: a) for compressional wave data, the simulated logs (red), generated by the unified model using the gas hydrate saturation (Archie-average resistivity) and porosity logs as inputs, are overlaid onto the velocities (blue) calculated directly from the measured sonic logs; b) for shear wave data, the simulated logs (purple), generated by the unified model using the gas hydrate saturation (Archie-average resistivity) and porosity logs as inputs, are overlaid onto the velocities (green) calculated directly from the measured sonic logs.

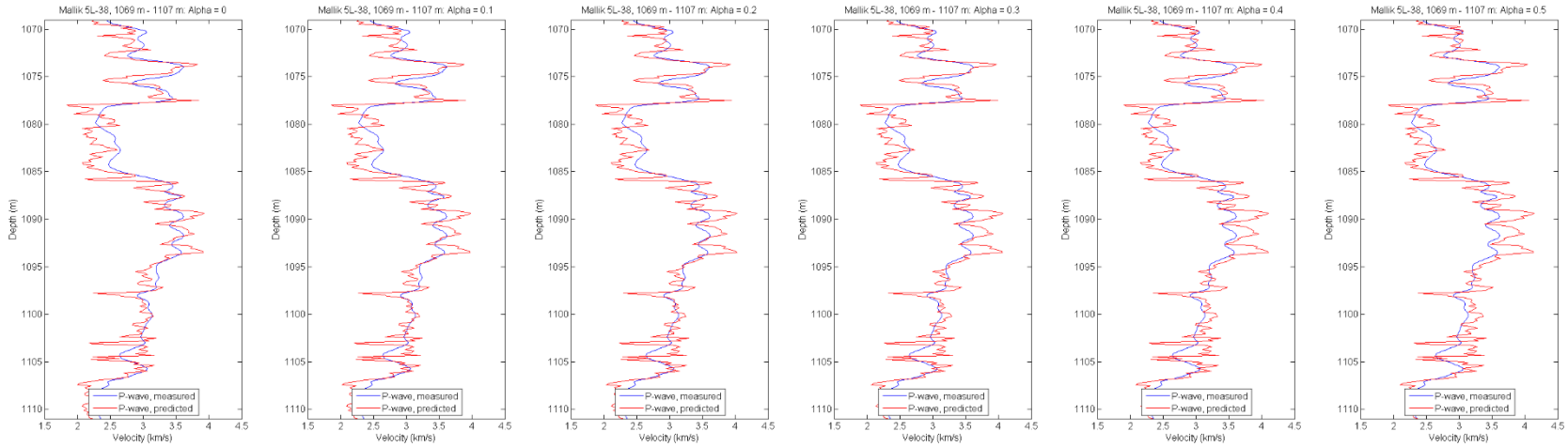

a)

Hydrate Window 6 for P-wave

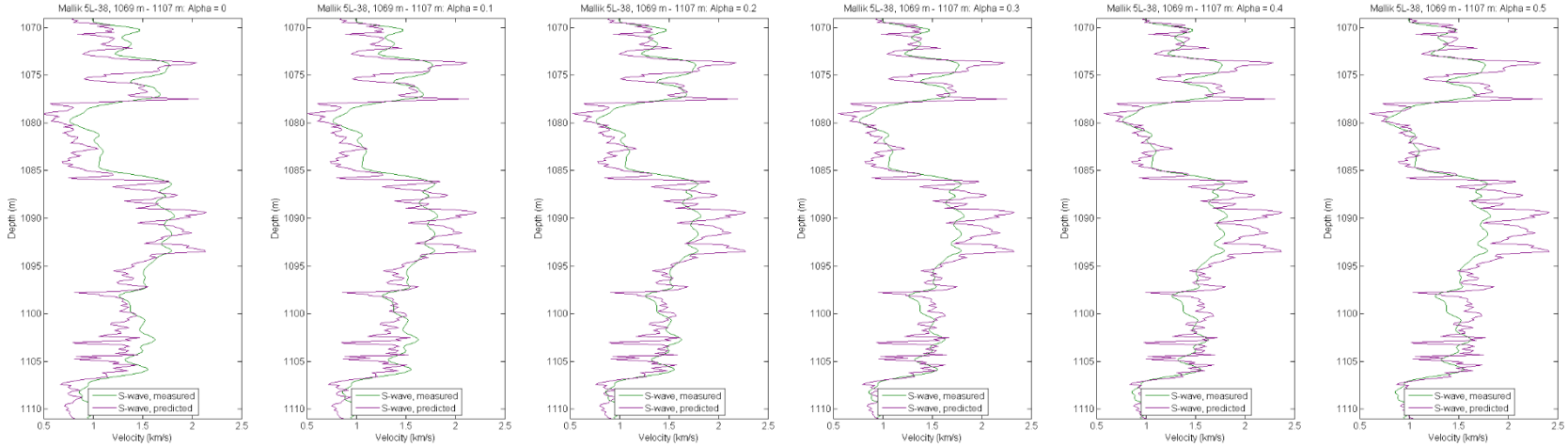

b)

Hydrate Window 6 for S-wave

Figure 10. Comparison of measured and predicted velocity logs for Hydrate Window 6 of Mallik 5L-38 for six values of the friction coefficient from $\alpha = 0.0$ to $\alpha = 0.5$: a) for compressional wave data, the simulated logs (red), generated by the unified model using the gas hydrate saturation (Archie-average resistivity) and porosity logs as inputs, are overlaid onto the velocities (blue) calculated directly from the measured sonic logs; b) for shear wave data, the simulated logs (purple), generated by the unified model using the gas hydrate saturation (Archie-average resistivity) and porosity logs as inputs, are overlaid onto the velocities (green) calculated directly from the measured sonic logs.

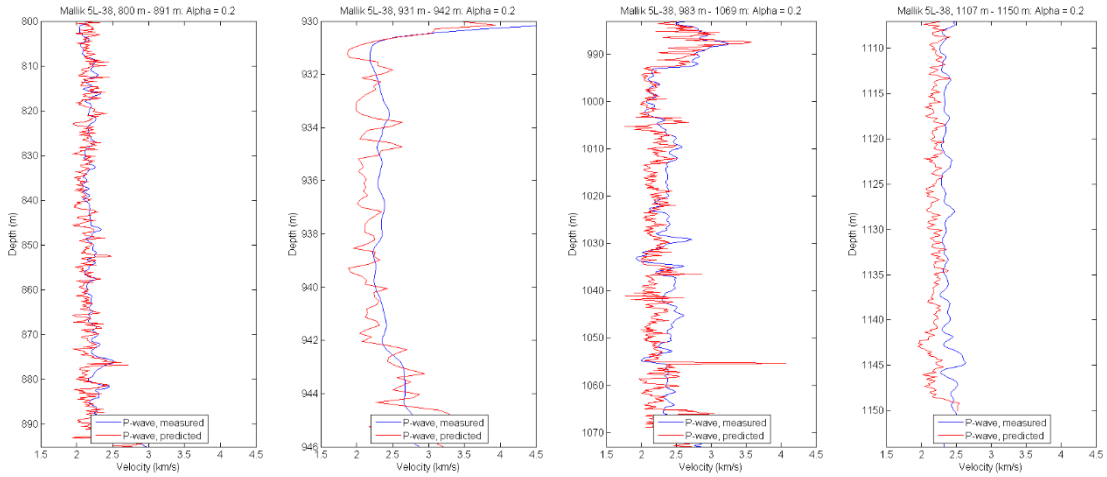

a)

Non-Hydrate Windows 1, 3, 5, and 7 for P-wave

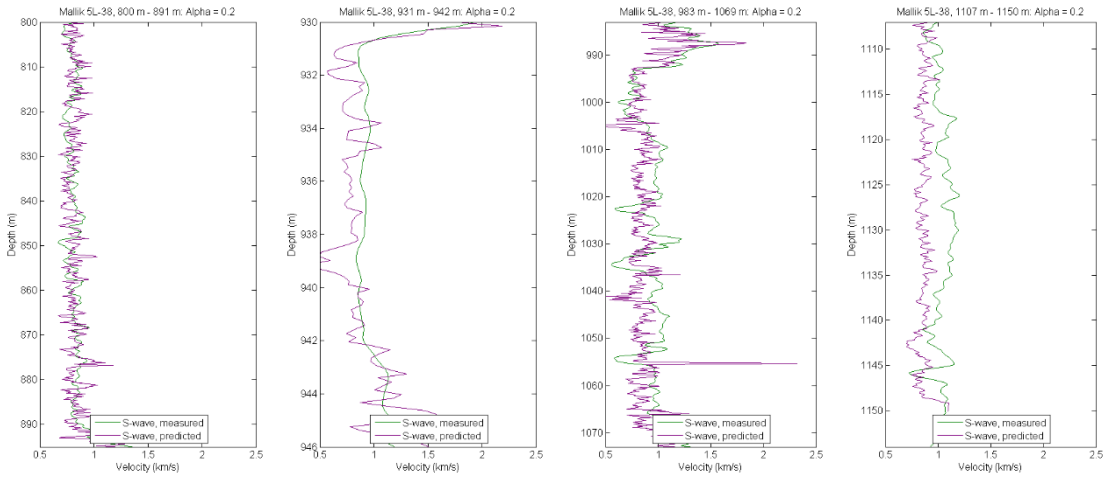

b)

Non-Hydrate Windows 1, 3, 5, and 7 for S-wave

Figure 11. Comparison of measured and predicted velocity logs for Non-hydrate Windows of Mallik 5L-38 for a single friction coefficient of $\alpha = 0.2$: a) for compressional wave data, the simulated logs (red), generated by the unified model using the gas hydrate saturation (Archie-average resistivity) and porosity logs as inputs, are overlaid onto the velocities (blue) calculated directly from the measured sonic logs; b) for shear wave data, the simulated logs (purple), generated by the unified model using the gas hydrate saturation (Archie-average resistivity) and porosity logs as inputs, are overlaid onto the velocities (green) calculated directly from the measured sonic logs.

overestimation. Cordon et al. (2006) supposedly used a rough sphere model and showed good agreement with the data of Mallik well 2L-38, but in reality the Cordon et al. (2006) model uses an empirical matching factor λ. With $\lambda = 2$, this corresponds more appropriately to $\alpha \approx 0.5$ for the unified model. Therefore, the Cordon model, though based on Dvorkin-Nur, should not be considered a rough sphere model since it uses an empirical matching factor to obtain its agreement with the data. Sriram et al. (2014, p. 329, eqn. B1) take an approach similar to Cordon et al. (2006) of using an infinitely rough sphere and adding a friction term, but take a more interesting approach using a Mindlin friction term that represents the fraction of the no-slip region to the grain radius. The Sriram model, adding a Mindlin friction term, is also a significant departure from the rough sphere model.

Results of the unified model are plotted in Figures 4, 5, and 6 for compressional versus shear wave velocities to ascertain that a very small friction coefficient ($\alpha = 0.2$ or thereabouts) is needed to accurately predict seismic velocities. This result for the unified model also confirms the earlier results from Bachrach and Avseth (2008). Using the friction coefficient α as an extra degree of freedom seems a viable approach.

The crossplots of compressional versus shear wave velocities in Figures 4, 5, and 6 for the three Hydrate Windows provide a consistent view that the selection of a friction coefficient of $\alpha = 0.2$ may be appropriate. In Figure 4 for Hydrate Window 2, specifically Figures 4 d), e), and f), the results of the model calculations (blue) and the measured values (red) for the crossplot do not match. Choosing among the remaining three subplots, a), b), and c) is more complicated because the measured (red) data shows two closely related linear trends. Initially Figure 4 b) might seem as a good choice with

offsetting misfits of the upper and lower sections of the measured data with the model data. But note that the upper portion of the measured data (red) is significantly broader than the lower section of the measured data (red). Based on this observation, Figure 4 c) is chosen as a better representation for matching Hydrate Window 2.

The selection in Hydrate Window 4 (Figure 5) is more clearly made than in the previous Hydrate Window 2 because the measured velocity data is more consistent. Figures 5 a), d), e), and f) are easily ruled out. The friction coefficient is selected as $\alpha = 0.2$.

The measured data in Hydrate Window 6 (Figure 6) is much less consistent than the previous two examples, yet still has a linear trend. The $\alpha = 0.2$, or Figure 6 c), choice is made since the linear trend of both ends of the measured values are coincident with the synthetic data (blue) from the model.

Measured data for all four of the Non-hydrate Windows, shown in Figure 7, are plotted at $\alpha = 0.2$. Of the four Non-hydrate Windows only Non-hydrate Window 5 shows a linear trend of the measured data coincident with the model data. It could be that this is a mixed hydrate/non-hydrate region since the width is significantly greater than in the known hydrate regions.

To further investigate these trends and anomalies, the model has also been exercised to generate synthetic compressional and shear wave velocity logs to match the velocity logs obtained from the measured sonic. The velocity logs are matched in Figures 8, 9, and 10 for the Hydrate Windows and in Figure 11 for the Non-hydrate Windows. As shown, the velocity logs provide a much more nuanced understanding of the influences on choosing the value for the friction coefficient. As with the velocity

crossplots, we ran the model to generate the velocity logs using six values of the friction coefficient from 0.0 to 0.5, and compare against the velocity data (based on the measured sonic logs). In Figures 8 thru 10 we show the comparisons for compressional and shear wave velocities for the three Hydrate Windows with the following conclusions:

Hydrate Window 2 (Figure 8):

Vp: Best overall match is for 0.2.

Vs: Best overall match is for 0.1 or 0.2.

Hydrate Window 4 (Figure 9):

Vp: Best overall match ranges from 0.3 to 0.5 (good at the top; poor at the bottom for0.3; reversed for 0.5).

Vs: Best overall match ranges from 0.2 to 0.4 (good at the top; poor at the bottom for0.2; reversed for0.4).

Hydrate Window 6 (Figure 10):

Vp: Best overall match is for 0.1 or 0.2.

Vs: Best overall match is for 0.2.

Figure 11 shows results for the Non-hydrate Windows, but only for a friction coefficient of 0.2.

1.6.1 Summary of Discussion

We incorporate the effective medium models from the work of Walton (1987), Dvorkin and Nur (1996), and Jenkins et al. (2005) into a single model that preserves the nomenclature of Dvorkin and Nur (1996). The unified model, based on capability of the Jenkins et al. (2005) extended Walton model to partition between rough and smooth grains, is reformulated to be consistent with Dvorkin and Nur (1996). We then

incorporate the extended effective medium model into the framework for unconsolidated sediments (Helgerud, 2001) using both the pore-fluid and the rock matrix configurations for grain placement with gas hydrates.

Furthermore, we apply the rock matrix model to data available from the Mallik gas hydrates project (Mckenzie River Delta, Northwest Territories, Canada), well 5L-38. We demonstrate how the model can be used in two steps. In the first step, we overlaid crossplots of compressional versus shear wave velocities for calculated and modeled acoustic logs, and compare the match until a good choice is found for the friction coefficient. For the second step we created a database of synthetic logs of compressional and shear wave velocities at appropriate friction coefficient values as seismic velocities versus gas hydrate saturation. The synthetic logs are overlain on the measured velocities calculated from the sonic logs.

Results here suggest the recommendation of Sava and Hardage (2006a, b) to use the smooth sphere grain model over the hard sphere model for unconsolidated sands was appropriate; with the unified model we are able to improve on that recommendation and refine results to a small friction coefficient between 0.2 and 0.4 for the Mallik wells.

The Cordon et al. (2006) model, based on Dvorkin-Nur, has previously been used to investigate the neighboring Mallik 2L-38 well (see Collett et al., 1999). Their model is presented as an infinitely rough sphere model, but actually uses an empirical adjustment factor that functions much like the friction coefficient of the unified model. Their "ad hoc reduction factor" (Cordon et al., 2006, p. F170, paragraph below eqn. A-3) at $\lambda = 2$ may be similar to the friction coefficient $\alpha = 0.5$ for the unified model; this helps explain how Cordon model results may not be that different to the results here.

Therefore, the Dvorkin-Nur model is an endpoint of the extended Walton model. Other models, such as Cordon et al. (2006) and Sriram et al. (2014), start from the Dvorkin-Nur model and make improvements to match the data. These improvements seem to march towards the smooth end of the effective medium models, yet it is thought Cordon et al. (2006) and Sriram et al. (2014) are using rough sphere models. For a future study it would be appropriate to directly compare the unified model and these alternative approaches with the data from both Mallik wells. Sriram et al. (2014) seems to be a more general approach, and may be a good alternative to the extended Walton model. There may be one model and multiple viable paths and models between the end points.

Though not a significant focus of this paper, we also have concluded that incorporating the coordination number as a function of porosity into an effective medium model is unresolved. There are discrepancies noted between Dutta (2009) and Zhang et al. (2013). To address the discrepancies, we built a model for the coordination number based on Mavko et al. (1998, page 150, Figure 5.2.2). The model largely had insignificant effects on our results, and therefore we cannot show whether Jenkins et al. (2005) conclusions from statistical modeling are verifiable. See Appendix A for more details.

We suggest possible paths to further improve the unified model and expand the envelope of its use: (1) use other suitable datasets to further validate the capability of the model presented here, and (2) expand the use of this model to lower effective-pressures to address issues regarding the coordination number and the discrepancies noted by Jenkins et al. (2005) regarding the Hertz-Mindlin (1949) assumption.

1.7 CONCLUSIONS

The unified effective medium model brings together two models thought to be different, but as described here, are shown to be similar. Each relies on a different assumption, but as shown earlier, though having a different mathematical expression, each can be converted to the other with a simple transformation. The Walton model consists of an equation for an infinitely rough sphere and another equation for a perfectly smooth sphere, whereas the Dvorkin-Nur model has been defined only for an infinitely rough sphere. The equation for the Dvorkin-Nur model can be transformed to the infinitely rough sphere of the Walton model, and vice-versa.

Part of the motivation here is to re-emphasize that the Jenkins model connects the end points represented by the Walton model. By showing that the Dvorkin-Nur model connects to the infinitely rough sphere end point of Walton, all the gas hydrate work on the Dvorkin-Nur model becomes useable with the Jenkins model; i.e., the extended Walton model. An important conclusion of this paper is that the Dvorkin-Nur model, is the rough sphere model endpoint of the extended Walton model.

A direct comparison of the synthetic and measured velocity logs provides valuable insight to validate the unified effective medium model for gas hydrates in sediments. Recognizing the significance of the Hertz-Mindlin type effective medium models for gas hydrates in unconsolidated sediments, we incorporate the previous efforts into a single "unified" model and define a common nomenclature. Though we attempt to assign a single friction coefficient value to each Hydrate Window, it is not surprising that in a real and heterogeneous environment, the value might vary with depth as it does here at the larger spatial scales. At the smaller spatial scales we also see good correlation

except the amplitudes of the small scale features are greater for the synthetic data than for the measured data.

TABLE III. Bulk Modulus, Shear Modulus, and Density

	Bulk Modulus (GPa)	Shear Modulus (GPa)	Density (g/cc)
Gas hydrate	5.6	2.4	0.90
Ice	8.8	3.9	0.92
Water	2.3	0.0	1.04
Quartz	36.0	45.0	2.65
Clay	21.0	7.0	2.60
Methane	0.1	0.0	0.235
Pore fluid	2.60		

ACKNOWLEDGEMENTS

We thank Dr. Diana Sava and the three additional anonymous reviewers for their valuable comments. We, also, thank Dr. Warren Wood from the U. S. Naval Research Laboratory, Stennis Space Center, MS for his discussions and insights during development of the model. We thank the Gulf of Mexico-Hydrates Consortium (GoMHRC), the Bureau of Ocean Energy Management (BOEM) of the U. S. Department of the Interior, and U. S. Department of Energy for funding support. Also, we thank Elizabeth Yankovsky for providing Figure 1. The first author would also like to thank the State of South Carolina for providing a Senior Fellowship.

APPENDIX A

COORDINATION NUMBER

Jenkins et al. (2005, p. 211) concludes from statistical modeling that "The average strain assumption provides a relatively good approximation to the bulk modulus and a relatively poor assumption to the shear modulus" (Jenkins, 2005, p. 211). We surmise from this that the Hertz-Mindlin model, developed for normal compression, is less reliable when extended to oblique compression than originally assumed.

Recent studies (Dutta, 2009; Zhang et al., 2013) argue that the statistical model results of Jenkins et al. (2005) can be obtained with the extended Walton model by incorporating the coodination number as a function of porosity or pressure. In Figure A-1 four models considered for use in the unified model are shown. At first glance and at the low end of the porosity scale, the models from Dutta (2009) seem the most realistic given that the coordination numbers (average of compressional and shear) around 12+, which is considered a theoretical max for the coordination number. However, Dutta (2009) does not provide any guidance for using in practical models such as considered in this paper where higher porosities are considerd. A similar argument applies to the model from Smith et al. (1929). We then went back to the standard model from Mavko et al. (1998), based on Murphy (1982), and applied linear extrapolations to pick up the lower and higher porosities needed for the simulations.

According to Murphy (1982, p.53), at high pressures near and above 15 MPa, the coordination number loses its dependence on pressure and becomes a simple function of porosity. Rather than trying to resolve the subtleties of the models we rely on the

assertion in Murphy (1982) that at high effective pressure the coordination number becomes independent of the pressure at 8.5.

To model the coordination number as a function of porosity Bachrach and Avseth (2008, p. E201) recommends the model provided in Mavko et al. (1998, p. 150, Figure 5.2.2) based on Murphy (1982). Mavko et al. (1998) provides a model of coordination number as a function of porosity that is suitable for inclusion in the unified model. The changes that result from inclusion of the coordination number as a function of porosity were insignificant for the cases we ran.

Both Dutta (2009) and Zhang et al. (2013) investigate the coordination number as a function of pressure. Though we quickly realized, these models are not relevant to the immediate need, we show their models in Figure A-2 because the differences in their results show there is still much to learn in the topic of coordination numbers. Both of their models for the compressional wave coordination numbers have the same shape but differ by a value of approximately 3.2. For the shear wave compressional numbers, the Zhang model is much steeper than the Dutta model, and the models also cross each other at a pressure of 10 MPa. The more important difference is that in the models for Dutta (2009), the coordination number is always greater than the shear wave coordination number; for Zhang et al. (2013), the opposite is true. There is still much that is unresolved in modeling coordination numbers in practical effective medium models.

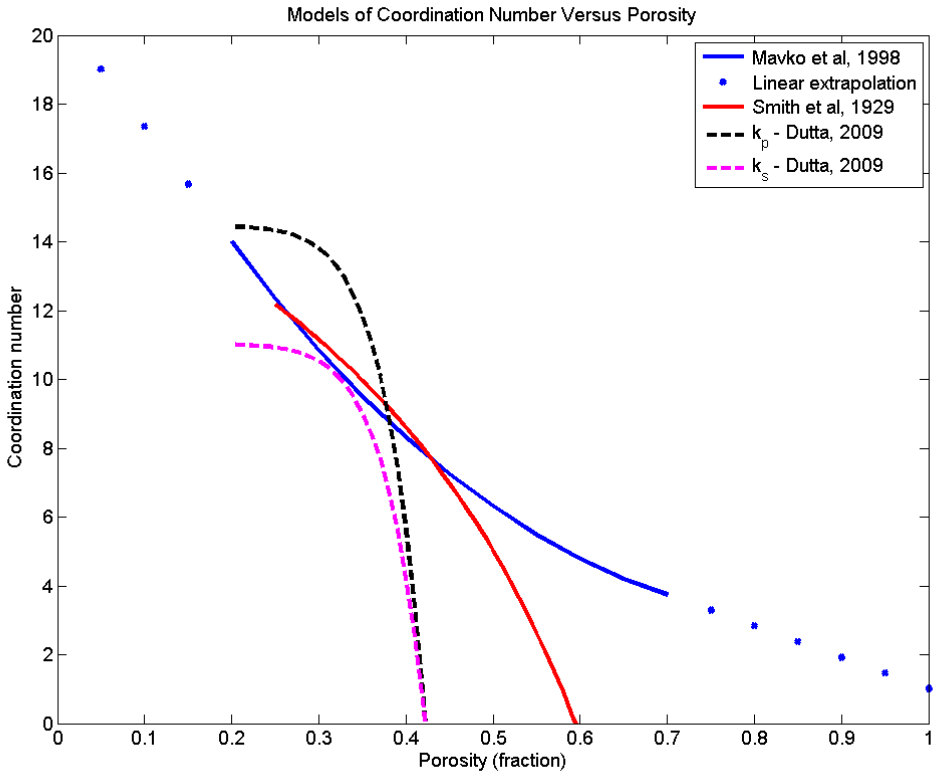

Figure A-1. Models of Coordination Number Versus Porosity: Blue solid line based on Mavko et al. (1998); blue dots are linear extrapolations from Mavko et al. (1998); red solid line is based on Smith et al. (1929); and black and magenta dashed lines, respectively, based on Dutta (2009) for compressional and shear wave coordination numbers.

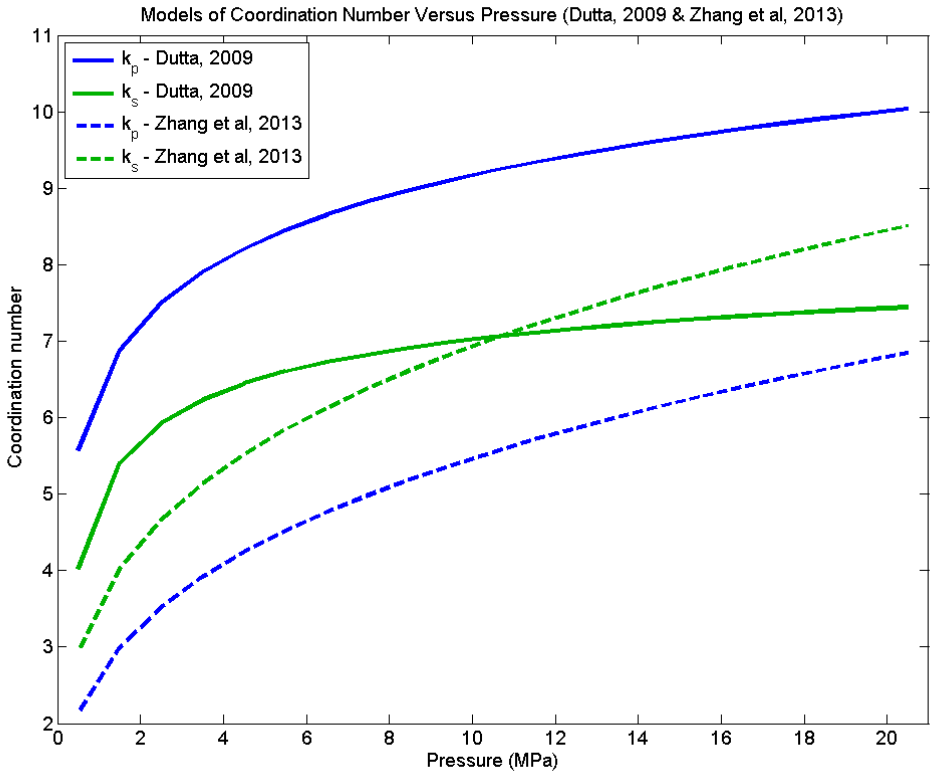

Figure A-2. Models of Coordination Number Versus Pressure: Blue lines are for the compressional wave coordination numbers; Dutta (2009) – solid line, and Zhang et al. (2013) – dashed line. Green lines are for the shear wave coordination numbers; Dutta – solid line, and Zhang et al., – dashed line.

NOMENCLATURE

a	=	Principal major axis of ellipse
b	=	Principal minor axis of ellipse
B	=	Coefficient defined in text
C	=	Coefficient defined in text
C_s'	=	Tangential compliance with slip
C_x'	=	Tangential compliance without slip
e	=	Strain tensor
f	=	Volume fraction
f_h	=	Volume fraction, hydrate
G	=	Shear modulus, solid phase
G_{Dry}	=	Shear modulus, dry frame
G_h	=	Shear modulus for hydrate
G_{HM}	=	Effective shear modulus, Hertz-Mindlin
G_s	=	Shear modulus, mixed solid grains
G_{Sat}	=	Shear modulus, saturated frame
k	=	Average number of contacts per grain (coordination number)
k^*	=	Effective bulk modulus, extended model
K	=	Bulk modulus, solid phase
K_{Dry}	=	Bulk modulus, dry frame
K^E	=	Effective bulk modulus
K_f	=	Bulk modulus, pore fluid
K_h	=	Bulk modulus for hydrate

K_{HM} = Effective bulk modulus, Hertz-Mindlin

K_s = Bulk modulus, mixed solid grains

K_{Sat} = Bulk modulus, saturated frame

K_w = Bulk modulus for water

p = Normal pressure on the contact surface

P = Hydrostatic pressure

P_x = Tangential force x-component

P_z = Tangential force z-component

S_h = Volumetric concentration, hydrate

S_w = Water saturation of pore space

u = Normal displacement

u' = Tangential displacement

v = Solid volume fraction

V_p = P-wave velocity

V_s = S-wave velocity

x = x-component position

y = y-component position

α = Strength of transverse stiffness, or friction parameter

δ_x' = Displacement variable

λ = Lamé coefficient

λ^* = Effective Lamé coefficient, extended model

λ^E = Effective Lamé coefficient, extended model

μ = Shear modulus of the grain material

μ^* = Effective shear modulus, extended model

μ^E = Effective shear modulus, extended model

ν = Poisson's ratio of the grain material

π = Pi

ϕ = Porosity

ϕ_c = Critical porosity

ϕ_h = Hydrate volume fraction

ϕ_r = Reduced porosity

ρ_B = Bulk density

ρ_f = Fluid density

ρ_h = Hydrate density

$\rho_{r-solid}$ = Density (reduced–solid volume fractions)

ρ_{solid} = Solid phase density

ρ_w = Water density

REFERENCES

Bachrach R. and Avseth P., 2008, Rock physics modeling of unconsolidated sands: Accounting for nonuniform contacts and heterogeneous stress fields in the effective media approximation with applications to hydrocarbon exploration: Geophysics, **73** (6), E197-E209.

Bernal J. D. and Mason J., 1960, Packing of spheres: Co-ordination of randomly packed spheres: Nature, **88**, 910-911.

Brandt H., 1955. A study of the speed of sound in porous granular media: Journal of Applied Mechanics, **22**, 479-486.

Collett T. S., Lewis R. E. and Dallimore S. R., 2005. JAPEX/JNOC/GSC et al. Mallik 5L-38 gas hydrate production research well downhole well-log and core montages, *in* S. R. Dallimore and T. S. Collett, eds., Scientific Results from the Mallik 2002 Gas Hydrate Production Research Well Program, Mackenzie Delta, Northwest Territories, Canada: Geological Society of Canada, Bulletin **585**, 23.

Collett T. S., Lewis R. E., Dallimore S. R., Lee M. W., Mroz T. H. and Uchida T., 1999. Detailed evaluation of a gas hydrate reservoir properties using JAPEX/JNOC/GSC Mallik 2L-38 gas hydrate research well downhole well-log displays, in S. R. Dallimore, T. Uchida, and T. S. Collett, eds., Scientific Results from the PAPEX/JNOC/GSC Mallik 2L-38 Gas Hydrate Research Well, Mackenzie Delta, Northwest Territories, Canada: Geological Survey of Canada, Bulletin **544**, 295-311.

Cordon I., Dvorkin J. and Mavko G., 2006. Seismic reflections of gas hydrate from perturbational forward modeling: Geophysics, **71** (6), F165-F171.

Dai J.; Snyder F., Gillespie D., Koesoemadinata A. and Dutta N., 2008. Exploration for gas hydrates in the deepwater, northern Gulf of Mexico: Part I: A seismic approach based on geologic model, inversion, and rock physics principles: Marine and Petroleum Geology, **25**, 830-844.

Dai J., Xu H., Snyder F. and Dutta N., 2004. Detection and estimation of gas hydrates using rock physics and seismic inversion: Examples from the northern deepwater Gulf of Mexico: The Leading Edge, **23**, 60-66.

Dallimore S.R., and Collett T. S., eds., 2005. Scientific Results from the Mallik 2002 Gas Hydrate Production Research Well Program, Mackenzie Delta, Northwest Territories, Canada: Geological Survey of Canada, Bulletin **585**, 890 p.

Deresiewicz H., 1958. Stress-strain relations for a simple model of a granular medium: Journal of Applied Mechanics, **25**, 402-406.

Digby P. J., 1981. The effective elastic moduli of porous granular media: Journal of Applied Mechanics, **48**, 803-808.

Duffy J. and Mindlin R. D., 1957. Stress-strain relations and vibrations of a granular medium: Journal of Applied Mechanics, **24**, 585-503.

Dutta T., 2009. Integrating Sequence Stratigraphy and Rock-Physics to Interpret Seismic Amplitudes and Predict Reservoir Quality: Ph.D. Dissertation, Stanford University, August 2009, 173.

Dvorkin J. and Nur A., 1996. Elasticity of high-porosity sandstones: Theory for two North Sea data sets: Geophysics, **61** (5), 1363-1370.

Dvorkin, J., Prasad M., Sakai A. and D. Lavoie, 1999. Elasticity of marine sediments: Rock physics modeling: Geophysical Research Letters, **26** (12), 1781-1784.

Gassmann F., 1951. Uber die elastizitat poroser medien: Vierteljahrsschrift der Naturforschenden Gesellschaft in Zurich, **96**, 1–23.

Han D.-H. and Batzle M. L., 2004. Gassmann's equation and fluid-saturation effects on seismic velocities: Geophysics, **69** (2), 398-405.

Hashin Z. and Shtrikman S., 1963. A variational approach to the theory of the elastic behaviour of multiphase materials: Journal of the Mechanics and Physics of Solids, **11**, 127-140.

Helgerud M. B., 2001. Wave Speeds in Gas Hydrate and Sediments Containing Gas Hydrate: A Laboratory and Modeling Study: Ph.D. Dissertation, Stanford University, April 2001, 249.

Helgerud M. B., Dvorkin J., Nur A., Sakai A. and Collett T., 1999. Elastic-wave velocity in marine sediments with gas hydrates: Effective medium modeling: Geophysical Research Letters, **26** (13), 2021-2024.

Hill R., 1952. The elastic behavior of crystalline aggregate: Proceedings of the Physical Society, London, **A65**, 349-354.

Jenkins J., Johnson D., La Ragione L. and Makse H., 2005. Fluctuations and the effective moduli of an isotropic, random aggregate of identical, frictionless spheres: Journal of the Mechanics and Physics of Solids, **53**, 197-225.

Mavko G., Mukerji T. and Dvorkin J., 1998. The Rock Physics Handbook: Tools for Analysis in Porous Media: Cambridge University Press, 329.

Mindlin R. D., 1949. Compliance of elastic bodies in contact: Journal of Applied Mechanics, **16**, 259-268.

Murphy W. F., 1982. Effects of Microstructure and Pore Fluids on the Acoustic Properties of Granular Sedimentary Materials: Ph.D. Dissertation, Stanford University, June 1982, 255.

Sava D. and Hardage B., 2006a. Rock physics models of gas hydrates from deepwater, unconsolidated sediments: SEG/New Orleans 2006 Annual Meeting, Expanded Abstracts, 1913-1917.

Sava D. and Hardage B., 2006b. Rock physics characterization of hydrate-bearing deepwater sediments: The Leading Edge, **25**, 616-619.

Scott G. D., 1960. Packing of spheres: Packing of equal spheres: Nature, **188**, 908-909.

Smith W. O., Foote P. D. and Busang P. F., 1929. Packing of homogeneous spheres. Physical Review, **34**, 1271-1274.

Sriram, G., Dewangan P. and Ramprasad T., 2014, Modified effective medium model for gas hydrate bearing, clay-dominated sediments in the Krishna-Godavari Basin: Marine and Petroleum Geology, **58**, 321-330.

Walton K., 1978. The oblique compression of two elastic spheres: Journal of the Mechanics and Physics of Solids, **26**, 139-150.

Walton K., 1987. The effective elastic moduli of a random packing of spheres: Journal of the Mechanics and Physics of Solids, **35**, 213-226.

Xu H., Dai J., Snyder F. and Dutta N., 2004. Seismic detection and gas hydrates using rock physics and inversion, *in* C. E. Taylor and J. T. Kwan, eds., Advances in the Study of Gas Hydrates: Kluwer Academic, 117-139 (Chapter 8).

Zhang Z., Han D.-h., and McConnell D. R., 2013. Characterization of elastic properties of near-surface and subsurface deepwater hydrate-bearing sediments: Geophysics, **78** (3), D169-D179.

CHAPTER II

SUBSPACE SOLUTIONS FOR SEISMIC VELOCITY ANALYSIS

Terry, Darrell A.; Yankovsky, Elizabeth A.; Knapp, Camelia C.; 2019. Subspace Solutions for Seismic Velocity Analysis. Manuscript, 34 p., 10 Figures.

ABSTRACT

Conventional semblance for seismic velocity analysis does not have the resolving power of Eigenstructure methods due to the inclusion of the noise-signal space in conventional semblance. For nearly three decades subspace, or Eigenstructure, techniques have been investigated as alternatives to conventional semblance for computing seismic velocity spectra, but still receive little use in seismic applications due to their high computational costs. Seismic velocity analysis using Eigenstructure techniques has developed along two approaches. These approaches include the so-called hybrid approach in which the conventional semblance coefficient is reformulated using Eigen analysis. In a second more direct approach, Eigen analysis and MUSIC techniques are used to define a coherency measure. The hybrid and direct approaches both use Eigen decomposition based on computing the spatial data covariance matrix, or the so-called matrix outer product. In a typical application for seismic velocity analysis, in

which the spatial dimension of the problem is significantly greater than the temporal domain, the solution for the seismic velocity spectra is computationally intensive. Although smoothing techniques and partial stacking have been used to lower the computational cost, the hybrid and direct Eigenstructure approaches have still seen limited use.

In this paper we discuss our efforts to develop an Eigen decomposition approach for seismic velocity spectra based on computing the temporal covariance data matrix as an intermediate step to efficiently compute the Eigenvectors of the spatial covariance data matrix. This greatly reduces the computational costs, and avoids the uncertainties of data smoothing, the difficulties of partial stacking, and the use of specialized algorithms to find the lowest order Eigenvalues. This paper provides a proof-of-concept for implementing an alternative Eigenstructure technique using the temporal covariance data matrix. We apply our approach to the so-called hybrid algorithm and compare our results to the conventional semblance and to the original hybrid algorithm directly calculating the spatial covariance data matrix. We show that by switching to the temporal-covariance formulation the computational cost of the Eigen decomposition is greatly reduced. Then using a simple matrix relationship we are able to calculate the needed Eigenvectors for the spatial-covariance formulation. A solution with the resolution of the spatial data covariance matrix is obtained with the lower computational cost of a temporal covariance data matrix solution, and therefore, is competitive to conventional semblance in computational cost. This alternative algorithm is applicable to direct approaches to calculate coherency measures for seismic velocity. Our approach benefits

recent efforts to develop a temporal approach to calculate coherency measures for seismic velocity analysis.

KEYWORDSs: Semblance, subspace, Eigenstructure, seismic, velocity, hybrid.

2.1 INTRODUCTION

The conventional semblance coefficient (Neidell and Taner, 1971) is widely used today to compute the seismic velocity spectra. Several algorithms have also been developed for computing the semblance coefficient in specialized cases, as well as suggested improvements for conventional semblance (Abbad and Ursin, 2012). Of the latter we specifically note Luo and Hale (2012) which significantly improves velocity resolution, but at great computational cost. Over the years, alternatives to the conventional semblance coefficient have been proposed, but none have received general acceptance. One noted deficiency of the conventional semblance coefficient is the inability to properly separate noise and signal subspaces (Shan et al, 1985; Kirlin, 1992); Eigenstructure techniques separate noise from signal subspaces, and therefore have been proposed as alternatives to the conventional semblance coefficient (Bondi and Kostov, 1988). Conventional semblance for seismic velocity analysis does not have the resolving power of Eigenstructure methods due to the inclusion of the noise within the signal subspace.

Eigenstructure techniques are typically divided into the so-called hybrid approaches to calculate an alternative semblance coefficient or into direct approaches to calculate a coherence measure. Kirlin (1992) first presented a formulation of the conventional semblance coefficient in terms of the data covariance measure in which the

conventional semblance coefficient is reformulated using Eigen analysis. In the direct approach Key and Smithson (1990) proposed a time-domain Eigenstructure technique to define a coherence measure. Similarly, MUSIC techniques are also used to define a coherence measure (Williams et al, 1988; Wang et al, 2001; Asgedom et al, 2011).

The hybrid and direct approaches both use Eigen decomposition based on computing the spatial data covariance matrix, or so-called matrix outer product. In a typical application for seismic velocity analysis, in which the spatial dimension of the problem is significantly greater than the temporal domain, the solution for the seismic velocity spectra is computationally intensive. Though smoothing techniques, partial stacking, and specialized algorithms for finding the lowest order Eigenvalues have been used to lower the computational cost, the hybrid and direct approaches have still seen limited use.

Despite expectations of improved velocity resolution, time domain direct Eigenstructure approaches have not been widely used, largely due to their increased computational times. Li and Liu (1999) proposed a frequency domain Eigenstructure approach that does not require Eigen decomposition. Even though frequency domain approaches, coupled with MUSIC, significantly reduce computational cost below that of even conventional semblance, these also have not been widely used because, while showing much promise, these have not yet been fully developed.

Based on this review, we chose to investigate the hybrid approach (Kirlin, 1992) as a test bed for an alternative Eigenstructure technique. In Kirlin (1992) the conventional semblance coefficient is reformulated in an Eigen analysis notation using the outer product of the data matrix. In our alternative Eigenstructure technique we show

how to compute the Eigenvectors for the spatial analysis using the inner product of the data matrix. We discuss insights and progress made to reduce the computational cost for performing the hybrid Eigenstructure approaches. This approach should be fully adaptable to the direct Eigenstructure technique described in Key and Smithson (1990). We also argue that this alternative algorithm is adaptable to the various direct approaches (Wang et al, 2001) and the most recent paper by Barros et al (2015). We do not discuss non Eigen decomposition approaches, such as Li and Liu (1999), further.

We discuss our efforts to develop an Eigen decomposition approach for seismic velocity spectra based on computing the temporal covariance data matrix as an intermediate step for computing the spatial covariance data matrix. This greatly reduces the computational intensity and avoids the uncertainties of data smoothing, the difficulties of partial stacking, and the use of specialized algorithms to find the lowest order Eigenvalues.

This paper provides a proof-of-concept for implementing an alternative Eigenstructure technique using the temporal covariance data matrix. We apply our approach to the so-called hybrid algorithm (Kirlin, 1992) and compare our results to the conventional semblance and to the original hybrid algorithm implemented using the spatial covariance data matrix. We show that by switching to the temporal covariance data matrix the computational cost of Eigen decomposition is greatly reduced; then using a simple matrix relationship we are able to calculate the needed Eigenvectors for the for the spatial covariance data matrix. A solution with the resolution of the spatial covariance data matrix is obtained with the lower computational cost of a temporal covariance matrix solution, and therefore, is competitive with conventional semblance in

computational cost. This alternative algorithm is applicable to direct approaches to calculate coherency measures for seismic velocity; we believe our approach would improve the effort of Barros et al (2015) to develop a temporal approach for calculating coherency measures for seismic velocity analysis. The approach discussed here is many times more computationally efficient than the spatial covariance data matrix, yet allows the spatial Eigenvectors to be calculated.

In section 2 of this paper we reformulate the conventional semblance algorithm and the covariance data matrix algorithms to a common nomenclature and notation. First the conventional semblance of Neidell and Taner (1971) is reformulated in this common notation. Then we describe the mathematical distinction between the spatial covariance data matrix and the temporal covariance data matrix. This includes reformulating the equations for solving the hybrid approach using the basic equations outlined in Kirlin (1992). Then, we describe the alternative hybrid approach that utilizes the temporal covariance data matrix to greatly reduce the computational cost.

Section 3 is used to compare conventional semblance results against the hybrid algorithm and our alternative hybrid semblance using a high resolution, industry quality data set from the central Aleutian Basin of the Bering Sea (Scholl et al, 2012). First we show Eigenvalue and Eigenvector results for the hybrid approach of Kirlin (1992); then we the compare the Eigenvectors of the spatial covariance data formulation results with the temporal covariance data results. Finally, we show that the Eigenvectors for the spatial covariance approach can be recovered from the temporal Eigenvectors. We also compare results from the velocity spectra for all three approaches.

In section 4 we discuss our results and suggest additional directions to further develop this alternative approach. We comment on the recent paper by Barros et al (2015) which also develops an Eigen decomposition approach based on the temporal covariance data matrix. Their paper applies the analysis to both the hybrid and direct approaches. We argue that our temporal approach should be used in their direct approaches to the coherence measure.

2.2 ALGORITHMS

This section is used to reformulate seismic velocity analysis as a multichannel signal-noise subspace problem. We begin by reformulating the mathematical description for the conventional semblance coefficient from Neidell and Taner (1971). Then we present a reformulation of Kirlin's (1992) formulation of the conventional semblance coefficient as a subspace-semblance coefficient; this has sometimes been referred to as a hybrid formulation of semblance.

Each paper previously mentioned uses a different notation for matrices and indexes. Kirlin (1992, eqn. 2) reverses the indices in the subscripts for the semblance equation from the notation in Neidell and Taner (1971, eqn. 11). Other conventions are found in Key and Smithson (1990) and Barros et al (2015). These reformulations are used to establish our notation, and carry that notation consistently into the subspace techniques. This insures a consistent notation throughout.

We use a bold, upper case **X** to represent a two-dimensional seismic data matrix. If we let time represent the row dimension i, and let columns j represent the spatial dimension, individual components of the two dimensional matrix are $x_{i,j}$. Then we can represent row and column vectors, respectively, as $\mathbf{x}_i = \left(x_{i,1}\ x_{i,2}\ x_{i,3}\ \ldots\ x_{i,N}\right)$ and $\mathbf{x}_j^T =$

$(x_{1,j}\ x_{2,j}\ x_{3,j}\ \ldots\ x_{M,j})$, where M is an odd number of samples in the time gate and N is the number of data channels.

2.2.1 Conventional Semblance

The semblance coefficient is defined to be the normalized output/input energy ratio. Under an assumption that the noise sum over all channels at any time is zero, the semblance coefficient is equal to the ratio of the signal energy over the total energy (Neidell and Taner, 1971).

In our notation the equation for the conventional semblance coefficient from Neidell and Taner (1971, eqn. 11) becomes:

$$A = \sum_{i=k-(M/2)}^{k+(M/2)} \left\{ \sum_{j=1}^{N} x_{i,j(i)} \right\}^2 \tag{1a}$$

$$B = N \sum_{i=k-(M/2)}^{k+(M/2)} \sum_{j=1}^{N} x_{i,j(i)}^2 \tag{1b}$$

Then, referring to the convention semblance coefficient as $S_c = A/B$, we have

$$S_c = \sum_{i=k-(M/2)}^{k+(M/2)} \left\{ \sum_{i=1}^{N} x_{i,j(i)} \right\}^2 \Big/ N \sum_{i=k-(M/2)}^{k+(M/2)} \sum_{j=1}^{N} x_{i,j(i)}^2 \tag{2}$$

The index k is the global index in the temporal domain to reference the center of the time gate.

2.2.2 Eigenstructure Semblance

Kirlin (1992) defines the covariance data matrix as the outer product of the data matrix. Yet it is also possible to define a covariance data matrix as the inner product of the data matrix. To distinguish between these approaches, we define a spatial covariance data matrix and a temporal covariance data matrix as follows.

Forming the outer product, we define the spatial covariance data matrices as:

$$\widehat{\mathbf{R}}_k = \mathbf{X}^H \mathbf{X} = \sum_{i=k-M/2}^{k+M/2} \mathbf{x}_i^H \mathbf{x}_i = \sum_{i=1}^{M} \mathbf{x}_i^H \mathbf{x}_i \tag{3}$$

where, on the right-hand-side, the vector products of the row vectors defined above are summed over the number of samples in the temporal window. This spatial data covariance matrix is $N \times N$ in size. Recognize that it is best to define the length of the time gate M as odd; in the first summation above we reference the local temporal index i to the global temporal index k; in the second summation, the local index is independent of the global index.

Then, to form the inner product to define the temporal covariance data matrix, we write

$$\hat{\mathbf{r}}_k = \mathbf{X}\,\mathbf{X}^H = \sum_{j=1}^{N} \mathbf{x}_j\,\mathbf{x}_j^H \tag{4}$$

Here, on the right-hand-side, the vector products of the column vectors defined above are summed over the number of spatial samples. This temporal data covariance matrix is $M \times M$ in size, with the indices being $i = k - M/2, \ \ldots, -1, 0, 1, \ldots, k + M/2$, or $i = 1, 2, 3, \ldots, M$ with M odd using the local index temporal frame.

2.2.3 Spatial covariance data matrix formulation

In this section, using the notation defined for this paper, we reformulate Kirlin's (1992) hybrid approach using a spatial covariance data matrix. As first shown in Kirlin (1992), and recently in Barros et al (2015), the conventional semblance coefficient can be rewritten in matrix form

$$S_c = \frac{\mathbf{1}_N^T \widehat{\mathbf{R}}_k \mathbf{1}_N}{M \, Tr\left[\widehat{\mathbf{R}}_k\right]} \tag{5}$$

where we have the identity vector $\mathbf{1}_N^T = [1 \ \ 1 \ \ 1 \ldots n \ \ldots \ 1]$ for $n = 1, 2, 3, \ldots, N$; and $Tr\left[\widehat{\mathbf{R}}_k\right]$ represents the trace of the spatial covariance data matrix. After Eigen decomposition to find the Eigenvalues of $\widehat{\mathbf{R}}_k$, we write the numerator as

$$\mathbf{1}_N^T \widehat{\mathbf{R}}_k \mathbf{1}_N = \sum_{j=1}^{N} \lambda_j \mathbf{1}_N^T \mathbf{u}_j \mathbf{u}_j^H \mathbf{1}_N \tag{6}$$

We can separate the right-hand-side into signal and noise subspaces, and rewrite the previous equation as

$$\mathbf{1}_N^T \widehat{\mathbf{R}}_k \mathbf{1}_N = \sum_{j=1}^{M} \lambda_j \mathbf{1}_N^T \mathbf{u}_j \mathbf{u}_j^H \mathbf{1}_N + \sum_{j=M+1}^{N} \lambda_j \mathbf{1}_N^T \mathbf{u}_j \mathbf{u}_j^H \mathbf{1}_N \quad (7)$$

Here, the columns of the matrix **U** are the Eigenvectors of the spatial data covariance matrix $\widehat{\mathbf{R}}_k$. As will become more clear later, the magnitudes of the Eigenvalues associated with the signal separate well from the Eigenvalues of the noise.

2.2.4 Reformulation with the temporal data covariance matrix

Analysis for semblance with the spatial data covariance matrix has shown that all the information content is contained within the first M Eigenvectors. Yet we quickly learned that reproducing the analysis from above using the temporal covariance data matrix is insufficient to correctly produce the semblance map.

The temporal covariance data matrix $\hat{\mathbf{r}}_k$ should contain all the information necessary to obtain the semblance coefficient, but we have not been able to write an explicit equation for S_c as a function of $\hat{\mathbf{r}}_k$. However, in this section we present an ad hoc approach using the temporal covariance data matrix that successfully models the semblance map and is much more computationally efficient than using the spatial covariance data matrix. If we perform an Eigen decomposition on the temporal covariance data matrix $\hat{\mathbf{r}}_k$ we get up to M Eigenvalues κ_j with M respective Eigenvectors $\mathbf{v}_j$, the latter of size $1 \times M$. For our definitions of $\widehat{\mathbf{R}}_k$ and $\hat{\mathbf{r}}_k$ the Eigenvalues have the special relationship $\kappa_j = \lambda_j$ for $j = 1, 2, 3, \ldots, M$; however, the Eigenvectors are significantly different in size. Therefore, $\mathbf{v}_j \neq \mathbf{u}_j$. However, we have learned through experimentation and the suggestion in Barros et al (2015) that we can recover, or calculate, the set of Eigenvectors **U** through the relationship

$$\mathbf{U} = \mathbf{X}^T\mathbf{V} \tag{8}$$

For the individual Eigenvectors $\mathbf{u}_j$, we write this as

$$\mathbf{u}_j = \mathbf{X}^T\mathbf{v}_j \tag{9}$$

Computationally, this is of value in many calculations for seismic velocity analysis if $M \ll N$.

By inspection we can write our semblance equation for the temporal data covariance matrix as follows. For the numerator, taking $j = 1, 2, 3, \dots, M$ and calculating $\mathbf{u}_j$ from the relationship above

$$A = \sum_{j=1}^{M} \kappa_j \mathbf{1}_N^T \mathbf{u}_j \mathbf{u}_j^H \mathbf{1}_M \tag{10}$$

For the denominator, using our definitions of $\widehat{\mathbf{R}}_k$ and $\hat{\mathbf{r}}_k$, we also have $Tr\left[\widehat{\mathbf{R}}_k\right] = Tr[\hat{\mathbf{r}}_k]$, therefore

$$B = N\, Tr[\hat{\mathbf{r}}_k] \tag{11}$$

Therefore

$$S_c = \sum_{j=1}^{M} \kappa_j \mathbf{1}_N^T \mathbf{u}_j \mathbf{u}_j^H \mathbf{1}_M \Big/ N\, Tr[\hat{\mathbf{r}}_k] \tag{12}$$

2.3 NUMERICAL SOLUTIONS

We provide a brief overview of the multichannel data set then describe the results generated from the conventional semblance algorithm compared against the spatial- and temporal-covariance approaches.

2.3.1 Data set from the central Aleutian Basin

For example calculations, we use an industry standard long offset, multichannel marine seismic data set acquired onboard the R/V Markus G. Langseth for the U.S. State Department's project for the third round of the Law-of-the-Sea Treaty (Scholl et al, 2012). The central Aleutian Basin beneath the Bering Sea is speculated to contain methane gas hydrates in high abundance. Fifteen multichannel seismic lines were acquired in this area in August 2011.

In Figure 1 we introduce the data set used in our numerical demonstration. Shotgather 1800 from Line 9A is shown in Figures 1 (b) and 1 (c). We also show pseudo seismic sections from the near and far-offset channels in Figures 1 (d) and 1 (a), respectively. A Butterworth bandpass filter from 12.5 to 125 Hz has been applied. For display the data has been clipped at ± 6.5 to provide optimum visualization of the reflectors; yellow is used to highlight negative excursions and red for positive excursions. In the near offset pseudo seismic section [Figure 1 (d)], the sea bottom is recognizable at approximately 5100 sec. The acoustic basement varies across the line, but is found at approximately 7500 to 7700 sec. Plume-like structures are noticed at shotgathers 1200,

1375, 1600, 1700, 1900, and 2225. These plume-like structures are speculated to be caused by the presence of buoyant methane gas. The data excursions seen at 5,550 ms are likely part of a bottom simulating reflector (BSR) marking the upward extent of methane gas transport and possibly precipitation into gas hydrate. The dark reflector at approximately 6200 sec is likely the BSR marking the CT Transition. With the other subfigures we can follow these features into the shotgather and into the far-offset pseudo seismic section [Figure 1 (a)]. As the reflection characteristics change with offset, the CT Transition becomes much more prominent at just greater than 8,000 ms in Figure 1 (a); the methane hydrate BSR is prominent at approximately 7,700 ms.

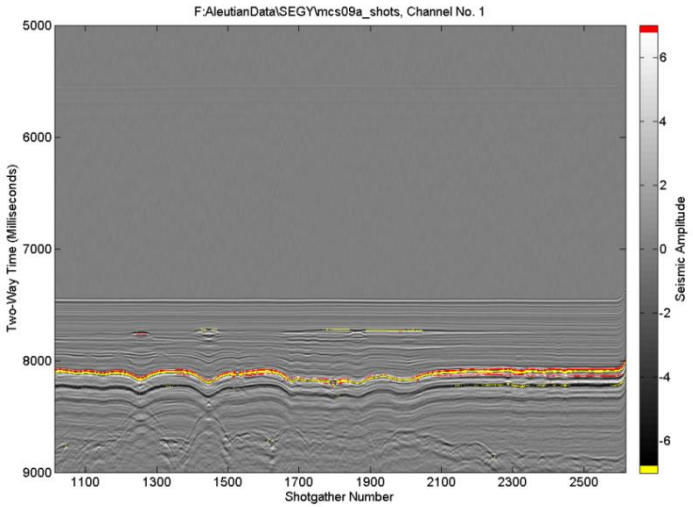
F:AleutianData\SEGY\mcs09a_shots, Channel No. 1
Two-Way Time (Milliseconds)
Shotgather Number
Seismic Amplitude

a)

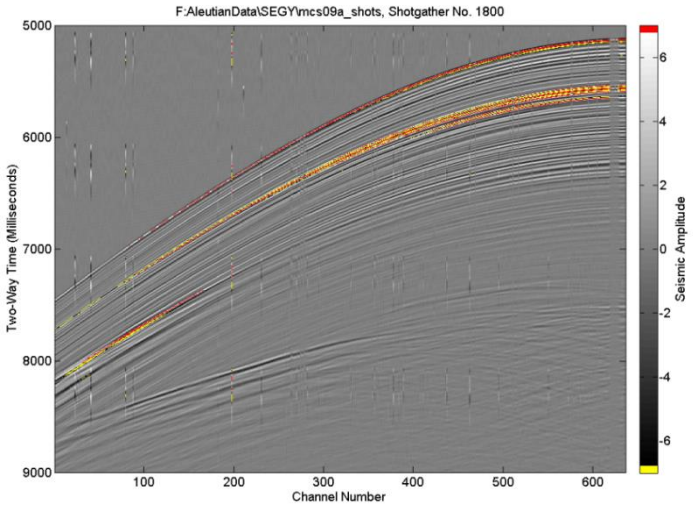
F:AleutianData\SEGY\mcs09a_shots, Shotgather No. 1800
Two-Way Time (Milliseconds)
Channel Number
Seismic Amplitude

b)

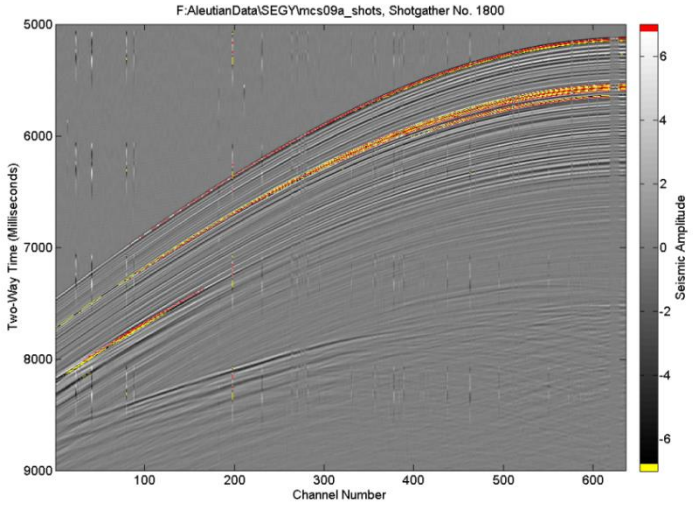
F:AleutianData\SEGY\mcs09a_shots, Shotgather No. 1800
Two-Way Time (Milliseconds)
Channel Number
Seismic Amplitude

c)

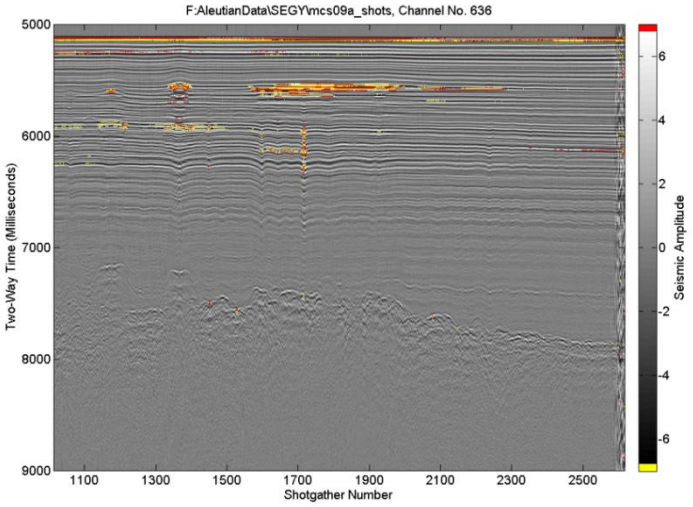
F:AleutianData\SEGY\mcs09a_shots, Channel No. 636
Two-Way Time (Milliseconds)
Shotgather Number
Seismic Amplitude

d)

Figure 1. Multichannel marine seismic data from the central Aleutian Basin of the Bering Sea, Cruise MGL1111 Line 9A (R/V Marcus G. Langseth, 18 August 2011), tying events of the near offset and far offset through the shotgather: a) seismic section created from far offset channel; b) shotgather 1800; c) shotgather 1800 (same as b); d) seismic section created from near offset channel.

To adequately represent the source wavelet in our semblance coefficient calculations we chose to use a sampling window of 25 representing 50 ms of two-way travel time. Results from computing the velocity spectra using the conventional semblance algorithm of Neidell and Taner (1971) are shown in Figure 2. Figure 2 (a) presents the semblance velocity spectra in an image plot of Two-Way Travel Time versus Average Velocity. Recall from the conventional semblance equation that the semblance coefficient is just the nondimensional ratio of the signal energy divided by the total energy; respectively we show these in Figures 2 (c) and 2 (b). The semblance velocity spectra of Figure 2 (a) is the baseline we will use to compare against our Eigen analysis results. Surprisingly we find high correlation of the sea bottom reflector and the methane hydrate BSR reflector with features in the total energy (TE) and signal energy (SE) spectra. There is only mild correlation with the CT Transition BSR at 6,200 ms; and additional energy is seen at 5,900 ms.

2.3.2 Comparison of Spatial and Temporal Solutions (Eigenvalues and Eigenvectors)

We discuss the results in Figures 3 thru 6 here. In Figures 3 and 4 we focus on the results of the spatial analysis. Then in Figure 5 and 6 we compare the results of the spatial analysis with the temporal analysis.

Results for Kirlin's (1992) hybrid approach with spatial data covariance matrix. Results from our spatial analysis are shown in Figures 3 and 4. Figure 3 shows the basic Scree plots in linear and semi-log y plots. Alternative Scree plots are shown in Figure 4 to visually separate signal from noise based on the Eigenvalue index.

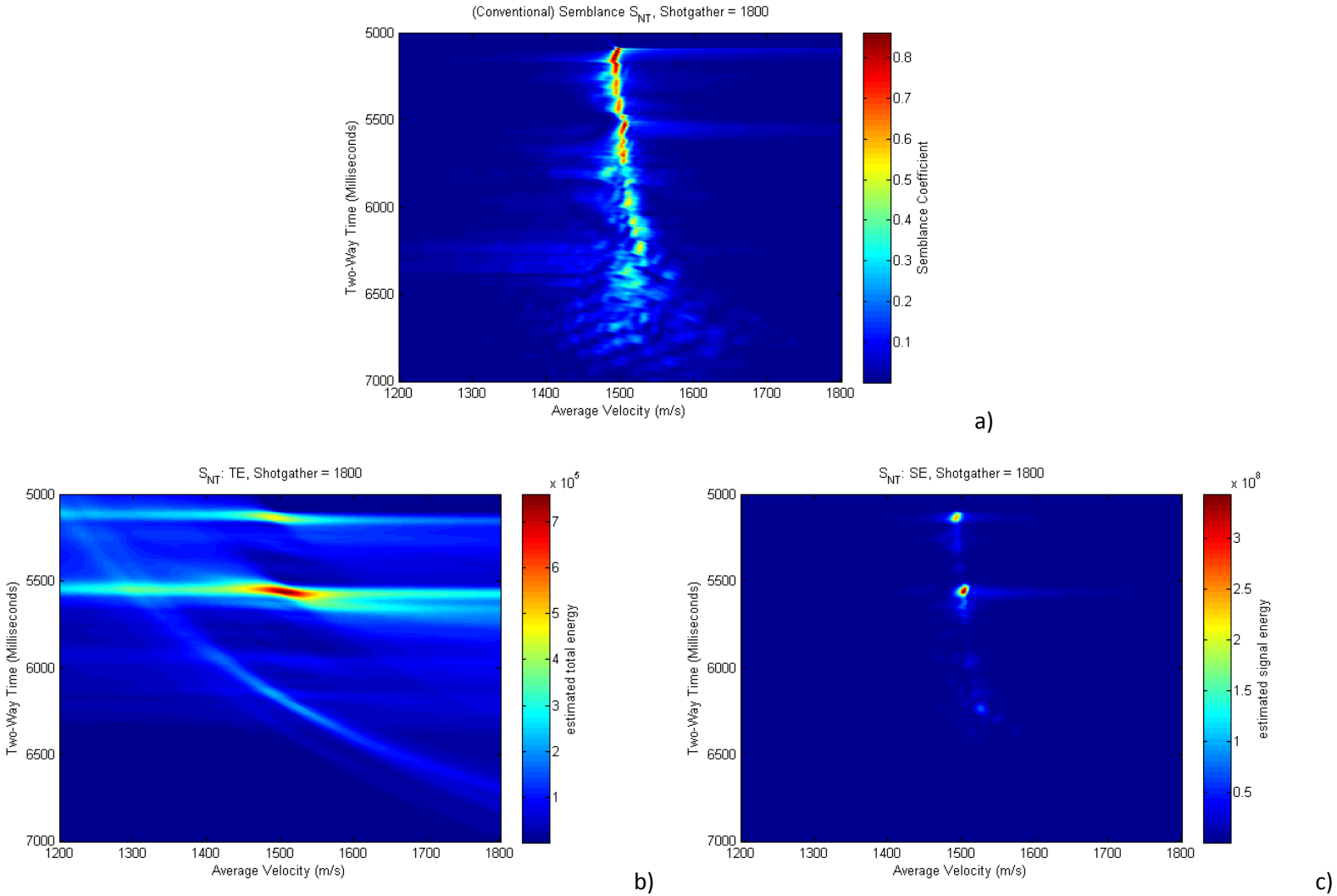

Figure 2. Conventional semblance analysis: a) conventional semblance velocity spectra; b) total energy; c) signal energy.

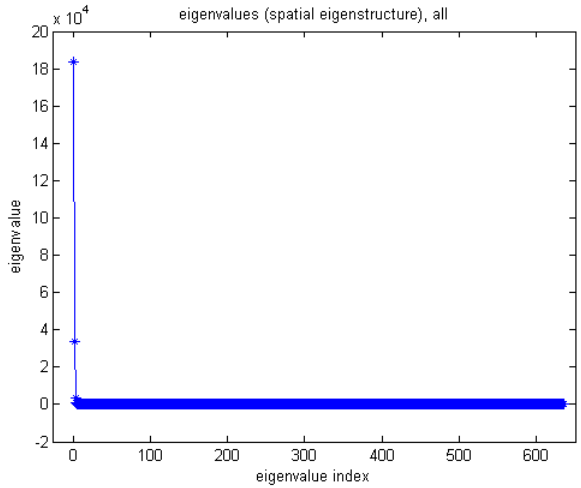
eigenvalues (spatial eigenstructure), all
x 10^4
eigenvalue
eigenvalue index

a)

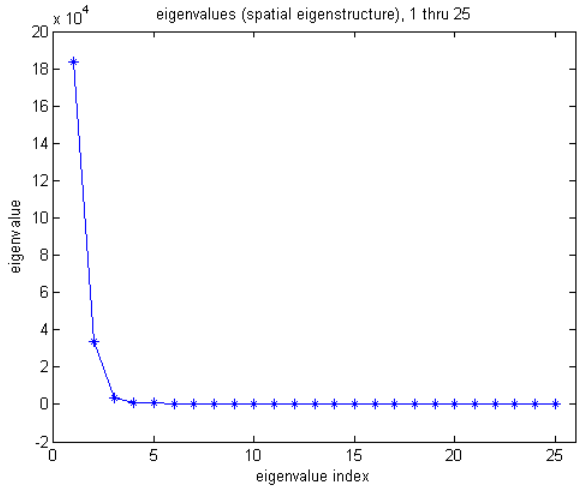
eigenvalues (spatial eigenstructure), 1 thru 25
x 10^4
eigenvalue
eigenvalue index

b)

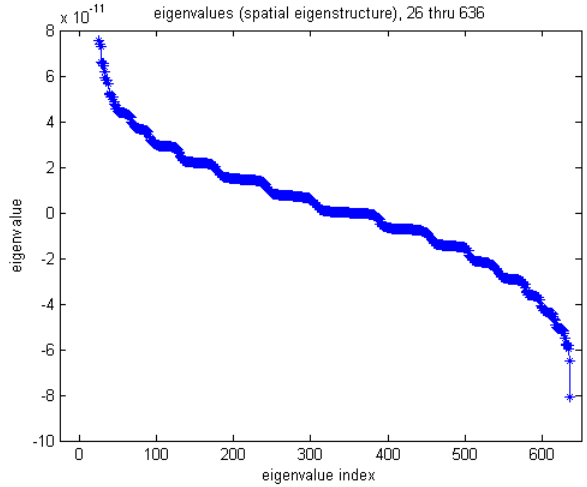
eigenvalues (spatial eigenstructure), 26 thru 636
x 10^-11
eigenvalue
eigenvalue index

c)

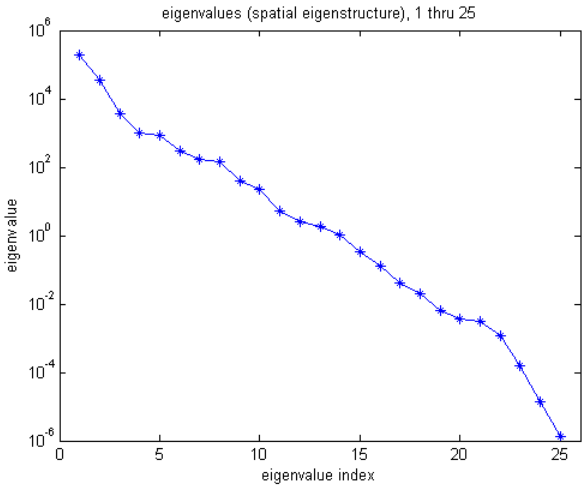
eigenvalues (spatial eigenstructure), 1 thru 25
eigenvalue
eigenvalue index

d)

Figure 3. Eigen analysis for the spatial data covariance matrix (Part I): a) scree plot for all 636 Eigenvalues; b) scree plot for the 25 largest Eigenvalues; c) scree plot for Eigenvalues order 26 thru 636; d) semi-log (y) scree plot for the 25 largest Eigenvalues.

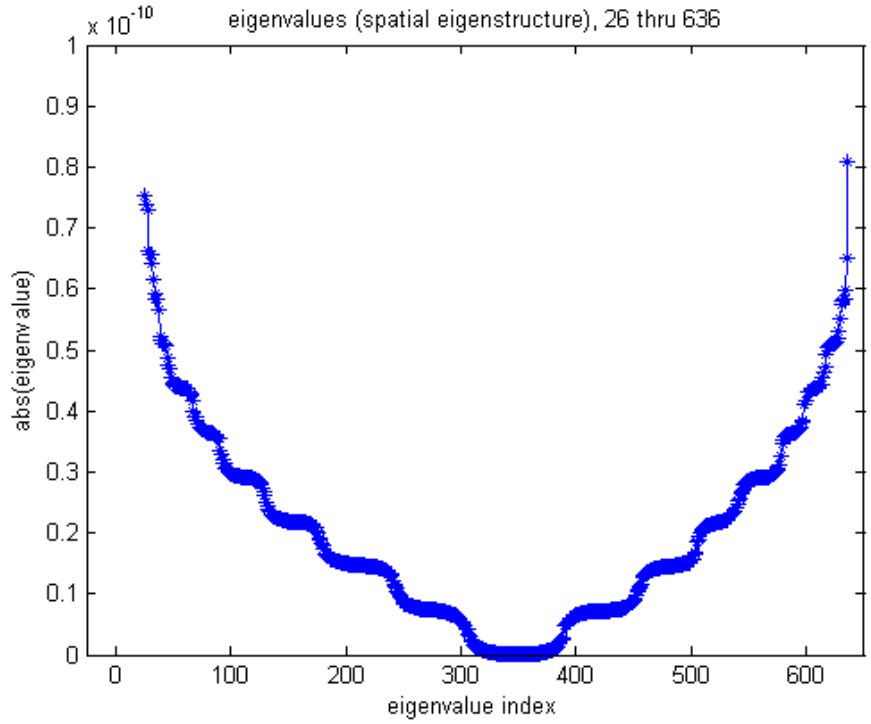

a)

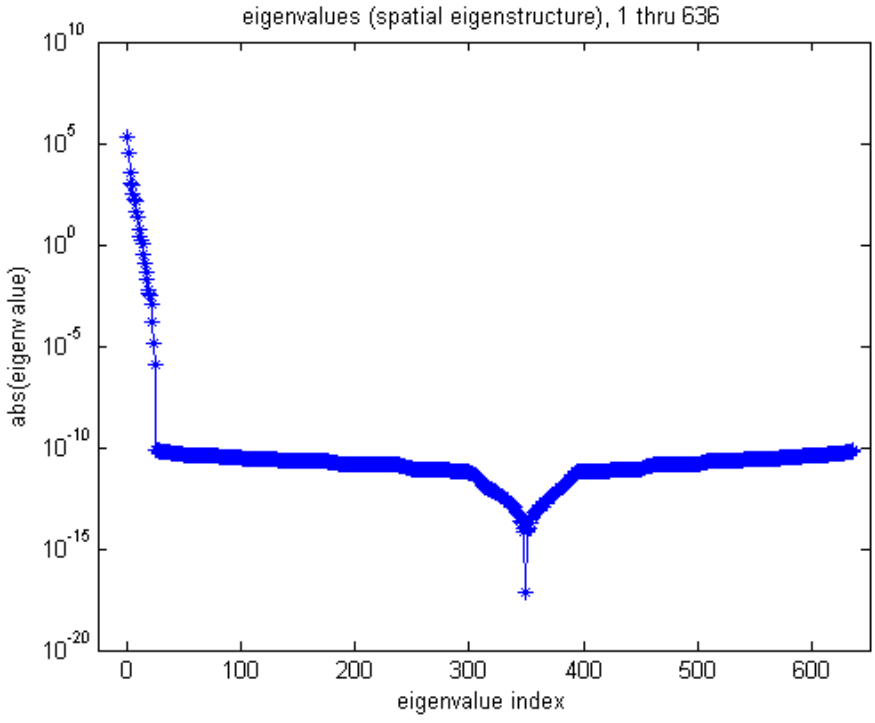

b)

Figure 4. Eigen analysis for the spatial data covariance matrix (Part II): a) scree plot of absolute value for Eigenvalues 26 thru 636 [same data as Figure 3 (c)]; b) semi-log (y) scree plot of absolute values for all 636 Eigenvalues. In both plots here, Eigenvalues above 349 are negative as shown previously in Figure 3 (c).

Figure 3 shows the Eigenvalues for the spatial data covariance formulation. In Figure 3 (a) is the typical Scree plot of Eigenvalue versus Eigenvalue index. We can only easily recognize three distinct Eigenvalues of the 636 Eigenvalues calculated. Figure 3 (b) is used to more closely look at the Eigenvalues 1 thru 25. In Figure 3 (c) we choose to look only at Eigenvalues 26 thru 636; results here suggest symmetric around zero in these for the higher index values. Displaying the Eigenvalues for the low index values with a semi-log y plot shows a clear linear trend in Figure 3 (d).

Figure 4 shows how the Eigenvalues separate into groups for the spatial covariance data matrix. Here we investigate symmetry and order-of-magnitude issues. Figure 4 (a) displays the absolute values for the same Eigenvalues previously shown in Figure 3 (c); except for the sign, the region from index 26 thru 348 is symmetric with the region from index 350 thru 636. In Figure 4 (b) we plot the absolute value of all Eigenvalues using a semi-log y plot; results show the Eigenvalues clearly separate into 3 groups; the first group is for index values 1 thru 25 to the upper far right of the subplot; the second group is in the lower left half of the subplot for index values 26 thru 348 or so; normally the third group cannot be shown on a semi-log y plot because the values are all negative for index 350 or so thru 636.

Results for our alternative hybrid approach with temporal data covariance matrix. Figure 5 compares the spatial and temporal Eigenvectors before translation of the temporal Eigenvectors. In Figure 5 we compare the Eigenvalues from the spatial-covariance Eigen analysis, Figure 5 (a), with the Eigenvalues from the temporal-covariance Eigen analysis, Figure 5 (c). The spatial-covariance Eigen analysis provides

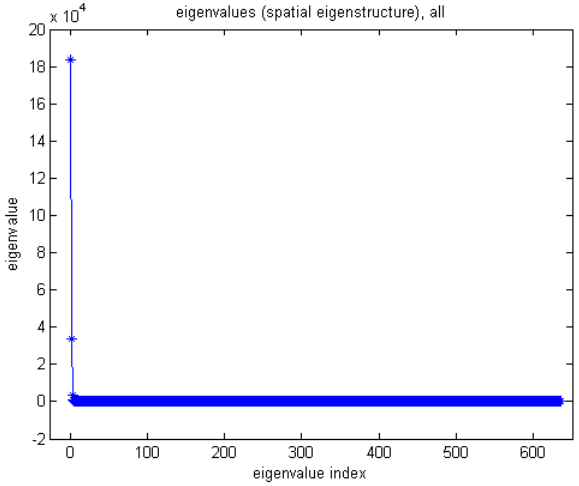
eigenvalues (spatial eigenstructure), all
x 10^4
eigenvalue
eigenvalue index

a)

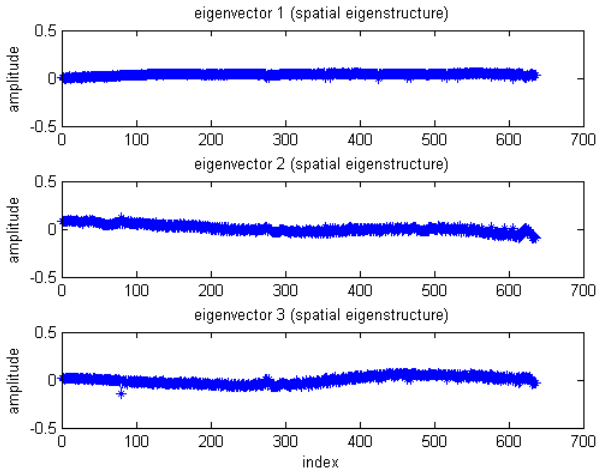
eigenvector 1 (spatial eigenstructure)
eigenvector 2 (spatial eigenstructure)
eigenvector 3 (spatial eigenstructure)
amplitude
index

b)

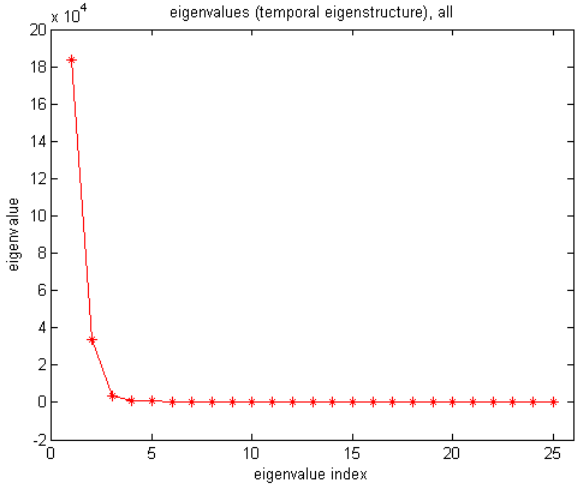
eigenvalues (temporal eigenstructure), all
x 10^4
eigenvalue
eigenvalue index

c)

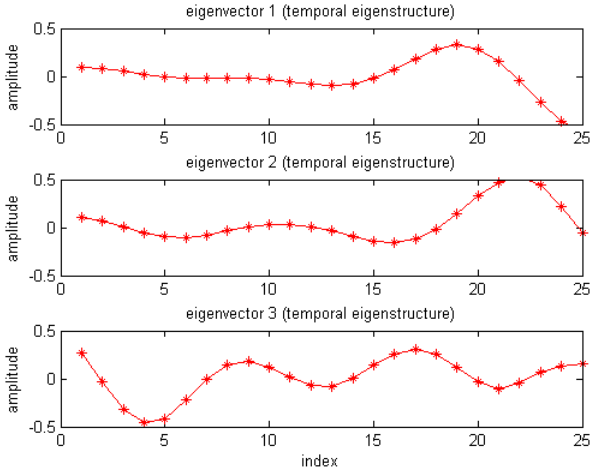
eigenvector 1 (temporal eigenstructure)
eigenvector 2 (temporal eigenstructure)
eigenvector 3 (temporal eigenstructure)
amplitude
index

d)

Figure 5. Comparison of the spatial (blue) with the temporal Eigen analysis velocity spectra (red): a) scree plot for all 636 Eigenvalues of spatial covariance data matrix; b) Eigenvectors for Eigenvalues 1 thru 3; c) scree plot for all 25 Eigenvalues of temporal covariance data matrix; d) Eigenvectors for Eigenvalues 1 thru 3.

636 Eigenvalues as we show earlier, whereas the temporal-covariance Eigen analysis provides only 25 Eigenvalues; though not readily apparent from these subplots, the 25 Eigenvalues from the temporal analysis are identical with the first 25 Eigenvalues from the spatial analysis. The spatial information contained within the Eigenvectors from the spatial analysis is much higher resolution than the spatial information contained within the Eigenvectors for the temporal analysis. This is readily apparent comparing Figure 5 (b) with Figure 5 (d) for the first three Eigenvectors.

Figure 6 compares the spatial and temporal Eigenvectors after translation. After we apply the translation relationship to the temporal Eigenvectors we again look at the results. In Figure 6 we directly compare Scree plots for Eigenvalues 1 thru 25 for both the spatial and temporal analysis in Figures 6 (a) and 6 (b), respectively. Likewise, we compare the Eigenvectors from the spatial and temporal analysis in Figures 6 (b) and 6 (d), respectively. From these displays we can see the results are essentially identical.

We have successfully generated the Eigenvectors of the spatial-covariance analysis by using the data matrix to translate the Eigenvectors from the temporal-covariance analysis; this was accomplished at a much lower computational cost than performing the full spatial-covariance analysis.

2.3.3 Comparison of Semblance Results (Conventional vs Spatial vs Temporal Covariance Semblance)

We also want to learn whether there is any deleterious effect on the semblance velocity spectra. Figure 7 compares the full semblance velocity/Eigen spectra for both the spatial and temporal analysis. The results show no discernable difference between the spatial covariance analysis and the temporal covariance analysis; see Figures 7 (a) and

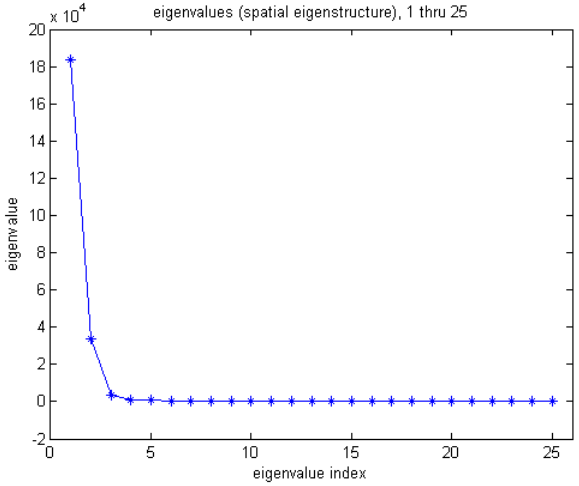
eigenvalues (spatial eigenstructure), 1 thru 25
x 10^4
eigenvalue
eigenvalue index

a)

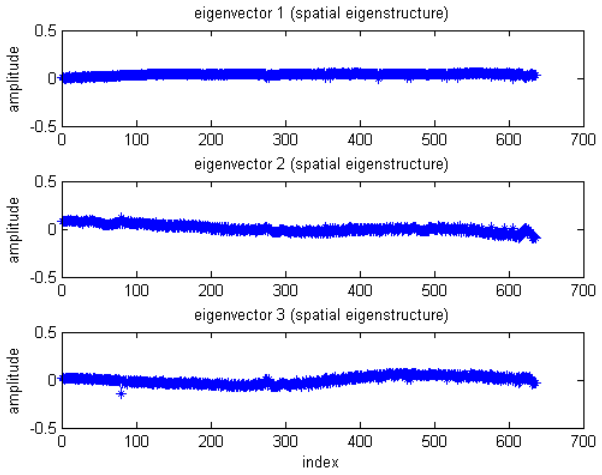
eigenvector 1 (spatial eigenstructure)
eigenvector 2 (spatial eigenstructure)
eigenvector 3 (spatial eigenstructure)
amplitude
index

b)

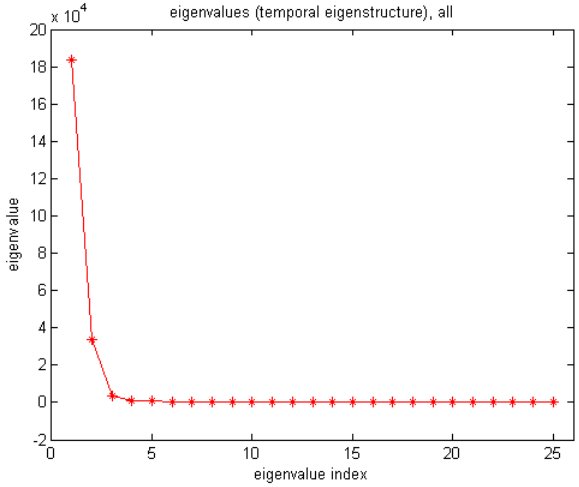
eigenvalues (temporal eigenstructure), all
x 10^4
eigenvalue
eigenvalue index

c)

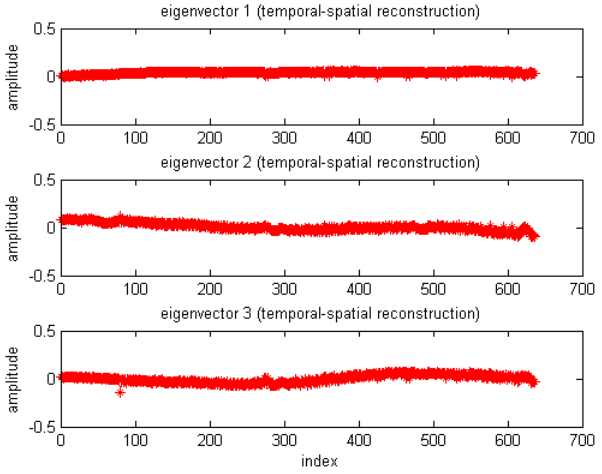
eigenvector 1 (temporal-spatial reconstruction)
eigenvector 2 (temporal-spatial reconstruction)
eigenvector 3 (temporal-spatial reconstruction)
amplitude
index

d)

Figure 6. Comparison of the spatial (blue) with the temporal Eigen analysis velocity spectra (red): a) scree plot for first 25 Eigenvalues of spatial covariance data matrix; b) Eigenvectors for Eigenvalues 1 thru 3; c) scree plot for all 25 Eigenvalues of temporal covariance data matrix; d) translated Eigenvectors for Eigenvalues 1 thru 3.

7 (b). Also, comparing these results with the conventional semblance velocity spectra of Figure 2 (a) we do not see any discernable differences.

We also want to review the results of the spatial and temporal covariance semblance coefficient for individual Eigen components. The results in Figure 7 are computed by summing the results of the 25 individual Eigen components. In Figures 8, 9, and 10 we investigate the Semblance velocity Eigen/spectra for the first 6 individual Eigen components. Since the spatial and temporal analysis results are essentially identical we only need to present results for the temporal analysis.

In Figure 8 we describe results for the temporal semblance velocity Eigen/spectra for Eigenvalues 1 and 2. As seen in Figure 8 (a), most of the signal energy is found in the velocity spectra for Eigenvalue 1. There are a few notable differences at 5,250, 5,800, and 6,400 ms. Also as expected, there is much less energy in the velocity spectra for Eigenvalue 2 seen in Figure 8 (b). The largest semblance coefficient is less than 0.3; there is some noticeable residual velocity from the seafloor down to 5,900 ms that appears to bleed over from Eigenvalue 1. In Figure 8 (b) we also see lower velocities from 5,800 down to 6,300 ms that are prominent in the display. Figure 9 shows the temporal semblance velocity Eigen/spectra for Eigenvalues 3 and 4. For Eigenvalue 3 in Figure 9 (a) we notice low velocity pockets near 5,300 and 5,400 msec. Residuals from the semblance velocity Eigen/spectra from Eigenvalue 1 are again noted from the seafloor down to about 6,300 ms. The semblance coefficient value is no greater than 0.14. Subplot does not show any notable pockets; the largest semblance coefficient is no greater than 0.07.

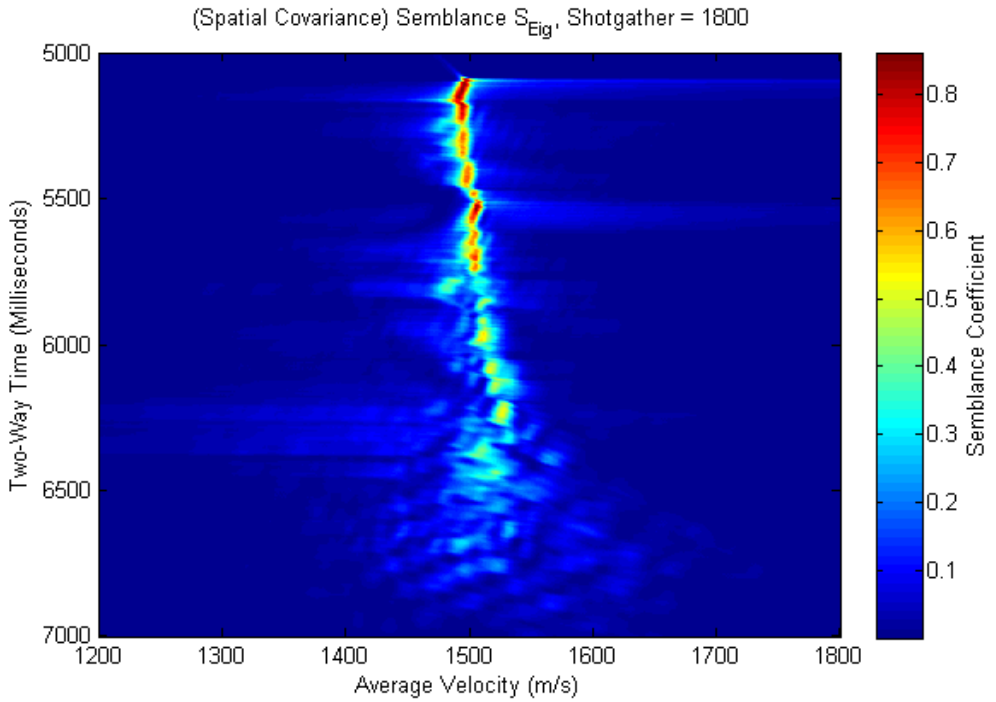

a)

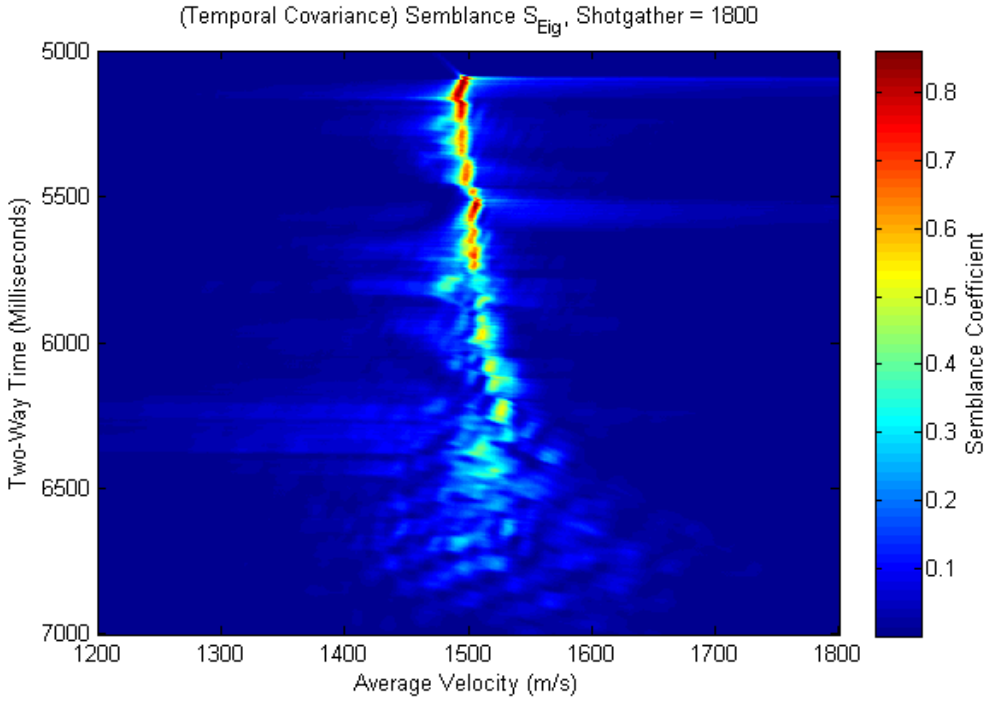

b)

Figure 7. Full spectrum semblance Eigen analysis: a) spatial covariance semblance velocity spectra; b) temporal covariance semblance velocity spectra.

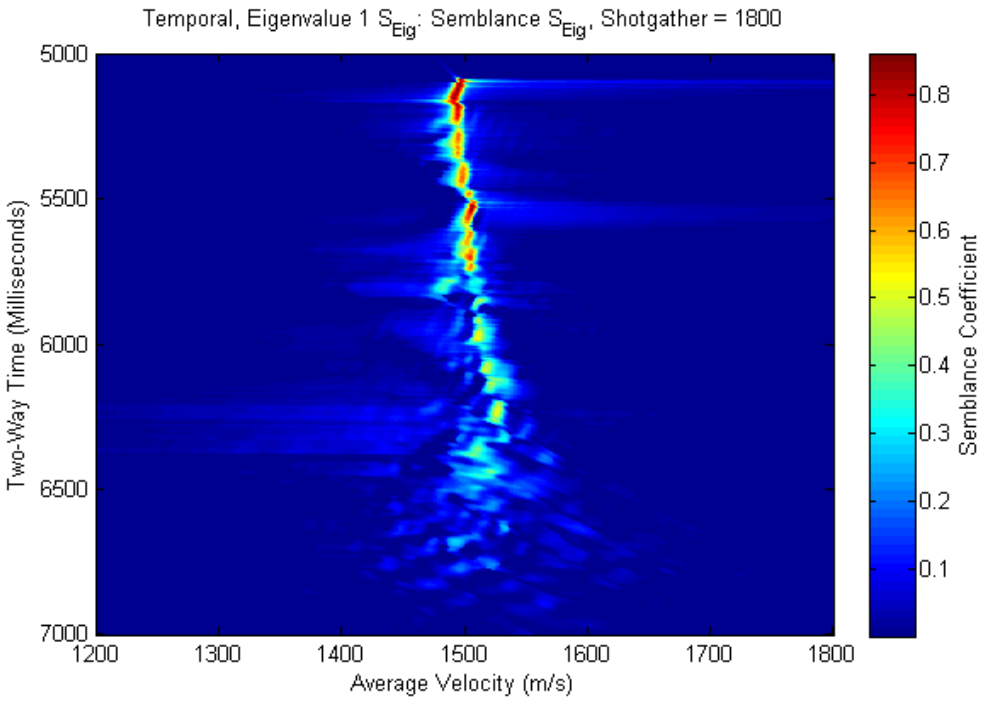

a)

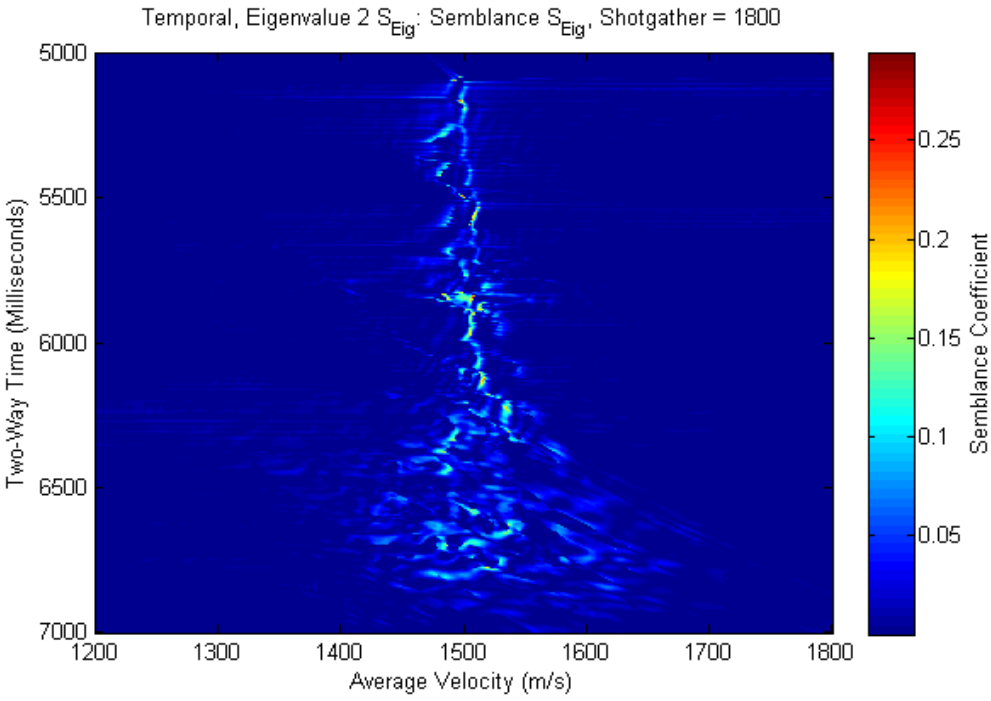

b)

Figure 8. Temporal covariance Eigen-Semblance velocity spectra results (Part I: a) Eigenvalue 1; b) Eigenvalue 2.

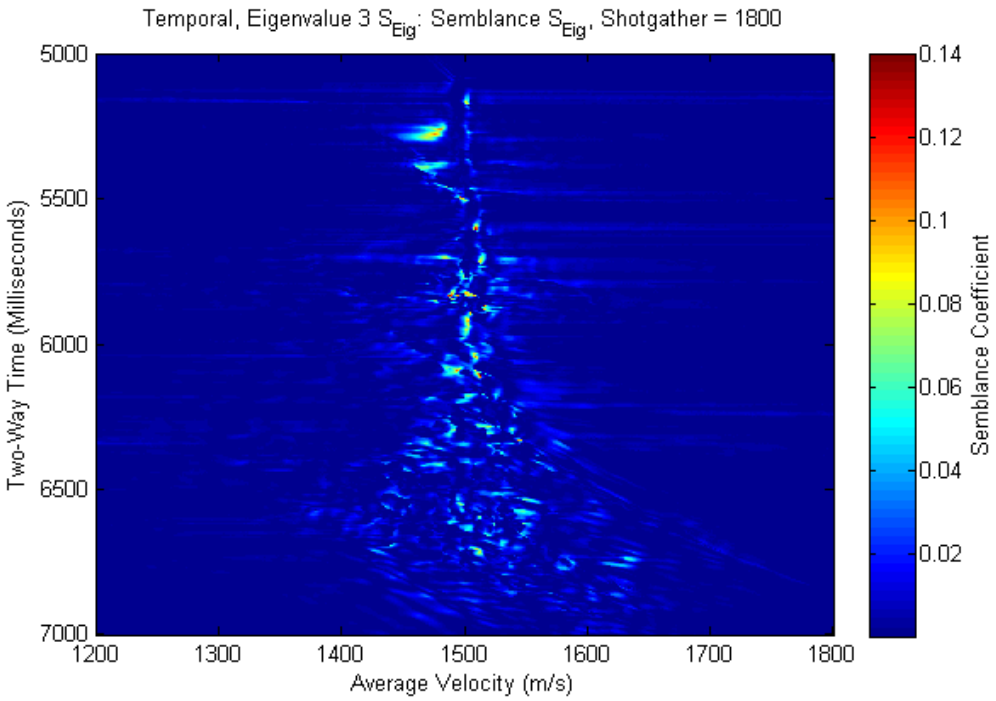

a)

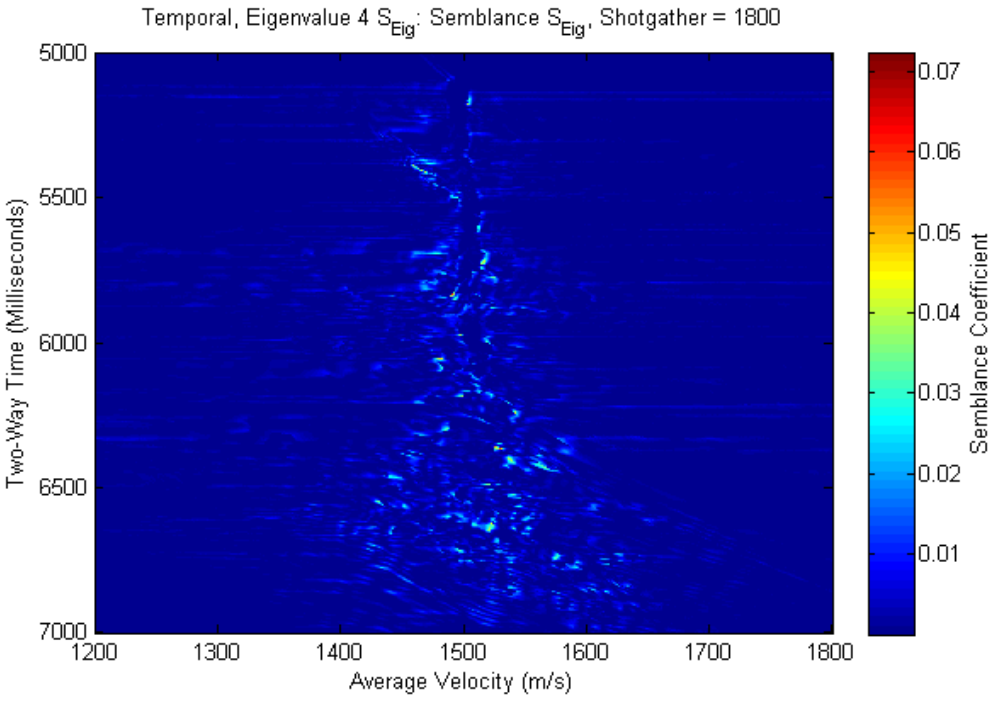

b)

Figure 9. Temporal covariance Eigen-Semblance velocity spectra results (Part II): a) Eigenvalue 3; b) Eigenvalue 4.

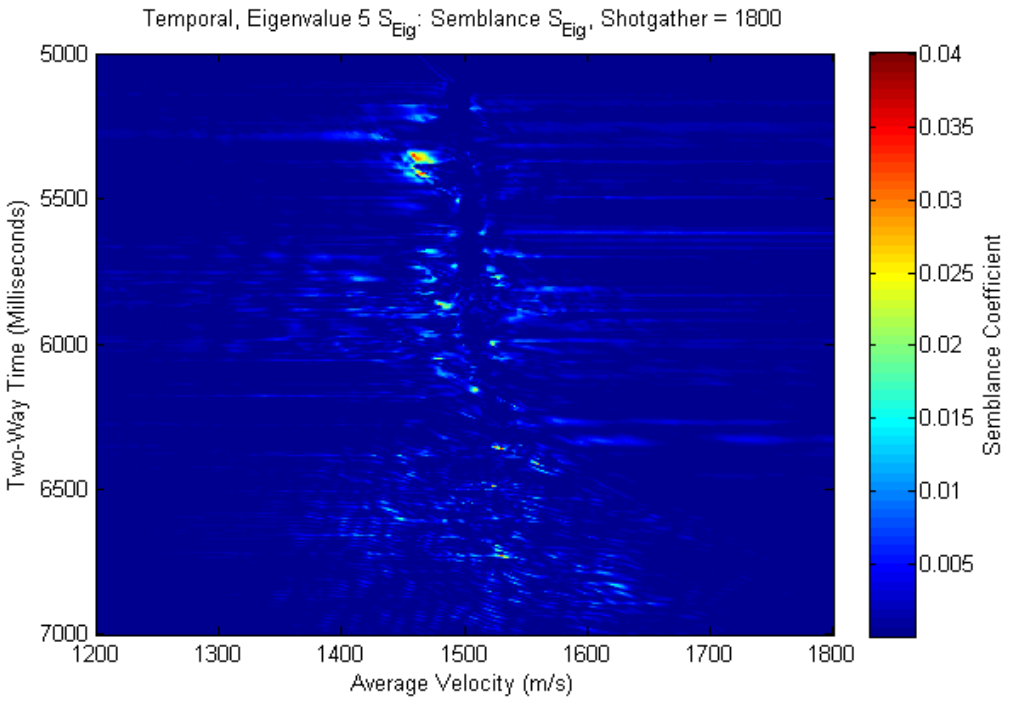

a)

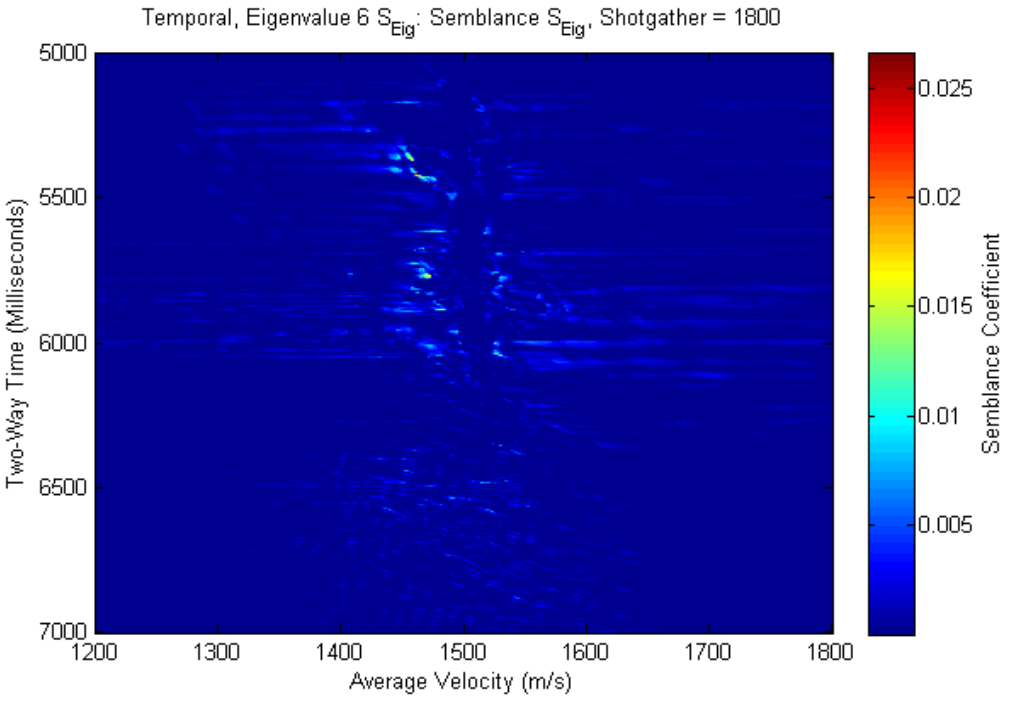

b)

Figure 10. Temporal covariance Eigen-Semblance velocity spectra results (Part III): a) Eigenvalue 5; b) Eigenvalue 6.

Finally, in Figure 10, we describe the temporal semblance velocity Eigen/spectra for Eigenvalues 5 and 6. The results for Eigenvalue 5 in Figure 10 (a) show low velocity pockets between 5,300 and 5,450 ms, but the semblance coefficient is no greater than 0.04. At this low value for the semblance coefficient the noise floor becomes more noticeable in the image display. A few minor low velocity pockets are noted in Figure 10 (b) for Eigenvalue 6.

2.4 DISCUSSION

This proof-of-concept paper shows that by computing the temporal covariance data matrix as an intermediate step we can compute the spatial-covariance Eigenvectors without the computational cost of performing the spatial covariance Eigen analysis. Instead the computational cost is greatly reduced and competitive with computing the conventional semblance coefficient. Without making any claims to having written efficient codes in MATLAB, we offer comparisons among the various algorithms' run times. Run times for the examples here for the conventional semblance coefficient were just over 20 minutes. The run times for the hybrid algorithm to calculate the Eigenstructure semblance coefficient took approximately 80 hours. Using the alternative hybrid approach of performing the temporal-covariance matrix analysis took in the neighborhood of 70 to 90 minutes.

This approach of substituting a temporal covariance data matrix for the spatial covariance data matrix should be easily adaptable to the direct approach of Key and Smithson (1990). We also believe there are important lessons from this effort that have implications for the results to calculate the coherency measure in Barros et al (2015). Part of the results in Barros et al (2015) define an analytical expression for a temporal

hybrid approach; though we have not shown our related work here, their result is incorrect. The relative success of their temporal coherency measure is a result of the superiority of their coherency measure algorithm despite an incorrect definition for their temporal analysis. Our results can be applied to the temporal coherency measure; the result should have the resolution of spatial coherency measure at the cost of their current temporal coherency measure.

The application here, and in Barros et al (2015), is for computation of seismic velocity analysis. However, results are not directly comparable. Not only are the data sets different, but we use a shot gather from a long array rather than a CMP gather. Also, we are less rigorous to properly align our normal moveout. While we apply a phase alignment, we do not apply a MUSIC algorithm. Also, we only use the real form of the data, while Barros et al (2015) likely used the analytic (or complex) form of the seismic data.

Barros et al (2015) shows how spatial covariance analysis can be applied to compute the conventional semblance coefficient with the hybrid approach from Kirlin (1992). They also define a coherence measure for a direct application of spatial covariance analysis. An important contribution of Barros et al (2015) is the attempt to apply temporal covariance analysis to the hybrid approach and to define the modified coherence measure. Though not shown in our paper here, the analytic equation shown in Barros et al (2015) does not successfully define a temporal-covariance equation. Here we take an ad hoc approach to apply temporal covariance data analysis to the hybrid approach; we are still searching to determine if an analytic form can be found. This ad hoc approach has important implications for the modified coherence measure of Barros et

al (2015). Barros et al (2015) show the value of the modified coherence measure. Even when using a temporal covariance analysis that is deficient, and likely incorrect, the velocity spectra look reasonable though degraded from their spatial covariance coherence measure. By switching to our alternative temporal covariance approach as an intermediate step to efficiently calculate the spatial covariance Eigenvectors, both the efficiency of the temporal-covariance algorithm and the resolution of the spatial-covariance algorithm can be realized. There are several important lessons learned from our effort:

1) The full non-noise Eigen spectrum (and Eigenvectors) for the spatial-covariance analysis is recovered from the temporal-covariance analysis (much less computational costs).
2) No data smoothing, no partial stacking, and no special algorithms to recover the lowest order Eigenvalues (much less preconditioning of data) are needed.
3) The equation in Barros et al (2015) for the semblance coefficient for the temporal covariance data matrix algorithm likely does not correctly recover the information content to be called a semblance coefficient;
4) We can recover that information, with minimal computational cost, using the matrix relationships between the spatial and temporal domains suggested by Barros et al (2015).

2.5 CONCLUSIONS

With this proof-of-concept presentation we have shown that an ad hoc algorithm allows for the successful use of a temporal covariance analysis. It is applicable to both hybrid and direct approaches. Improvements in our normal moveout alignment are

necessary to realize the full value of our approach. We also want to redevelop the algorithm for performing the velocity analysis with the analytic form of the seismic data.

Barros et al (2015) have made an important contribution with their modified spatial coherence measure for calculating the seismic velocity spectral map, but at great computational cost. Their attempt to develop the modified temporal coherence measure seems successful, particularly since the computational costs are more competitive with the computational cost of the conventional semblance coefficient. We want to apply our ad hoc analysis as an intermediate step in the modified temporal coherence measure calculations. This should achieve the competitive computational cost of the temporal-covariance analysis; after applying the translation to calculate the spatial Eigenvectors the results should have the precision of the modified spatial coherence measure.

Besides providing a higher resolution seismic velocity spectral map, Eigen-covariance analysis provides a richer insight to the data. With a temporal-covariance analysis that is competitive with the conventional semblance coefficient it is now feasible to further investigate this richness. The challenge now is to provide physical meaning to the additional low order Eigen-covariance seismic velocity spectra maps.

ACKNOWLEDGEMENTS

The MGL1111 multichannel seismic reflection data sets were made available to us through the courtesies of Dr. Ginger Barth, U. S. Geological Survey, and Dr. Warren Wood, Naval Research Laboratory, and the support of Rose Anne Weissel, Marine Geoscience Data System, LDEO, Columbia University.

REFERENCES

Abbad B. and Ursin B., 2012. High-resolution bootstrapped differential semblance. *Geophysics*, 77 (3), U39-U47.

Asgedom E. G., Gelius L. J. and Tygel M., 2011. High-resolution determination of zero-offset common-reflection-surface stack parameters. *Intern. J. Geophysics*., doi:10.1155/2011/819831, 10 pp.

Barros T., Lopes R. and Tygel M., 2015. Implementation aspects of eigendecomposition-based high-resolution velocity spectra. *Geophysical Prospecting*, v. 63, p. 99-115.

Biondi B. L. and Kostov C., 1989. High-resolution velocity spectra using eigenstructure methods. *Geophysics*, 54 (7), 832-842.

Key S. C. and Smithson S. B., 1990. New approach to seismic-reflection event detection and velocity determination. *Geophysics*, v. 55, n. 8, p. 1057-1069.

Kirlin R. L., 1992. The relationship between semblance and eigenstructrue velocity estimators. *Geophysics*, v. 57, n. 8, p.1027-1033.

Li F. and Liu H., 1999. Subspace based seismic velocity analysis (Chapter 7). In: Kirlin, R. L.; Done, W. J.; Editors, 1999. *Covariance Analysis for Seismic Signal Processing*. Geophysical Developments Series, No. 8, Society of Exploration Geophysicists, p. 109-140.

Luo S. and Hale D., 2012. Velocity analysis using weighted semblance. *Geophysics*, v. 77, n. 2, U15-U22.

Neidell N. S. and Taner M. T., 1971. Semblance and other coherency measures for multichannel data. *Geophysics*, v. 36, n. 3, p. 482-497.

Scholl D. W., Wood W. T., Barth G. A. and Childs J. R., 2012. The Bering Sea Basin: New drilling and geophysical observations and evidence for an important contribution of thermogenic methane to interstitial deposits of methane hydrate. *Eleventh International Conference on Gas in Marine Sediments, Nice, France, 4-7 September 2012*, p. 74.-77

Shan, T.-J., Wax M. and Kailath, T., 1985. On spatial smoothing for direction-of-arrival estimation of coherent signals. *IEEE Trans. ASSP*, ASSP-33 (4), 806-811.

Wang Y. Y., Chen J.-T. and Fang W. H., 2001. TST-MUSIC for joint DOA-delay estimation. *IEEE Trans. Signal Process.*, 49 (4), 721-729.

Williams R. T, Prasad S. and Mahalanabis A. K., 1988. An improved spatial smoothing technique for bearing estimation in a multipath environment. *IEEE Trans. ASSP*, ASSP-36 (4), 425-432.

CHAPTER III

IDENTIFICATION OF BOTTOM SIMULATING REFLECTORS IN FAR OFFSET SEISMIC IMAGES

Terry, Darrell A.; Knapp, Camelia C.; 2019. Identification of Bottom Simulating Reflectors on Far Offset Seismic Images. Manuscript, 33 p., 7 Figures.

ABSTRACT

The presence of marine gas hydrates is routinely inferred based on the identification of bottom simulating reflectors (BSRs) in common depth-point (CDP) seismic images. This has proven to be a cost-effective approach to identify the presence of marine gas hydrates. Additional seismic studies such as amplitude variation with offset (AVO) can be applied for corroboration. However, confirmation is needed by drilling and sampling. Here, the use of single channel far offset seismic images is investigated for what appears to be a more reliable and cost-effective indicator for the presence of bottom simulating reflectors than traditional CDP processing or AVO analysis. This approach may expand the envelope of environments under which the presence of marine gas hydrates may be identified. This investigation considers recently collected multi-channel seismic data from the deep waters of the central Aleutian Basin beneath the Bering Sea, the pre-processing of the data sets, and the methodology for processing and display to generate single

channel seismic images.

A non-traditional approach to processing seismic data is taken to be more relevant to gas hydrate imaging. Instead of applying the traditional CDP seismic processing workflows from the oil industry, we have chosen to more carefully review the significant amount of information existing in the data, and to explore how the character of the data changes as offset angle changes. Three cases are selected for detailed analysis. These include 1) stratigraphy running parallel with the ocean bottom; 2) a potential bottom simulating reflector, running parallel to the ocean bottom, and cross-cutting dipping reflections, and 3) a suspected thermal intrusion without a recognizable bottom simulating reflector. Descriptions are provided for the single channel near and far offset seismic images for these sample cases. Results indicate that BSRs related to marine gas hydrates, and originating due to the presence of free gas, are more easily and uniquely identifiable from single channel displays of far offset seismic images than from traditional CDP displays.

KEYWORDS: gas hydrates, bottom simulating reflector, seismic analysis, Aleutian Basin, far offsets

3.1 INTRODUCTION

Naturally occurring methane-hydrates have been the subject of study and interest since their prediction and discovery in the mid-1960s. Though indirect, seismic evidence has proven to be an effective economic methodology to determine the presence and the estimated volumes of marine gas hydrate resources. Results of previous analysis, regardless of the disagreements over the actual amounts, show the volume of hydrate resources to be enormous and nearly ubiquitous in the deep waters of the continental shelf areas. Over many decades it has been observed that marine gas hydrates are found in the shallow sediments of the deep ocean along continental margins. Both direct and indirect evidence has been used to determine or infer the

presence of marine gas hydrates. Their presence has been routinely inferred based on the identification of bottom simulating reflectors (BSRs) in common depth-point (CDP) seismic images (Kvenvolden and Lorenson, 2001, p. 7). The BSRs are high amplitude reflections of reverse polarity from the ocean bottom reflection that mark the bottom of the hydrate stability zone and meet additional criteria discussed later. The identification of BSRs has been especially valuable to assess the areal extent of marine gas hydrate deposits (Kvenvolden and Lorenson, 2001, p. 6, 7; see Sloan, 1998, p. 463 for a more detailed explanation). Further seismic analysis, such as amplitude variation with offset (AVO), are typically applied for corroboration. But confirmation by drilling and sampling is still needed. The remainder of this section concerns identification of BSRs and application of velocity analysis with Amplitude Variation with Offset (Sloan, 1998, p. 484).

3.1.1 Identification of Bottom Simulating Reflectors

The origins of the concept for the bottom simulating reflector (BSR) has its beginnings in the opal A to opal CT transition that marks the transformation of unconsolidated sediments to a more consolidated form. Today, though, the use of term BSR is largely used for gas hydrate related occurrences. Examples of seismic data used in this study from the central Aleutian Basin (of the Bering Sea) show that both occurrences are present.

Bottom simulating reflectors (BSRs) first received recognition in the field as "BS reflectors" associated with the diagenetic boundaries seen in early marine seismic recordings (Meadows and Davies, 2010). Today, the term is commonly associated with recognition of strong reverse polarity reflections thought to represent the bottom boundary of the gas hydrate stability zone. However, three classes of bottom simulating reflectors are known in nature (Berndt et al, 2004). The first class is

defined to represent the base of the gas hydrate stability and is essentially a thermobaric surface. Conjecture and modeling strongly suggest in most instances the presence of a BSR is caused by the presence of free gas (Hyndman and Davis, 1992; Andreassen et al, 1990, 1995; Andreassen, 1995). Over the shallow depths below the ocean subbottom at which the marine gas hydrate BSRs are typically found, the stability field is more strongly a function of temperature than pressure and generally follow an isotherm. In stable heat flow environments, the isotherms generally follow the ocean subbottom and therefore the BSR may simulate the ocean subbottom (Hyndman and Davis, 1992).

The second class of BSRs originates in the diagenetic transition from opal-A to opal-CT. Interestingly, temperature is one of the dominant factors in silica formation; therefore, this diagenetic boundary may be an isothermal marker for a specific temperature at which the reaction may take place over an extensive area (Berndt et al, 2004). In general, BSRs, formed from diagenetic processes, are also pressure and temperature-dependent (Berndt et al, 2004).

Berndt et al (2004) also defines a third class of BSRs that have their origins in either a smectite illite conversion or a sudden increase in authigenic carbonates. It is not generally understood whether pressure, temperature, or other processes are important in formation of this class. Therefore, this third class is not of further concern here. Most of the remaining discussion is about gas hydrate related BSRs except as noted below.

Shipley et al (1979) first described the BSR as representing a boundary with a higher sonic velocity hydrate-bearing sediment above, and lower sonic velocity, free-gas bearing sediment below. Hyndman and Davis (1992) helped establish that BSRs mark the bottom of the hydrate stability zone in the shallow seafloor as inferred from

their observations. Three conditions were established that a suspected BSR has to meet: 1) the temperature and pressure conditions estimated at depth should be consistent with the maximum temperature and pressure at which hydrate is known to be stable; 2) the polarity should be reversed from the polarity of the ocean bottom reflection; and 3) interstitial and/or massive hydrates have been recovered at shallower depths. See summaries in Kvenvolden and Barnard (1983) and Suess et al (1988). Ninety (90) percent of the oceans' areal extent contains conditions thermodynamically stable to hosting gas hydrates (Sloan, 1998, p. 458); however, their presence is largely found at accretionary prisms and continental margins, and seldom in the deep ocean where a general source of terrestrial sediment material is lacking.

Knowing the general distribution and thickness of hydrate layers are important considerations to predict the influence of hydrates on future global climate change (Kvenvolden, 1988; MacDonald, 1990). In the absence of direct measurements, the presence of a BSR can be used to seismically estimate the geothermal heat flow (Yamano et al, 1982). Furthermore, marine gas hydrates are of interest because of their potential as a hazard during drilling operations.

Numerous seismic studies have focused on constraints on the quantity of hydrate in the sediments just above the BSR and on the methane concentration in the pore fluid below the BSR (e.g., Shipley et al, 1979; Shipley and Didyk, 1982; Minshull and White, 1989; Miller et al, 1991; Davis et al, 1990). The main results are:

1. The reflection polarity is usually reversed from that of the ocean bottom reflection, which indicates that, for a simple interface contrast, there must be a lower acoustic impedance below the boundary.

2. The BSR reflection coefficients are large, commonly 30% of that of the seafloor; thus quite high concentrations of hydrate must be present above the BSR, or there must be free gas below it.
3. The hydrate layer must be at least a few meters thick (an eighth to a quarter of a seismic wavelength) to give the observed strong multichannel seismic reflections at low frequencies, but not more than a few tens of meters in most areas because seismic velocity generally indicates little increase in average velocity in the sediment section from the BSR to the seafloor.
4. The impedance contrast at the base of the layer must be very abrupt since BSRs are sharp and clear at the high frequencies of small airgun systems (i.e., up to 100 Hz;).
5. The lack of a reflection from the top of the hydrate zone (it should be positive) indicates that the upper boundary is probably a diffuse or gradual transition.

3.1.2 Amplitude Variation with Offset (AVO)

Ostrander (1984) is the classic paper that uses Poisson's ratio as a direct hydrocarbon indicator from AVO analysis. The differences in elastic properties between gas hydrate, free gas, and liquid water are the physical basis for AVO analysis of the BSR (Andreassen et al, 1995, p. 12,664). Differences in elastic properties are quantified by Poisson's ratio. The change of this ratio at an interface directly affects the reflected P wave amplitude as a function of offset on pre-stack data, specifically CDP gathers.

Various papers describe the numerous corrections necessary to apply AVO analysis to common depth point (CDP) gathers. Many factors affect the recorded

amplitude as a function of offset; eleven factors are identified (Ostrander, 1984; Andreassen et al, 1995): 1) reflection coefficient; 2) the encasing sediment; 3) spherical spreading; 4) source and receiver array attenuation; 5) event tuning; 6) interface geometry (smooth versus complex boundary); 7) structure; 8) anisotropy; 9) noise; 10) residual normal moveout; 11) processing.

A detailed examination of the CDP gathers will help to judge the quality and significance of the 11 factors cited (Ostrander, 1984; Andreassen et al, 1995). It is difficult to isolate and remove many of the different causes that affect the AVO response (Andreassen et al, 1995, p. 12,665). AVO analysis requires relative amplitude balancing to be preserved along with a typical sequence of pre-stack processing. In example, to obtain true amplitude-versus-offset data for the BSR analysis, the most important corrections are air gun source and hydrophone receiver array attenuation (e.g., Ostrander, 1984). The modeling studies of Andreassen et al (1995) confirm the value and difficulty of AVO analysis. Their modeling study concludes the presence of gas hydrate or free gas can strongly affect the compressional wave velocity of clastic sediments (Andreassen et al, 1995, p. 12,663). For sediment with more than a few percent of free gas, Poisson's ratio is found to drop to between 0.1 and 0.2 (Ostrander, 1984). As a consequence, the reflection coefficients and seismic response are directly affected.

More directly, Minshull and White (1989) point out how the transition, from overlying sediments with or without hydrate to sediments containing free gas, results in a decrease in Poisson's ratio. This in turn results in an increase in reflection amplitudes with increasing incidence angle (or offset). Given this response variation with offset angle and the usefulness of the AVO technique for gas analysis, it seems likely that far offset seismic images would be useful pieces of the puzzle to consider

in reconnaissance. Hyndman and Spence (1992, p. 6,685) point out the important characteristics of the seismic responses from the BSR. These include 1) reverse polarity relative to the response of the seafloor, and 2) large reflection coefficients, up to 50% of the seafloor reflection, and 3) a single symmetrical pulse suggesting a simple sharp interface.

Hyndman and Davis (1992) propose that in most cases BSRs are generated from methane removed from expulsion of pore fluids upward through thick sedimentary sequences with the methane carried as a disseminated free gas. Therefore, the hydrate layer builds upward from the base of the stability zone. And, thus the zone should have a sharp base and a diffuse or gradational top. In their model for the Cascadia accretionary prism even a strong BSR will not significantly inhibit vertical fluid flux, with permeability maintained by tectonic processes and natural hydrofracturing.

Hyndman and Davis (1992, p. 7,028) carried out an AVO modeling study, by varying the velocity and Poisson's ratio structures to illustrate that free gas is not necessary to generate a BSR response. Their modeling also showed that what happens at far offset is more diagnostic; if the impedance contrasts originate from a gas layer, the amplitudes predicted at far offsets flatten. This is critical to the motivation of our study reported here.

The reflection coefficient of a BSR is a function of three parameters: compressional velocity Vp, shear velocity Vs, and the density structure. With the AVO behavior primarily dependent on the contrast in Poisson's ratio related to the Vp/Vs ratio, Hyndman and Spence (1992) use compressional velocity and Poisson's ratio as their model parameters. This should give negative reflection amplitudes that become substantially larger (and smaller Poisson's Ratio) with increasing source-

receiver offset. Hyndman and Spence (1992, p. 6,687), "… conclude that the BSR must result from hydrate replacing pore fluid."

3.2 PROBLEM STATEMENT

Velocity contrasts beneath the ocean floor mark a change in material density, such as would be obtained by hydrate-filled sediments overlying a gas. BSRs related to hydrates are normally taken as indicators of the hydrate base, marked by a sharp decrease in compressional velocity and a sharp increase in shear velocity (Ecker et al, 1996).

Traditional oil and gas applications of CDP stacking and AVO analysis generally consider only near to mid offsets. For the shallower targets usually associated with marine gas hydrates the angle offsets are much greater, and the traditional AVO analysis may be less appropriate. The question asked is this: If the response changes with offset angle, how is this change manifested in a single channel far offset seismic image? As proposed in this study, the response in the single channel far offset seismic image may be particularly unique and informative to the presence of a BSR and to the presence of gas.

3.3 ANALYSIS OF SEISMIC IMAGES

We provide an overview from preliminary analysis of the pre-stack multi-channel seismic (MCS) data. Throughout the 15 multi-channel seismic data sets, a high abundance of VAMP structures and chimneys are found beneath a generally recognized and regionally extensive bottom simulating reflector, reversed polarity, at a reasonable depth to be the bottom of a gas hydrate stability zone. At greater depth, and usually normal polarity, another bottom simulating reflector is suggested to be

present in the single channel near offset seismic images likely associated with the opal-A to opal-CT transition and consolidation.

We demonstrate that far offset seismic images may serve as a unique identifier for the thermobaric boundary identifying the base of the gas hydrate stability zone. It is well documented that bottom simulating reflectors (BSRs) are a reliable indicator for identifying the presence or absence of gas hydrates in the world's oceans. Though there are cases of misidentification of both the presence or absence of gas hydrates, seismic evidence for bottom simulating reflectors is an efficient and cost-effective method to explore for gas hydrate resources in the marine environment.

Here we present three sample cases to show the capability of these single-channel far offset seismic sections to identify bottom simulating reflectors that uniquely identify the bottom of the gas hydrate stability zone. The three sample cases discussed here include 1) flat-lying reflections, 2) cross-cutting reflections, and 3) a speculated thermal anomaly. We use the single-channel near offset seismic sections as our ground-truth.

3.3.1 Flat-Lying Reflections

MCS01 provides our example of flat-lying reflections in which a possible BSR and the stratigraphy run parallel with each other. This can make it difficult to definitively separate the presence of a BSR from an otherwise "bright spot" horizon. In Figure 1 (a) below, the CDP stacked migrated data is shown. Figure 1 (b) shows the single-channel near offset seismic image; similarly, Figure 1 (c) shows the far offset seismic image. One VAMP at shotpoint 1,520; all chimneys/plumes all seem to terminate at 5,500 ms.

Figure 1 (a). The CDP stacked migrated seismic data is displayed here for MCS01.

Figure 1 (b). In Figure 1 (b) we have the seismic section for MCS01 created from the near channel. The data shows approximately 20 chimneys, at least one (at shotpoint 1,520) we identify as a VAMP; classic example of pull-ups above and push-downs below. The so-called BSR-GH is most likely the high negative horizon at 5,500 ms. However, there are other likely candidates at 5,250 ms, 5,300 ms, 5,450 ms, or even 5,600 ms. The data also shows another potential BSR at 6,100 ms; we will designate this as BSR-DB as it is likely to represent the transition from opal A to opal CT diagenetic boundary.

Figure 1 (c): Figure 1 (c) provides another view, this time using the far offset channel. Here, though the times are delayed because of the much larger offset, the presence of the BSRs are much more clearly evident. The BSR-GH is at 7,700 ms; in this offset view is seems much more identifiable as being the BSR for the gas hydrate presence. The BSR-DB is at 8,050 ms; at this far offset the reflection response is much stronger than in the near-offset image, suggesting the critical angle may have been surpassed. Other features are also more evident including the VAMP and termination of the chimneys at the BSR-GH are much more evident. The push-downs from the BSR-GH is much more exaggerated down through the BSR-DB; the latter has normal polarity. Stratigraphy shallower than the BSR-GH is more subdued in character.

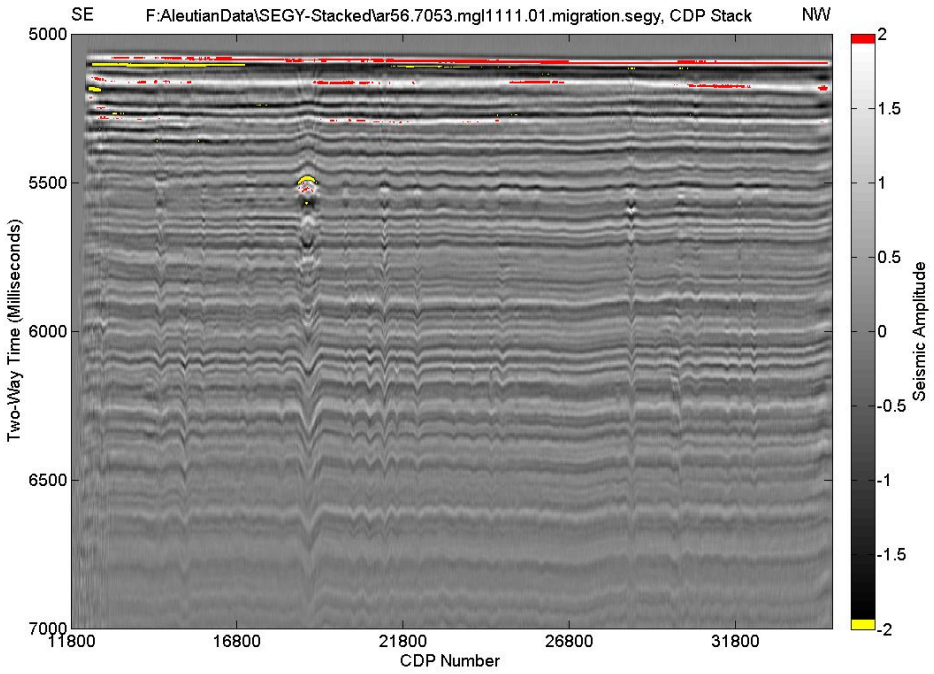
SE
F:AleutianData\SEGY-Stacked\ar56.7053.mgl1111.01.migration.segy, CDP Stack
NW
Two-Way Time (Milliseconds)
5000
5500
6000
6500
7000
11800
16800
21800
26800
31800
CDP Number
Seismic Amplitude
2
1.5
1
0.5
0
-0.5
-1
-1.5
-2

a)

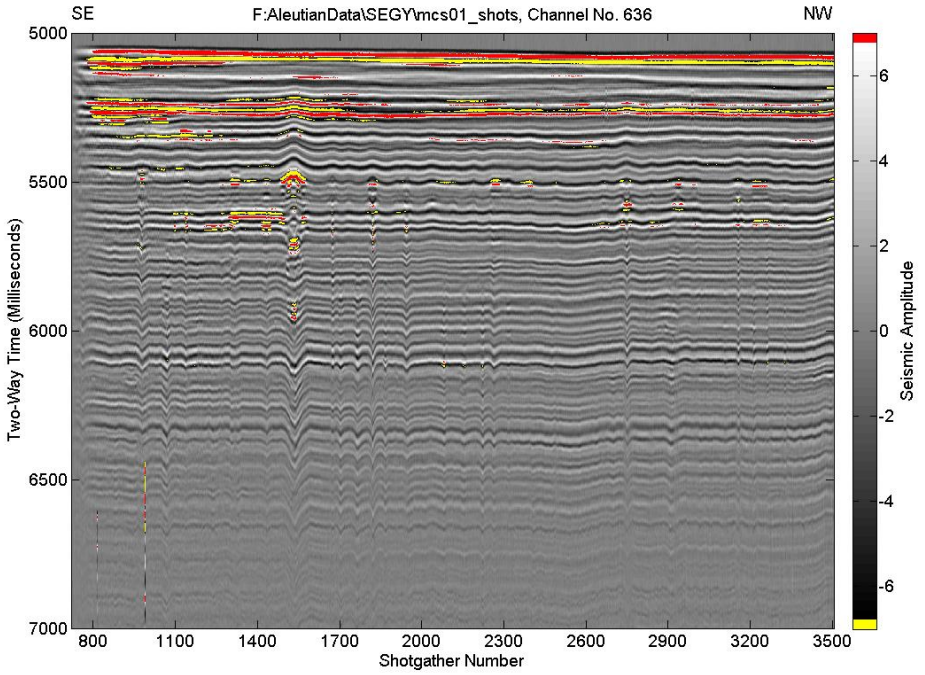
SE
F:AleutianData\SEGY\mcs01_shots, Channel No. 636
NW
Two-Way Time (Milliseconds)
5000
5500
6000
6500
7000
800
1100
1400
1700
2000
2300
2600
2900
3200
3500
Shotgather Number
Seismic Amplitude
6
4
2
0
-2
-4
-6

b)

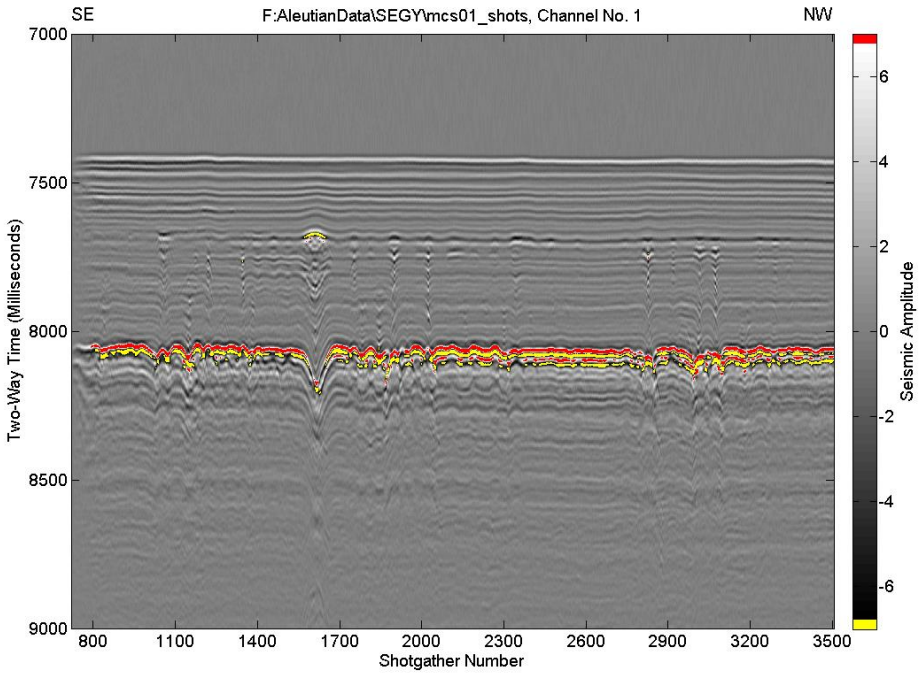

c)

Figure 1. Example of flat-reflections from MCS01: a) CDP stack migrated seismic image; b) single channel near offset seismic image; c) single channel far offset seismic image.

3.3.2 Cross-Cutting Reflections

MCS05 provides our example of cross-cutting beds in which a possible BSR cuts across the non-horizontal stratigraphy. This is one of the classic cases that makes it easy to identify the presence of a BSR. Figure 2 (a) shows the CDP stacked migrated data, Figure 2 (b) shows the single-channel near offset seismic section; similarly, Figure 2 (c) shows the single channel far offset image.

Figure 2 (a): The baseline CDP stacked migrated data for MCS05 is shown here.

Figure 2 (b). An example for a BSR-GH cross-cutting the geologic structure is shown in Figure 5 (b) for MCS05. The geologic structure slopes up from left to right whereas the identified BSR-GH at 5,600 ms largely mimics the seafloor without the ambiguity as seen in the flat lying beds example. Stratigraphy has a slight up dip

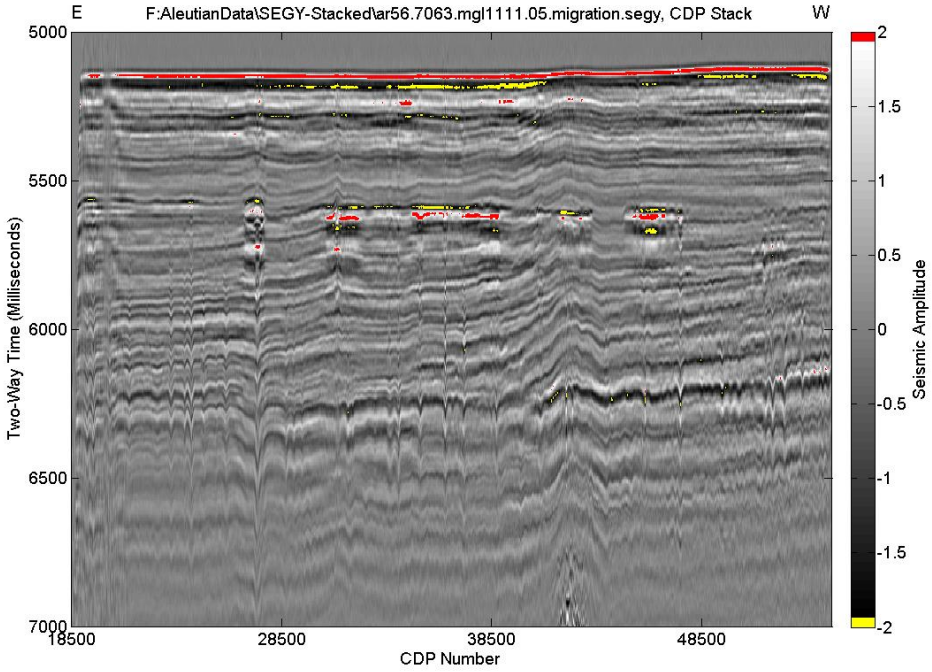
E
F:AleutianData\SEGY-Stacked\ar56.7063.mgl1111.05.migration.segy, CDP Stack
W
Two-Way Time (Milliseconds)
5000
5500
6000
6500
7000
18500
28500
38500
48500
CDP Number
Seismic Amplitude
2
1.5
1
0.5
0
-0.5
-1
-1.5
-2

a)

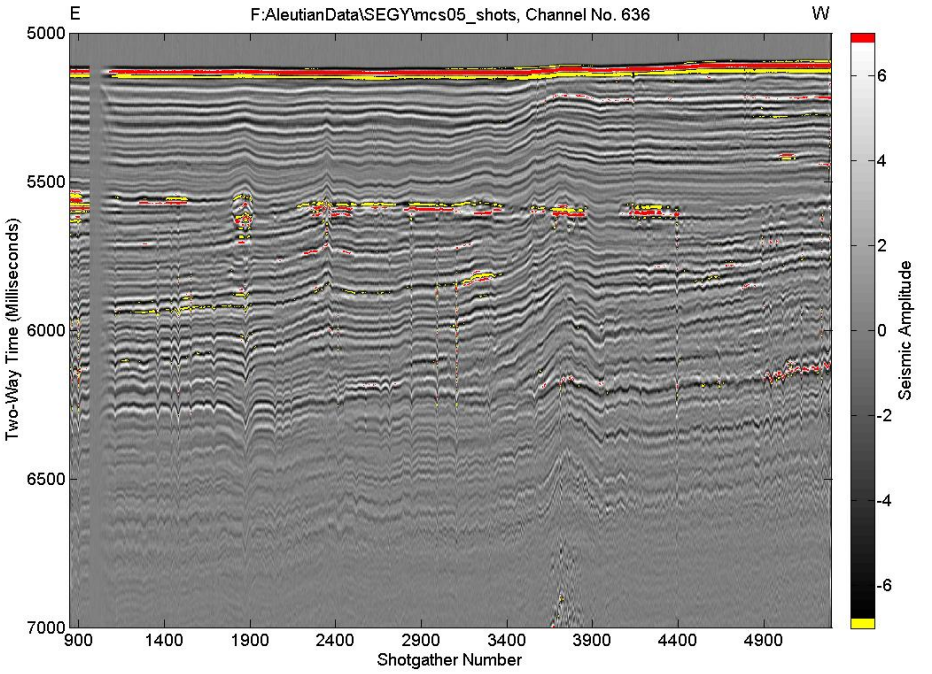
E
F:AleutianData\SEGY\mcs05_shots, Channel No. 636
W
Two-Way Time (Milliseconds)
5000
5500
6000
6500
7000
900
1400
1900
2400
2900
3400
3900
4400
4900
Shotgather Number
Seismic Amplitude
6
4
2
0
-2
-4
-6

b)

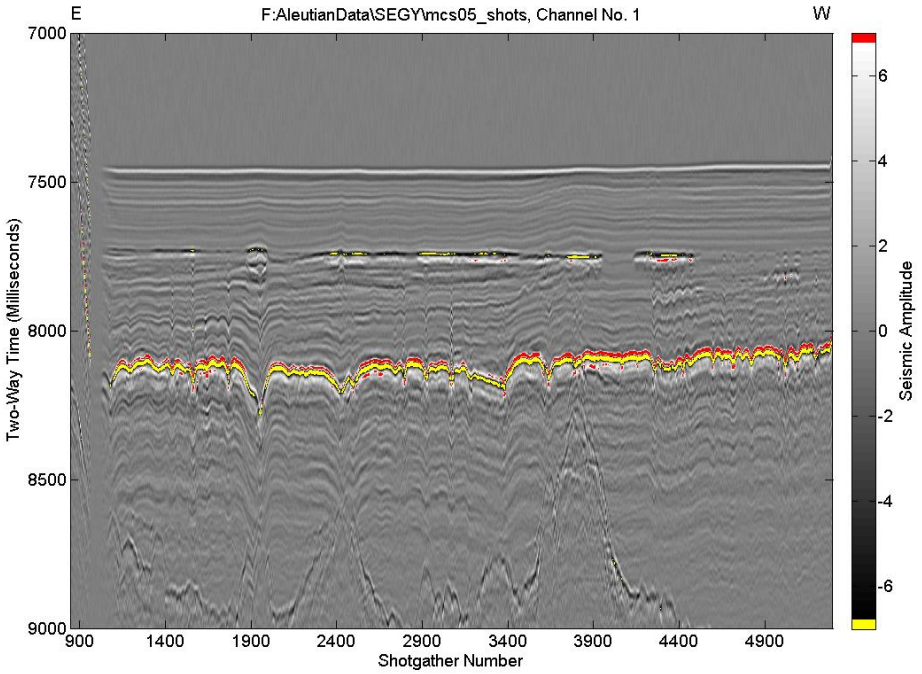

c)

Figure 2. Example of cross-cutting reflections from MCS05: a) CDP stacked migrated seismic image; b) single channel near offset seismic image; c) single channel far offset seismic image.

from left to right. Small VAMPs at shotpoints 1,900 and 2,400; maybe with a slight down dip from left to right. Roughly 17 chimneys/plumes; all below the suggested BSR-GH at 5,600 ms. Significant up bending at shotpoint 3,700 seems to have its origins in the acoustic basement. The BSR-DB is identified to be at 6,300 ms.

Figure 2 (c): The far offset display for MCS05 in Figure 4 (b) is dominated by the two BSRs. The BSR-GH at 7,750 ms is even more so, and the BSR-DB is at 8,150 ms. The BSR-DB at 8,150 ms, though it appears as a rough surface, it is likely very smooth but velocity variations in the layer above (and below the BSR-GH) disrupt the seismic continuity.

3.3.3 Inferred Thermal Anomaly

MCS13 provides an example from a possible thermal anomaly which normally are expected to disrupt and cause gaps in an otherwise expected regionally extensive BSR. These types of environments can make it particularly difficult to define or identify the base of the gas hydrate stability zone. Figure 3 (a) shows the CDP stacked migrated seismic image, Figure 3 (b) shows the single-channel near offset seismic image; similarly, Figure 3 (c) shows the single channel far offset seismic image.

Figure 3 (a). This is the baseline CDP stacked migrated seismic image processed in Christeson and Barth (2015)

Figure 3 (b): The three most notable features of this seismic image are the small VAMP at shotpoint 2,335, a larger VAMP at Shotpoint 2,582, and an intrusion of unknown nature from shotpoints 2,000 to 2,250 penetrating to the upper sedimentary layers. What is likely a BSR-GH, 5,550 ms (left); reverse polarity reflection where a BSR-GH would be expected seems to disappear as one looks closer to where the intrusion from the basement penetrates into the upper layers; 5,500 ms (right). The BSR-DB, 6,200 ms (left); seems to disappear across the basement; 6,250 ms (right).

Figure 3 (c): BSR-GH, 7,700 ms (left); can trace parts across basement; 7,700 ms (right). The BSR-GH is more easily seen in this far offset image at the larger VAMP and to the right. Between the smaller and larger VAMPs there is little trace of the BSR-GH. From the smaller VAMP and to the left over the region of the intrusion, a strong negative polarity feature is prominent. Inferring this strong reverse polarity feature is an extension of the BSR-GH, it is possible to ascertain how the thermal environment changes across the intrusion. BSR-DB, 8,100 ms (left); can trace high values across basement; 8,100 ms (right). As seen in previous examples, for BSR-DB seen at 8,100 m,

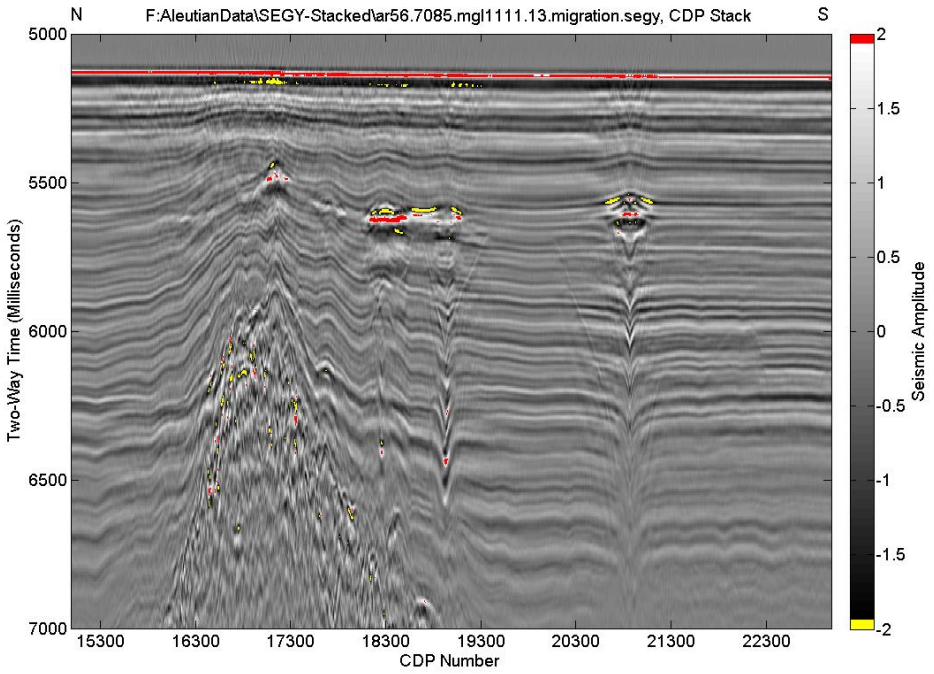
N
F:AleutianData\SEGY-Stacked\ar56.7085.mgl1111.13.migration.segy, CDP Stack
S
Two-Way Time (Milliseconds)
5000
5500
6000
6500
7000
15300
16300
17300
18300
19300
20300
21300
22300
CDP Number
Seismic Amplitude
2
1.5
1
0.5
0
-0.5
-1
-1.5
-2

a)

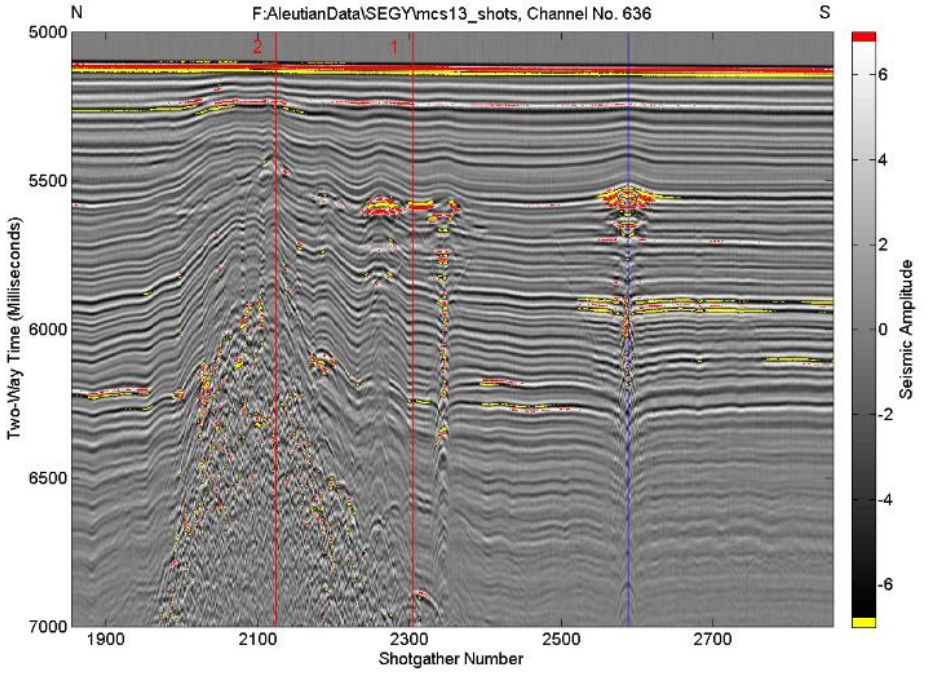
N
F:AleutianData\SEGY\mcs13_shots, Channel No. 636
S
2
1
Two-Way Time (Milliseconds)
5000
5500
6000
6500
7000
1900
2100
2300
2500
2700
Shotgather Number
Seismic Amplitude
6
4
2
0
-2
-4
-6

b)

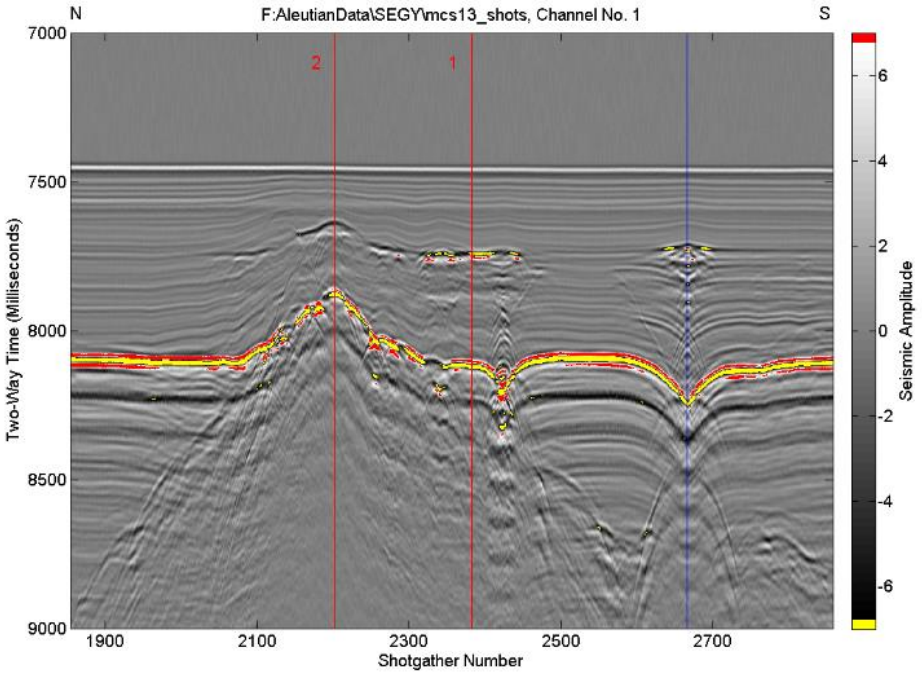

c)

Figure 3. Example of inferred thermal anomaly from MCS13: a) CDP stacked migrated seismic image; b) single channel near offset seismic image; c) single channel far offset seismic image.

the angle of incidence has passed the critical angle of reflection. Therefore, most of the energy is reflected back to the surface. The refraction patterns and velocity delays from the upper layers at the VAMPs in particular, breakup reflections of the BSR-DB boundary.

Based on observation of the seismic data that suggests a thermal anomaly in the subsurface, we use MCS13 as our third example. The near offset seismic image is shown in Figure 3 (b). Based on the plumes for shotgathers at 2,575 and 2,350, we have identified the BSR-GH to be at 5600 ms, but the presence of the BSR-GH is lost over the body centered at shotgather 2,100. The BSR-DB is at about 6,200 ms. The locations for the BSRs are much more evident in Figure 3 (c) using the far offset data. In this example

should the BSR-GH still be called a BSR? Even though this is not following the seafloor, most likely it originates in the geologic column because the temperature field is elevated, and therefore it is mimicking the seafloor for the temperature present at this location, even though on the larger scale the shape of the seafloor is not preserved, this is likely an extension of the BSR-GH due to higher heat flow originating in the intrusion.

Note there is a prominent horizon at 5,250 ms in the near offset image corresponding to the horizon noted at 7,600 ms in the far offset seismic image. We might speculate this is a hydrate deposit.

3.4 DISCUSSION

As seen in the previous sample cases considerable new information is obtained by reviewing the far offset seismic images. In AVO analysis it is possible to obtain quantitative information at specific locations chosen for analysis based on pre-stack CDP gathers subjected to various difficult to apply corrections such as true amplitude recovery and especially source and receiver array attenuation. The various assumptions that underlie AVO should apply everywhere free gas is present. By choosing a single channel offset display the assumptions for AVO across the CDP gather are not needed. Therefore, you can quickly evaluate large volumes of data looking for spatial anomalies within single channel images. The example of a flat-lying stratigraphy in Figure 1 (c), for the far offset, shows the areal extent of the BSR; it is not strong, but it is a clear barrier to further upward migration of gas.

The cross-cutting example of Figure 2 (a, b) is straight forward with little to no surprise when reviewing Figure 2 (c). However, a closer examination of the signature for

the BSR reveals a uniqueness not expected from the near offset display. The BSR abruptly stops and restarts.

Here the information content of individual traces from the potential thermal anomaly are examined in more detail. Figure 4 (a) shows individual traces from the near offset image shown in Figure 3 (b) at Red 1; five traces centered at Shotpoint 2300. The traces clearly show the ocean bottom arrival at 5,100 ms and the BSR-GH at 5,550 ms. The arrival from the BSR-DB is not clearly recognized but is probably the feature seen at 6,250 ms. Figure 4 (b) provides the traces from Figure 3 (b) at Red 2; five traces centered at Shotpoint 2120. As expected the ocean bottom arrival is easily recognized. If the thermal environment is uniform, it might be expected to find a cross-cutting BSR-GH showing an expression around 5,550 ms. If the intrusion centered at Shotpoint 2,120 is due to salt or other feature that disrupts the thermal environment, a trace excursion should be recognized at an earlier time, but none exists among the five traces.

The discussion above is reported for Figure 5 for traces extracted from the far offset image of Figure 3 (c). The result is different. In Figure 5 (a), feature Red 1 shows the ocean bottom arrival at 7,450 ms, BSR-GH at 7,750 ms, and BSR-DB at 8,150 ms. This is consistent with the results previously mentioned for the near offset except that the BSR-DB is clearly identifiable here. This provides hope that if the thermal environment is stable, the arrivals for feature Red 2 would appear at approximately the same times if present. The ocean bottom arrival is at 7,450 ms as expected. The other two events arrive earlier than expected; the BSR-GH at 7,650 ms; the BSR-DB at 7,850 ms. This offers a strong inference that Location Red 2 is warmer than Location Red 1 while

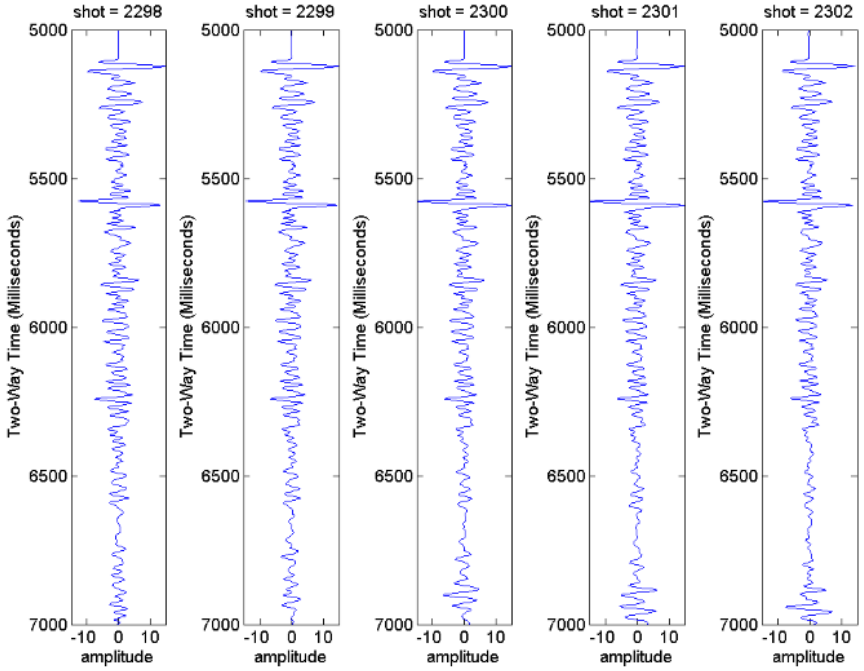

a)

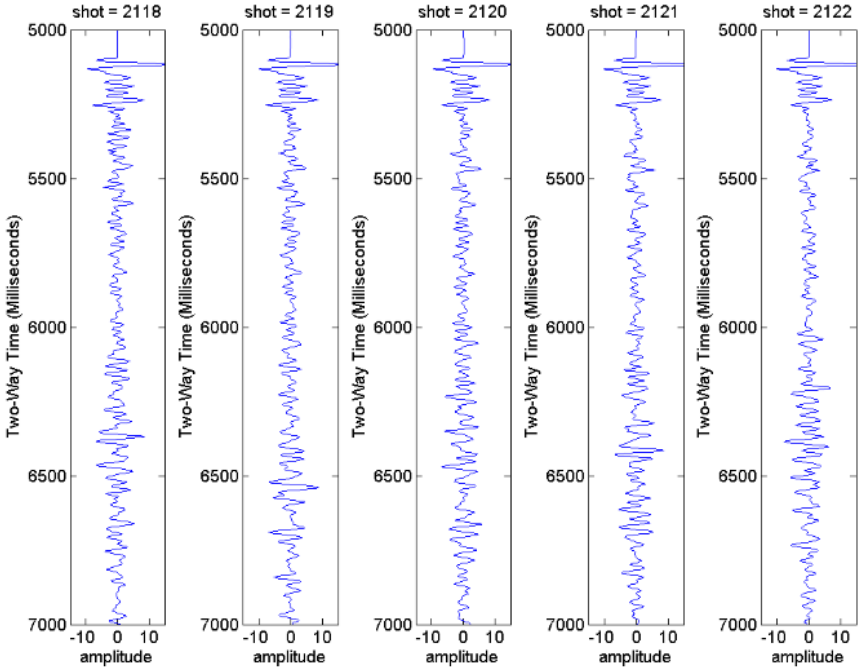

b)

Figure 4. Traces from near offset image of MCS13 as shown in Figure 3 (b): a) Location Red 1, and b) Location Red 2.

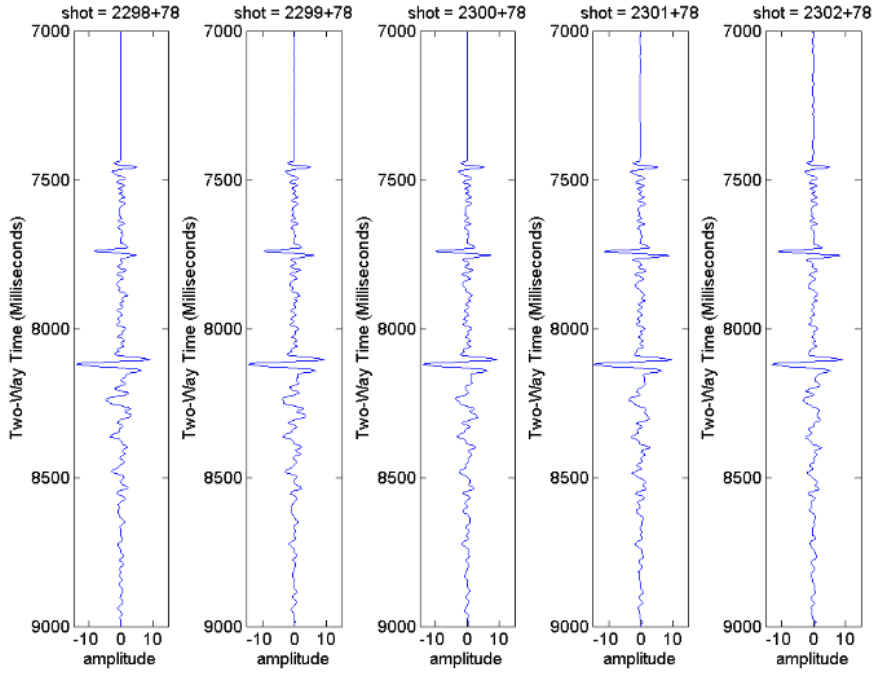

a)

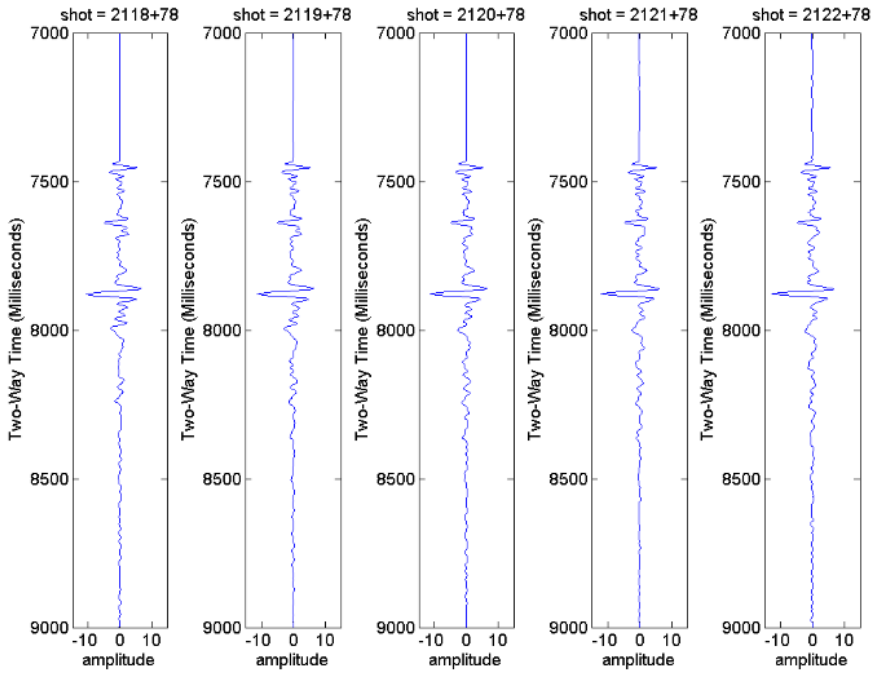

b)

Figure 5. Traces from far offset image of MCS13 as shown in Figure 3 (c): a) Location Red 1, and b) Location Red 2.

expanding the conditions under which presence of free gas may be identified from seismic data.

3.5 CONCLUSIONS

It is shown here that single channel images at far offset provide a useful enhancement to identify the presence of gas hydrate BSRs. Results indicate that BSRs related to marine gas hydrates present spatially coherent structures that may be uniquely identifiable from single channel far offset seismic images. Obviously less quantitative than AVO, but perhaps a stronger confirmation than AVO for the actual presence of free gas. This approach represents a qualitative, but powerful, technique based on principles from AVO and overcomes the obstacles of difficult-to-apply corrections in AVO analysis. The technique has proven useful to identify the presence of marine gas hydrates in the central Aleutian Basin which itself is a unique environment for the presence of marine gas hydrates. Therefore, this methodology should be applied with additional data sets in other areas such as the Gulf of Mexico, where it has proven difficult to identify regionally extensive BSRs even though marine gas hydrates have a significant presence in the Gulf area.

The far offset images provide a more compelling case to identify the presence of marine gas hydrates than identification from stacked images and even AVO analysis. The minimal signal processing and the geometric effects associated with far offset data complicate certain features within the images. But those effects impact the features associated with the presence of free gas very differently than all the other sediments. Amplitudes level off as offset is increased, and the BSR presents a uniquely identifiable negative reflection in the far offset seismic image. In contrast the diagenetic boundary, or

BSR-DB, generally a positive reflection, largely is accentuated in the far offset images because the critical angle of reflection has been reached.

As shown in the three example cases, the presence of the BSR is enhanced in the case for flat-lying structures (Figure 1). Even for the example case of cross-cutting structures (Figure 2) the BSR is greatly enhanced. In Figure 3 this approach expands detection to an example that may have a thermal anomaly that seemingly disrupts the presence of the thermobaric surface.

We outlined our ongoing research into simple approaches to analyze single channel seismic images at far offset to identify and confirm the presence of BSRs in multi-channel seismic acquisitions. Two directions are envisioned for future work. The first is to apply this approach to other areas, particularly, to the Gulf of Mexico where identification of regionally extensive BSRs have been difficult to identify. This is appropriate to assess whether this approach has broader application. The second direction is to derive quantitative information associated with the far offset data. Multi-channel seismic data sets contain huge amounts of information that is currently underutilized even in modern processing approaches. Future efforts should be made to apply a simple NMO on the far offset traces to address the shortening of the far offset traces (which distorts the frequency content) and adjust the images to better quantitatively compare to the near-offset images.

ACKNOWLEDGEMENTS

The MGL1111 data sets were made available to us though the courtesies of Dr. Ginger Barth, U.S. Geological Survey, and Dr. Warren Wood, Naval Research

Laboratory, and the download assistance of Rose Anne Weissel, Marine Geoscience Data System, LDEO, Columbia University.

REFERENCES

Andreassen K., 1995. Seismic Reflections Associated with Submarine Gas Hydrates. D.Sci. Thesis, U. Tromso, Norway.

Andreassen K., Hart P.E. and Grantz A., 1995. Seismic studies of a bottom simulating reflection related to gas hydrate beneath the continental margin of the Beaufort Sea. Journal of Geophysical Research 100, (B7), 12659-12673.

Andreassen K., Hogstad K. and Berteussen K.A., 1990. Gas hydrate in the southern Barents Sea, indicated by a shallow seismic anomaly. First Break 8, 235–245.

Atwater T.; 1970. Implications of plate tectonics for the Cenozoic tectonic evolution of western North America. Geological Society of America Bulletin. 81, 3513-3536.

Barth G. A., Scholl D. W. and Childs, J. R. 2006. Possible deep-water gas hydrate accumulations in the Bering Sea. Fire in the Ice, Methane Hydrate Newsletter 6, (3), 10-11.

Barth G., Childs J., and Wood, W., 2013. Multi-Channel Seismic Shot Data from the Bering Sea acquired during the R/V Marcus G. Langseth expedition MGL1111 (2011). Interdisciplinary Earth Data Alliance (IEDA). http://doi:10.1594/IEDA/318037.

Berndt C., Bunz S., Clayton T., Mienert J. and Saunders M., 2004. Seismic character of bottom simulating reflectors: examples from the mid-Norwegian margin. Marine and Petroleum Geology 21, 723-733.

Bishnoi P. R., Gupta A. K., Englezos P. and Kalogerakis N., 1989. Multiphase equilibrium flash calculations for systems containing gas hydrates. Fluid Phase Equilibria. 53, 97-104.

Byrne T. 1979. Late Paleocene demise of the Kula-Pacific spreading center. Geology 7, (7), 341-344.

Christeson G.L. and Barth G.A., 2015. Aleutian basin oceanic crust. Earth and Planetary Science Letters 426, 167-175

Cooper A.K., Marlow M.S. and Scholl D.W., 1977. The Bering Sea – A multifarious marginal basin. In: Island Arcs, Deep Sea Trenches and Back-Arc Basins, (ed. M. Talwani and W. C. Pitman), American Geophysical Union, pp. 437-450.

Cooper A.K., Marlow M.S. and Scholl D.W., 1987. Geologic framework of the Bering Sea crust (Chapter Five). Geology and Resource Potential of the Western North America and Adjacent Ocean basins – Beaufort Sea to Baja California, Circum.-Pacific Council for Energy and Mineral Resources, pp. 73-102.

Cooper A. K., Marlow M. S., Scholl D. W. and Stevenson, A. J., 1992. Evidence for Cenozoic crustal extension in the Bering Sea region. Tectonics 11, (4), 719-731.

Cooper A. K., Scholl D. W., Marlow M. S., Childs J. R., Redden G.D., Kvenvolden K.A. and Stevenson A.J. 1979. Hydrocarbon potential of Aleutian Basin, Bering Sea. American Association of Petroleum Geologists Bulletin 63 (11), 2070-2087.

Creager J.S., Scholl D.W. and Supko P.R., eds., 1973. Initial reports of the Deep Sea Drilling Project, Vol. 19. U.S. Government Printing Office, 913 p.

Davis E. E., Hyndman, R. D. and Villinger, H., 1990. Rates of fluid expulsion across the Northern Cascadia accretionary prism: Constraints from new heat flow and multichannel seismic reflection data. Journal of Geophysical Research 95 (B6), 8869-8889.

Ecker C. D., Lumlet, D., Dvorkin, J. and Nur A., 1996. Structure of hydrated sediments from seismic and rock physics. Proceedings of the Second International Conference on Natural Gas Hydrates, Toulouse, 491-498.

Engebretson D.C., Cox, A. and Gordon, R. G., 1984. Relative Motions Between Oceanic Plates of the Pacific Basin. Journal of Geophysical Research 89, (B12), 10291-10310.

Foster T. D., 1962. Heat-flow measurements in the Northeast Pacific and in the Bering Sea. Journal of Geophysical Research 67, (7), 2991-2993.

Hein J. R., Scholl D. W., Barron J. A., Jones M. G. and Miller J., 1978. Diagenesis of Late Cenozoic diatomaceous deposits and formation of the bottom simulating reflector in the southern Bering Sea. Sedimentology 25, (2), 155-181.

Hyndman R.D. and Davis E.E.; 1992. A mechanism for the formation of methane hydrate and seafloor bottom-simulating reflectors by vertical fluid expulsion. Journal of Geophysical Research 97, (B5), 7025-7041.

Hyndman R. D., and Spence G. D., 1992. A seismic study of methane hydrate marine bottom simulating reflectors. Journal of Geophysical Research, 97 (B5), 6,683.

Karl H. A., Carlson P. R. and Gardner J. V., 1996. Aleutian Basin of the Bering Sea. In: Geology of the United States Seafloor: The View from Gloria. (ed. J. V. Gardner, M. E. Field and D. C. Twichell), Cambridge University Press, 374 pp.

Kvenvolden, K. A., 1988. Methane hydrate – a major reservoir of carbon in the shallow geosphere? Chemical Geology 71, 41-51.

Kvenvolden, K. A. and Barnard, L. A., 1983. Hydrates of natural gas in continental margins. Studies in Continental Margin Geology 34, 631-640.

Kvenvolden, K. A. and Lorenson, T. D., 2000. Methane and other hydrocarbon gases in sediment from the southeastern North American continental margin. In: Paull, C.K., Matsumoto, R., Wallace, P.J., and Dillon, W.P. (Eds.), 2000 Proceedings of the Ocean Drilling Program, Scientific Results, Vol. 164, 29-36.

Lee H. J. 1973. Measurements and estimates of engineering and other physical properties, Leg 19. Initial Reports of the Deep Sea Drilling Project, Vol. 19. U. S. Government Printing Office, pp. 701-719.

Lu Z. and Sultan N., 2008. Empirical expressions for gas hydrate stability law, its volume fraction and mass-density at temperatures 273.15K to 290.15 K. Geochemical J. 42, (2), 163-175.

MacDonald, G. J., 1990. Role of methane clathrates in past and future climates. Climate Change 16, 247-281.

Meadows D. and Davies R.D., 2010. The limited suitability of silica diagenetic boundaries as isothermal markers: Insights from seismic reflection imaging, Offshore Sakhalin, Russian Far East. Marine and Petroleum Geology, 27, 1028-1029.

Miller J. J., Lee M. W. and von Huene R., 1991. An analysis of a seismic reflection from the base of a gas hydrate zone, offshore Peru. AAPG Bulletin 75 (5), 910-924.

Minshull T. and White R., 1989. Sediment compaction and fluid migration in the Makran accretionary prism. Journal of Geophysical Research 94 (B6), 7387-7402.

Ng D. and Martinson D., 2011. RV Langseth Data Reduction Summary, MGL1111, Dutch Harbor, AK – Dutch Harbor, AK, Not Final, V1.2, 2011-09-02. Lamont Doherty Earth Observatory, Columbia University, 64 pp, +5 Appendices.

Ostrander W. J. 1984. Plane-wave reflection coefficients for gas sands at nonnormal angles of incidence. Geophysics 49 (10), 1637-1648.

Rea D.K. and Dixon J.M. 1983. Late Cretaceous and Paleogene tectonic evolution of the North Pacific Ocean. Earth and Planetary Science Letters 65, (1), 145-166.

Rearic D.M., Williams S.R., Carson P.R. and Hall R.K. 1988. Acoustic evidence for gas-charged sediment in the abyssal Aleutian Basin, Bering Sea, Alaska. Department of the Interior, U. S. Geological Survey, Open-File Report 88-577.

Scholl D.W., Barth G.A. and Childs J.R., 2009. Why hydrate-linked velocity-anomaly structures are common in the Bering Sea Basin: A hypothesis. In: Natural Gas Hydrates – Energy Resource Potential and Associated Geologic Hazards, American Association of Petroleum Geologists Memoir, Vol. 89 (ed. T. Collett, A. Johnson, C. Knapp and R. Boswell), pp. 308-323.

Scholl D.W., Buffington E.C. and Hopkins D.M., 1968. Geologic history of the continental margin of North America in the Bering Sea. Marine Geology 6, 297-330.

Scholl D.W. and Cooper A.K., 1978. VAMPs – Possible hydrocarbon-bearing structures in Bering Sea basin. American Association of Petroleum Geologists Bulletin 62, (12), 2481-2488.

Scholl D.W. and Creager J.S., 1973. Geologic synthesis of Leg 19 (DSDP); Far North Pacific, and Aleutian Ridge, and Bering Sea. Initial Reports of the Deep Sea Drilling Project, Vol. 19. U. S. Government Printing Office, pp. 897-913.

Scholl D.W. and Hart P.E., 1993. Velocity and amplitude structures on seismic-reflection profiles – Possible massive gas-hydrate deposits und underlying gas accumulations in the Bering Sea Basin. In: The Future of Energy Gases, Professional Paper 1570 (ed. D. G. Howell), pp. 331-351, U. S. Geological Survey.

Scholl D.W. and Stevenson A.J, 1990. Was the Aleutian Basin more enclosed, its deeps oxygen deficient, and the geothermal gradient steepened in the Middle Tertiary? Implications for the petroleum potential of the Bering Sea (abs). Fifth Circum-Pacific Energy and Mineral Resources Conference, Honolulu, HI, 29 July-3 August 1990, p. 1000.

Shipley T. H., Houston M. H., Buffler R. T., Shaub F. J., McMillen K. J., Ladd J. W. and Worzel J. L., 1979. Seismic evidence for widespread possible gas hydrate horizons on continental slopes and rises. AAPG Bulletin 63 (12), 2204-2213.

Shipley T. H. and Didyk B. M., 1982. Occurrence of methane hydrates offshore southern Mexico. In: Watkins J.S., Casey Moore J. et al. (Eds.) 1982, Initial Reports of the Deep Sea Drilling Project Vol. 66, 547-555.

Shor G.G. 1964. Structure of the Bering Sea and the Aleutian Ridge. Marine Geology 1, 213-219.

Sliter R., Barth G., Wood W. T. and Childs, J., 2011. Processed multi-channel seismic data in the Bering Sea acquired during R/V Marcus G. Langseth expedition MGL1111 (2011).

Academic Seismic Portal at UTIG, Marine Geoscience Data System. http://dx.doi.org/10.1594/IEDA/500056

Sloan Jr. E. D., 1998. Clathrate Hydrates of Natural Gases, Second. Marcel Dekker.

Spence G.D., Haacke R.R. and Hyndman R.D. 2010. Seismic indicators of natural gas hydrate and underlying free gas. In: Geophysical Characterization of Gas Hydrates, SEG Special Volume (ed. M. Riedel, E.C. Willoughby and S. Chopra), Chapter 4, pp. 39-71.

Suess E., et al 1988. Proceedings of the Ocean Drilling Program: Initial Reports, Vol. 112

Sultan N, Foucher J. P., Cochonat P., Tonnerre T., Bourillet J. F., Ondreas H., Cauquil E. and Grauls D., 2004. Dynamics of gas hydrate: case of the Congo continental slope. Marine Geology, 206, 1-18.

Wallace W.K. and Engebretson D.C., 1984. Relationships between plate motions and Late Cretaceous to Paleogene magmatism in southwestern Alaska. Tectonics 3, (2), 295-315.

Watanabe T., Langseth M.G. and Anderson R.N., 1977. Heat flow in back-arc basins of the western Pacific. In: Island Arcs, Deep Sea Trenches and Back-Arc Basins (ed. M Talwani and W. C. Pitman), American Geophysical Union, pp. 137-161.

Yamano M., Uyeda S., Aoki Y. and Shipley T. H., 1982. Estimates of heat flow derived from gas hydrates. Geology 10, 339-343

Yankovsky E. A., Terry D. A. and Knapp C. A., 2015. Seismic and gravity evidence for methane-hydrate systems in the central Aleutian Basin. International Journal of Earth Science and Geophysics 1 (1), 1-8.

CHAPTER IV

STABILITY ANALYSIS OF VAMP-HYDRATE SYSTEMS IN THE CENTRAL ALEUTIAN BASIN

Terry, Darrell A.; Knapp, Camelia C.; 2019. Stability Analysis of VAMP-Hydrate Systems in the Central Aleutian Basin. Manuscript, 39 p., 11 Figures, 2 Tables.

ABSTRACT

Marine gas hydrates have been studied intensely for more than five decades under the assumption that deep ocean basins lack the methane necessary to generate significant volumes of gas hydrates. Contrary to this, the deep waters of the Aleutian Basin in the Bering Sea alone are estimated to contain globally significant volumes of methane in gaseous and hydrate forms and are observed in seismic velocity amplitude (VAMP) structures. We investigate the hypothesis that the VAMP structures are a natural analog of the Bénard problem (and buoyancy-driven cellular convection) for a saturated porous medium, better known as the Lapwood problem. The Aleutian Basin's tectonic history may provide a unique environment leading to the formation of these methane hydrate structures in deep basins. Unraveling the physics and chemistry of forming methane hydrate structures in the Aleutian Basin may lead to a better understanding of the

potential for other deep water methane hydrate structures, and may lead to a re-evaluation of buoyancy driven flow in more traditional marine gas hydrate reserves.

The sections of this paper include the motivation for this research, the theory of cellular convection in a porous media. The motivation for this research is provided through a description of the tectonics of the Bering Sea Basin and of the seismic evidence for methane hydrate structures. The second section provides a review of the Lapwood problem describing the nature and conditions of cellular convection in a porous media. In a third section we conduct a stability analysis with calculations for the Rayleigh-Darcy number for the conditions found in the central Aleutian Basin. The research is a system level analysis of geophysical transport processes involved in the VAMP structures of the deep waters of the Aleutian Basin. From this we may gain a broader understanding of the role buoyancy driven flow may contribute in all marine gas hydrate systems.

Studies of marine gas hydrates began with the early accumulations of Rempel and Buffett (1997, 1998). Recent dynamic models such as Liu and Flemings (2007) provide are an important step. We are not aware of any other study that dynamically models VAMP structure and buoyancy. As a first step in this research we calculate the Rayleigh numbers for porous media flow to establish stability conditions in the central Aleutian Basin.

KEYWORDS: gas hydrates, cellular convection, stability analysis, Aleutian Basin

4.1 INTRODUCTION

Naturally occurring methane-hydrates have been the subject of study and interest since their prediction and discovery in the late 1960s. Over many decades it has been observed that marine gas hydrates are found in the shallow sediments in the deep ocean along continental margins, usually the upper reaches of the continental slopes. Though conditions exist for the formation of hydrates in the deep ocean basins, significant amounts of marine gas hydrates have not been expected to be found in deep ocean basins due to a general lack of methane availability. Contrary to this assertion are the velocity-amplitude anomaly (VAMP) structures found in the deep waters of the Bering Sea, and in particular, in the Aleutian and Bowers Basins at water depths greater than 3700 m (Scholl and Cooper, 1978; Rearic et al, 1988; Barth et al, 2006; 2009; Scholl et al, 2009).

Exploration in the Aleutian Basin began with the review of U.S. naval data in the 1960s and has progressed through several active campaigns of single and multi-channel seismic data collections, site observations during the Ocean Drilling Program, and GLORIA sonar surveys of the ocean floor physiography and backscatter (Karl et al, 1996). More recently, a new set of multi-channel seismic lines were collected as part of the U. S. participation in the Extended Continental Shelf Project (reference data report; Scholl et al, 2012; Christeson and Barth, 2015)

Evidence of the large and anomalous sub-bottom VAMP structures, abundance of the structures, and presence of bottom-simulating reflectors (BSR), suggest methane resources in globally significant quantities just within the central Aleutian Basin (Barth et al, 2009; Scholl, 2009). Furthermore, long available measurements of heat flow show anomalous moderately high values throughout the Aleutian Basin and other basins of the

Bering Sea (Foster, 1962; Watanabe et al, 1977; Cooper et al, 1987). Though the methane-hydrate structures of the Aleutian Basin are atypical from the traditional model of marine gas hydrates, the Aleutian Basin provides a unique opportunity to investigate the role of buoyancy-driven flow in the formation and distribution of marine gas hydrates. In this research we investigate buoyancy-stability calculations in the shallow sediments of a deep ocean basin to develop an understanding of the conditions and dynamics of the VAMP structures in the central Aleutian Basin.

1. Globally significant amount of gas hydrate speculated to be present in the central Aleutian Basin
2. VAMPs are typically 5 to 10 km in diameter
3. Thicknesses of hydrate layers varies
4. More than 12,000 VAMPs identified in the central Aleutian Basin

4.2 EVALUATION OF SEISMIC VAMP STRUCTURES

The new seismic data acquired in 2011 is examined with 3 different approaches. In this subsection we provide a review of a preliminary look of the CDP processing from Scholl et al (2012); then provide a look at some of the more fully processed CDP sections, and also show that far offset single channel seismic sections provide further interpretative capabilities for identifying bottom simulating reflectors. We use some of the processed results first presented in Scholl et al (2012). Then we provide an overview from preliminary analysis of the pre-stack multi-channel seismic (MCS) data using single channel displays of the near and far offsets. We have found, in particular, that far offset displays are useful for more clearly identifying the presence of a regional bottom simulating reflector (Terry and Knapp, 2019). Results from the data have previously

been presented in Scholl et al (2012), Christeson and Barth (2015), and Yankovsky et al (2016).

Cyrano. Results from minimal CDP)3-trace stack with NMO applied)processing of the VAMP named Cyrano, first presented in Scholl et al (2012), are shown in Figures 1 and 2. In Figure 1 (a) we see the behavior of pull-ups and push downs seen in the early literature; here the data has been migrated and depth converted. Figure 1 (b) shows results from the velocity analysis. Figure 2 shows an expanded section or image along the seismic line. Here we more clearly see the flat laying structure and a repetitive pattern of low velocity regions. A 1D acoustic velocity inversion (Wood, 1993) was used to obtain detailed estimates of velocity and other properties (Scholl et al, 2012).

4.2.2 CDP Stacked Seismic Data Analysis (Christeson and Barth, 2015).

A more complete CDP processing of the MGL1111 data is reported in Christeson and Barth (2015) and Sliter et al (2011). Shown here are lines MCS01, the Cyrano VAMP shown earlier, Figure 3 (a) and MCS05, Figure 3 (b). The CDP stacked SEGY data files are courtesy of the data portal at UT, Austin.

Figure 3 (a). MCS01 includes the Cyrano VAMP processed earlier in Scholl et al (2012) and shows numerous chimneys that terminate at just greater than 5500 microseconds; likely the bottom of the gas hydrate stability zone. Though not mathematically periodic, there is a regular pattern of chimneys.

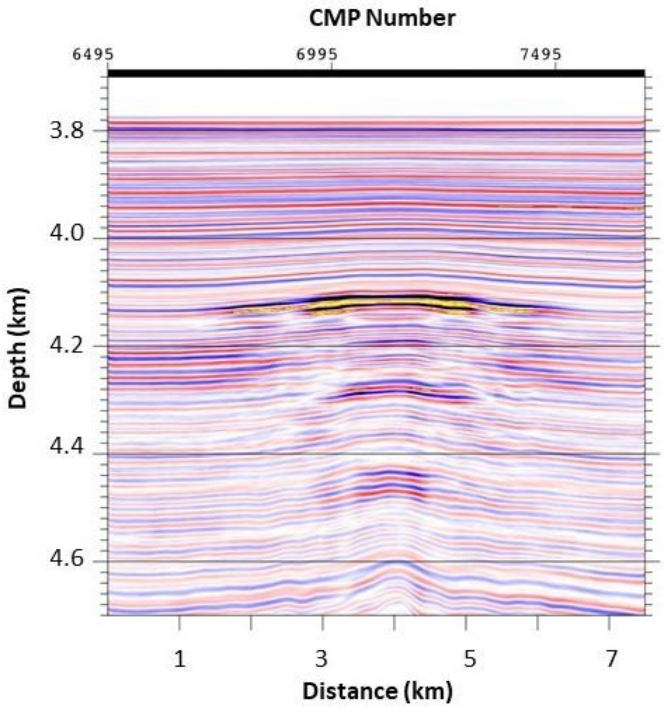

a)

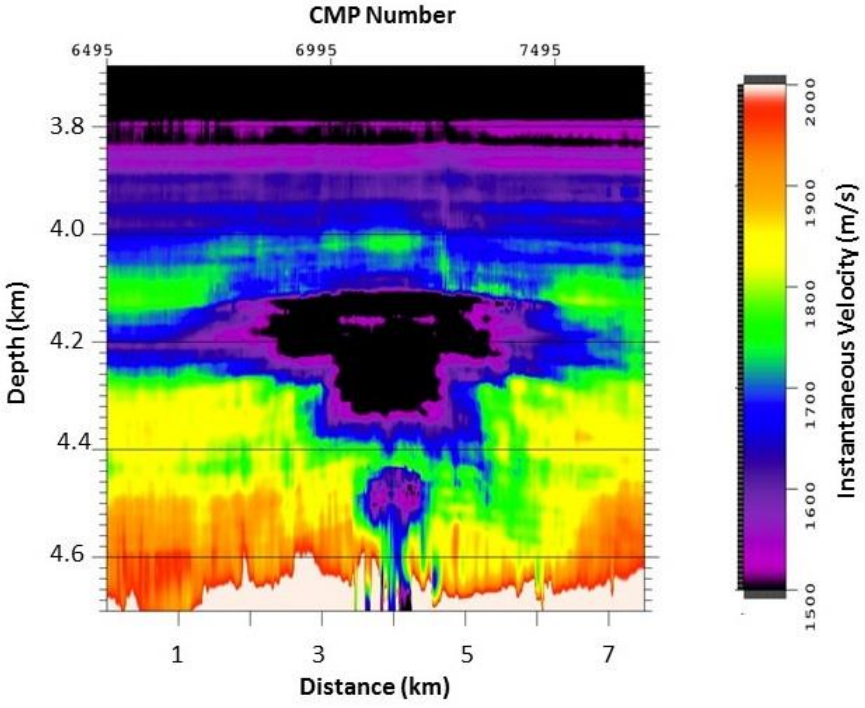

b)

Figure 1. Processed seismic results from Scholl et al (2012) for MCS01 at Cyrano. Part a) near channel CDP stack, migrated and depth converted. Part b) interval velocities for the same section after high resolution velocity analysis with GDMI.

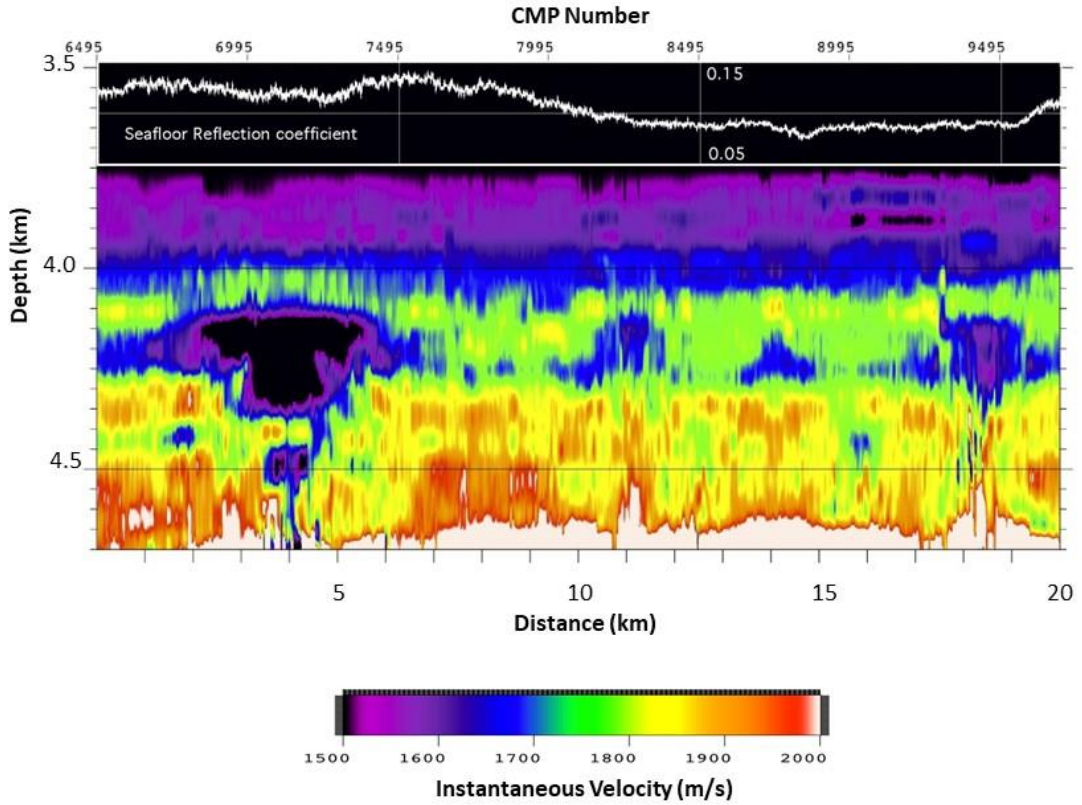

Figure 2. Processed seismic results from Scholl et al (2012) for MCS01 at Cyrano and nearby. Expanded area of velocity analysis shows multiple VAMP structures.

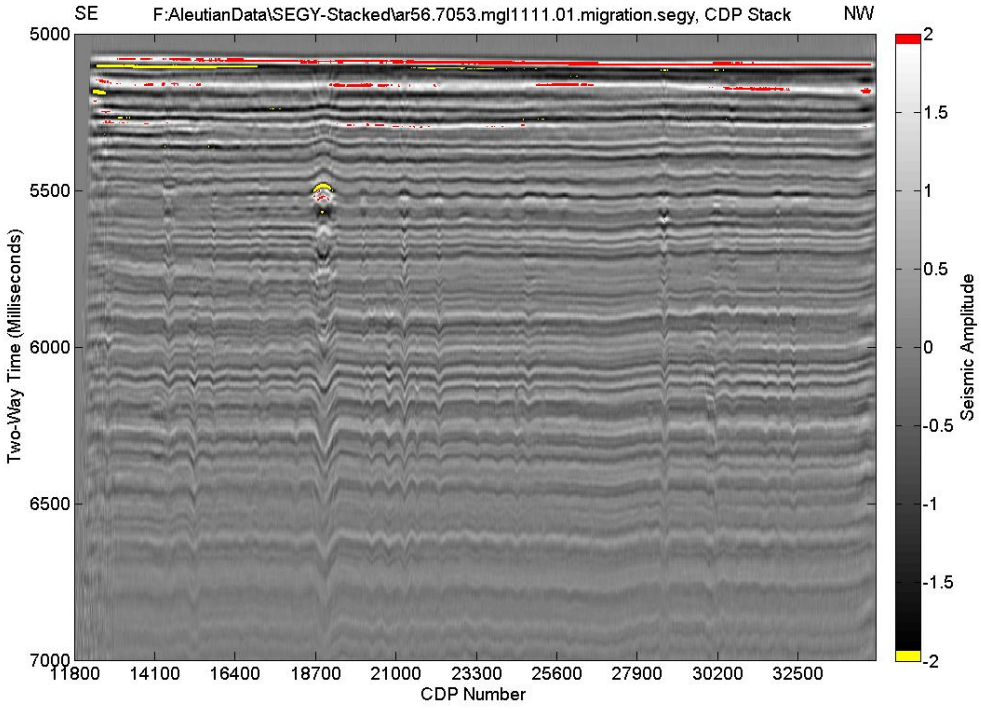

a)

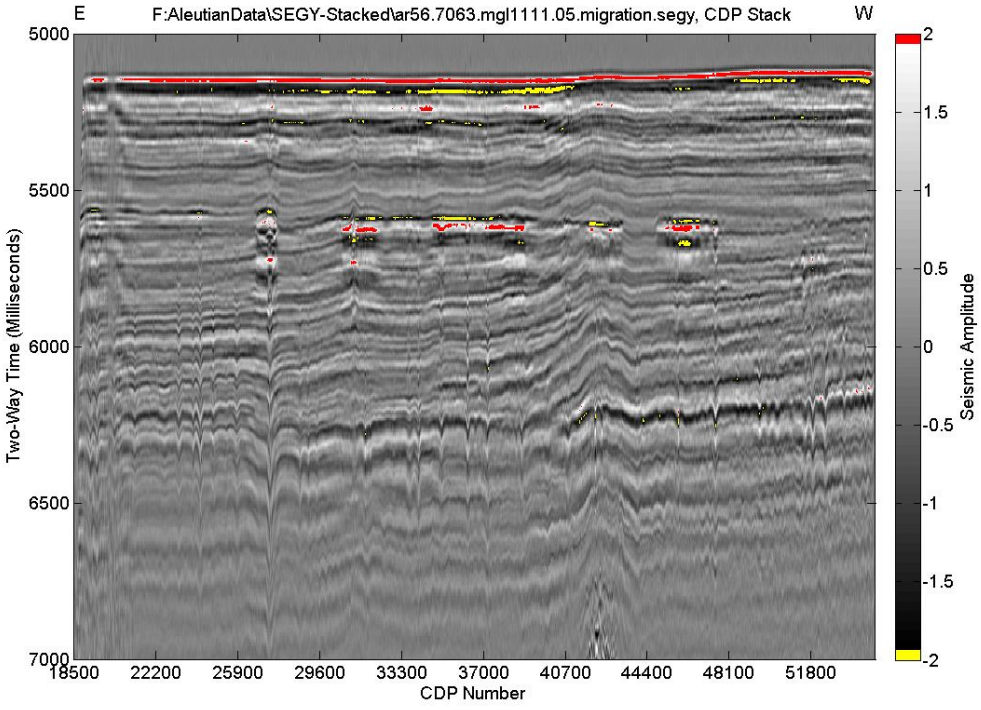

b)

Figure 3. CDP data for (a) MCS01, and (b) MCS05.

Figure 3 (b). MCS05 more clearly shows a BSR crosscutting the dipping horizons of this area. The regular pattern of chimneys is close to a spacing of 3000 CDPs. The dark band at 6300 ms is identified as the BSR-DB

4.2.3 Single-Channel Near and Far Offset Analysis (Pre-Stack Analysis of Seismic Data)

Multi-channel seismic data acquisition has proven to be a good tool for reconnaissance to detect the presence of methane hydrate. Seismic Common Depth-Point (CDP) processing has been extensively developed over more than six decades, and with current 3D acquisition systems is integrated across exploration and production environments. Seismic CDP processing led many of the developments in multi-channel signal processing yet is falling behind the state-of-the-art and does not take full advantage of the information content. In response AVO inversion has developed as a more general methodology for AVO analysis; AVO inversion requires less human interpretation and provides estimates of elastic properties. Amplitude Variation with Offset (AVO) analysis has been a common approach to confirming the presence of bottom simulating reflectors.

Here we consider the prestack single channel near and far offset images as an alternative to AVO analysis. The objective of using the single channel images rather than CDP stack images is easier visualization of when a BSR-GH is present. We provide comment on features in three lines (MCS01, MCS05, MCS09A, and MCS13) to represent the types of features of interest found in the data, Figures 7 thru 10 respectively. We generated single channel seismic sections for the nearest and farthest offset channels. For display we applied a wide bandpass filter to remove cable noise for displays of both the single channel seismic sections and the shot gathers. In all displays of the seismic

data below we use a linear gray scale clipped at ± 7. We chose this value to provide the greatest definition of the laying. Negative and positive clippings are displayed with yellow and red, respectively. This choice for the clipping value has been very fortuitous to define major horizontal layer boundaries. In each we display a 2,000 ms window starting just above the water bottom. We start the window at 5,000 ms for the near offsets, and start the window at 7,000 ms to account for the longer travel time due to the far offsets without a normal moveout (NMO) velocity correction.

To better understand the link between the near and far offset displays we next present displays of a shot gather along with the near and far offset data from MCS01 in Figure 4. In this example it is possible to follow the variation of reflection strength with offset distance. It seems evident that the diagenetic boundary is visualized by the clipping because the critical angle of reflection is reached. It is just as evident that more complex circumstances govern visualization of BSR-GH, the plume-like structures, chimneys, other features, and possible the spacing of VAMPs and chimneys.

In Figure 5 we show single channel seismic sections for the near and far offset channels for MCS05. The subplot for the near offset marks part of the time horizon just below 5500ms in red and yellow. We believe this is in fact a portion of a more extensive or regional BSR-GH discussed in Scholl et al (2009). This is interpreted to mark the bottom of the gas hydrate stability zone. In the lower (far offset) display we believe the clipping identifies the diagenetic boundary discussed in Scholl et al (2009); i.e. BSR-CT. From the display of this figure we are able to define a relatively homogeneous horizontal layer between the bottom of the gas hydrate stability zone and the diagenetic boundary. In the near offset the diagenetic boundary should be at about 6,000 ms.

First the sedimentary structures have a little more dip, and enough such dip to better define a possible regionally extensive BSR-GH. With or without the negative and positive clipping a strong reflector clearly cuts across the mildly dipping structures, providing a strong indication of a BSR-GH. The near offset display also shows a suggestion of semi-regular plumes across the section. The far offset display of Figure 6 shows the diagenetic boundary with the negative and positive clipping. This far offset display of Figure 6 also shows the presence of the regionally extensive BSR-GH. Even without clipping, the presence of a reflector crossing the dipping sedimentary layering is evident. The semi-regular plumes evident in the near-offset section are even more evident in the far offset section.

Two features of interest are identified in the near offset display from MCS09A in Figure 6. These include the well-defined plume-like structure centered near SP 1365 at about 5550 ms, and the thick bright spot, also near 5550 ms, spanning SPs 1600 to 2000. Again, the far offset display seemingly identifies the diagenetic boundary. In addition, the far offset display highlights the presence of plumes identified in the near offset display.

MCS13 provides another example of a plume-like structure in the near and far offset displays of Figure 7. The far offset display again seemingly identifies the diagenetic boundary (BSR-DB) and highlights the semi-regular presence of plumes seen in the near offset display These four examples show the likely presence of a regional BSR-GH and the diagenetic boundary to define a relatively homogeneous horizontal layer. This geometry may provide a good environment in which to study the role of buoyancy and its role in formation and evolution of thermogenic methane hydrates.

The objective in this research is to determine whether suitable conditions exist that cellular convection may occur; seismic evidence suggests the semi-regular ordering of plumes and chimneys. By our observation, we have the following distributions of plumes and chimneys:

MCS05 – spacing on left side is approximately 500 shotpoints, or 25,000 m. middle of image chimney spacing is closer to 150 m, or 7,500 m.

MCS09a – spacing is approximately 250 shotpoints, or 12,500 m

MCS13 – spacing of plumes is approximately 275 shot points, or 13,750 m.

Among other requirements, for cellular convection to occur or develop, it is necessary that the Rayleigh-Darcy Number, the ratio of buoyancy forces to viscous forces, exceeds a critical value. These calculations are detailed below.

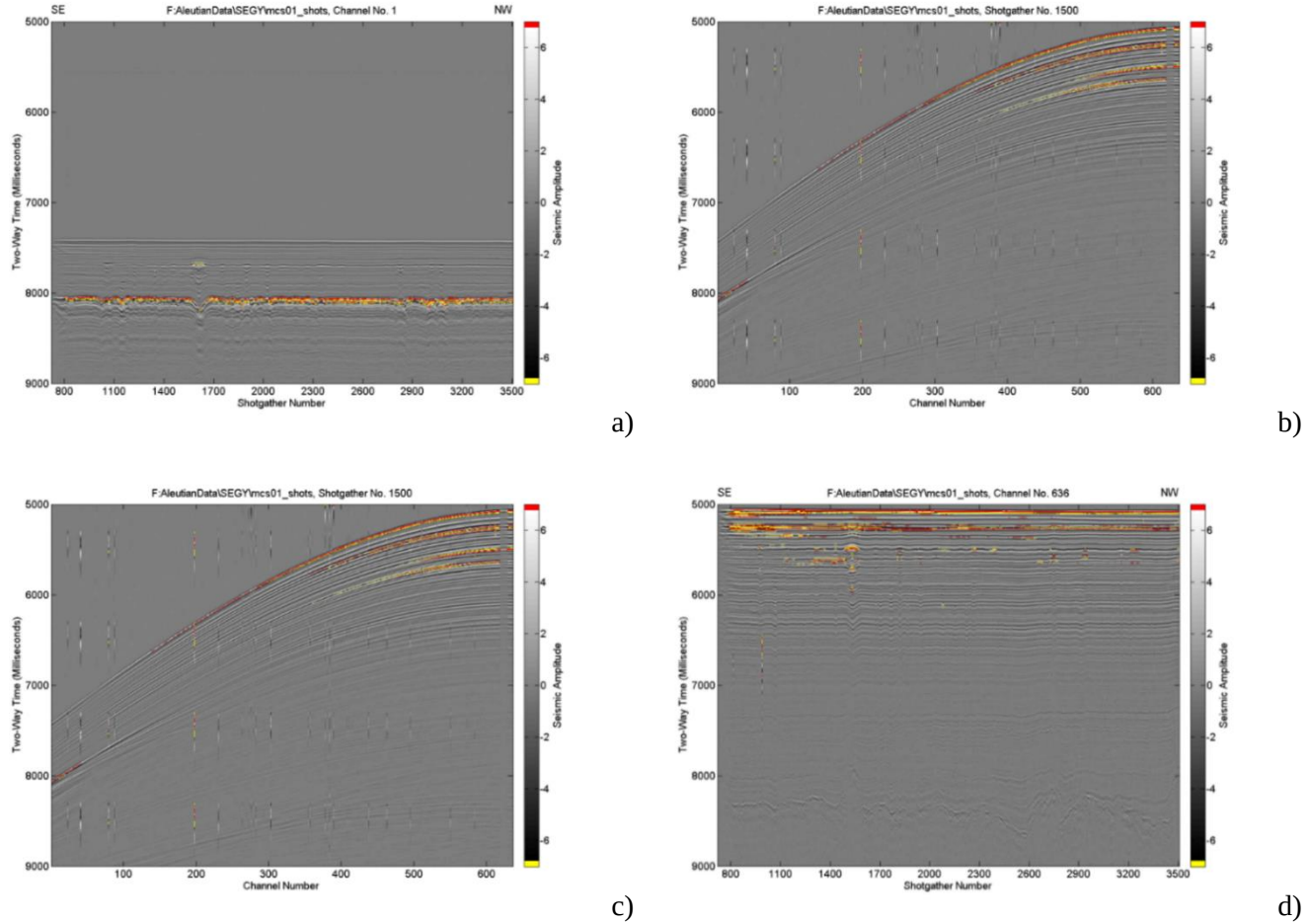

Figure 4. MCS01 a) far offset, b) shotgather 1500, c) shotgather 1500, and d) near offset.

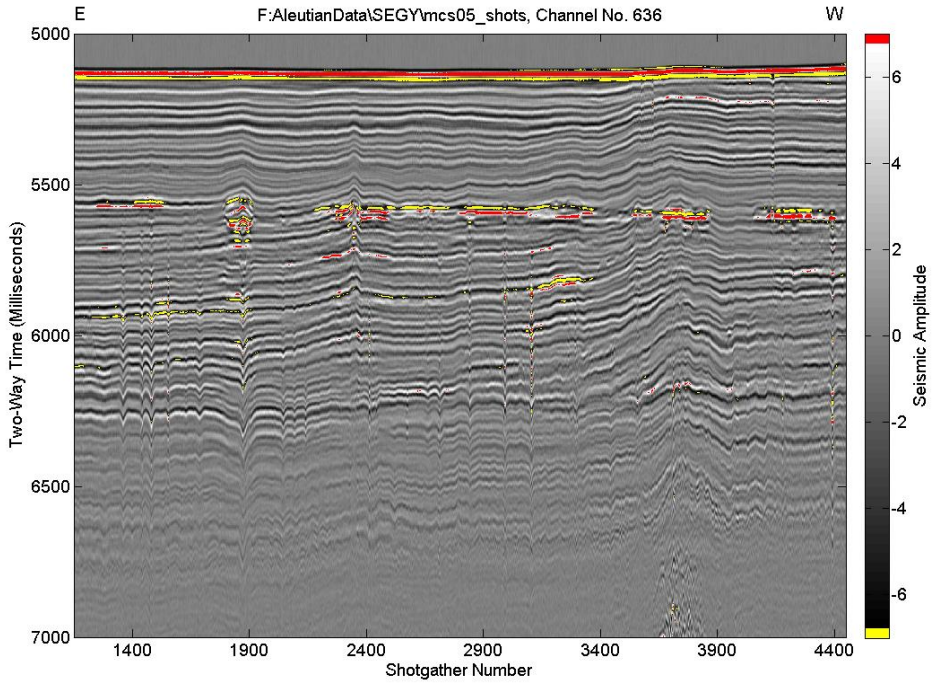

a)

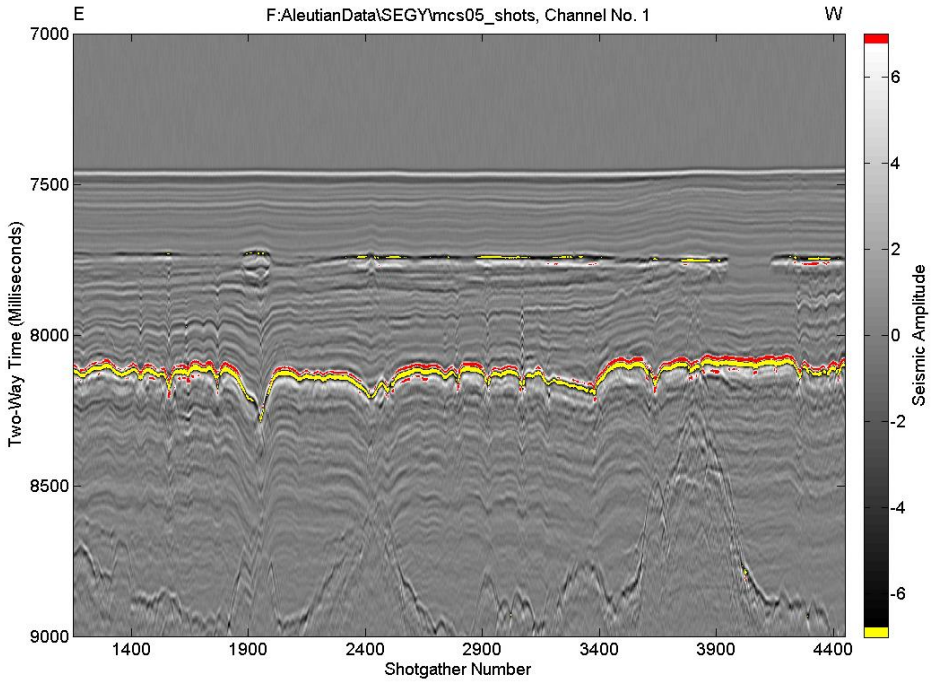

b)

Figure 5. MCS05 – BSR-GH cuts across sedimentary structures.

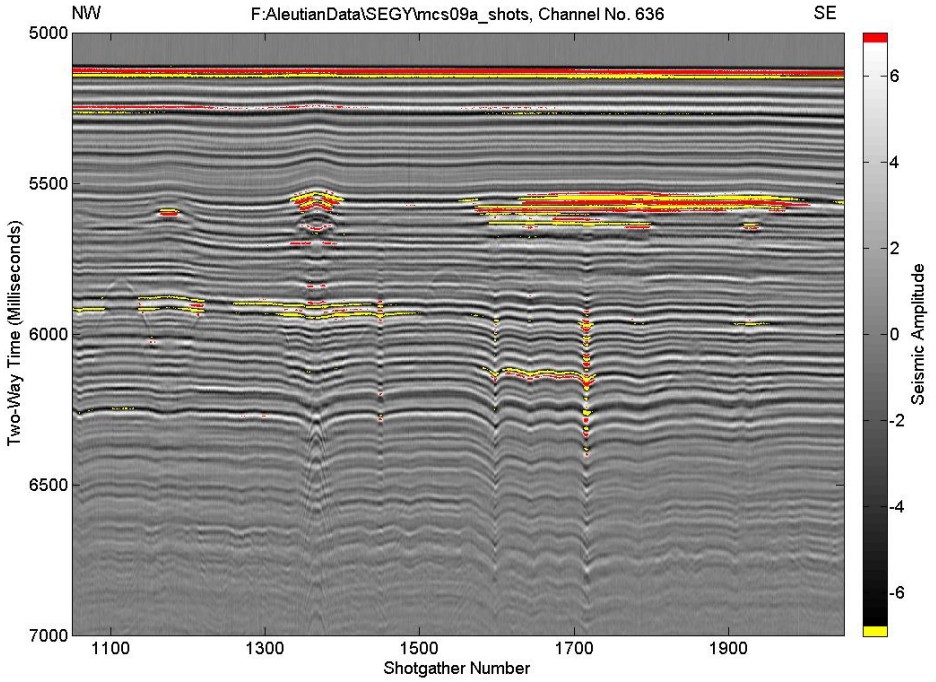

a)

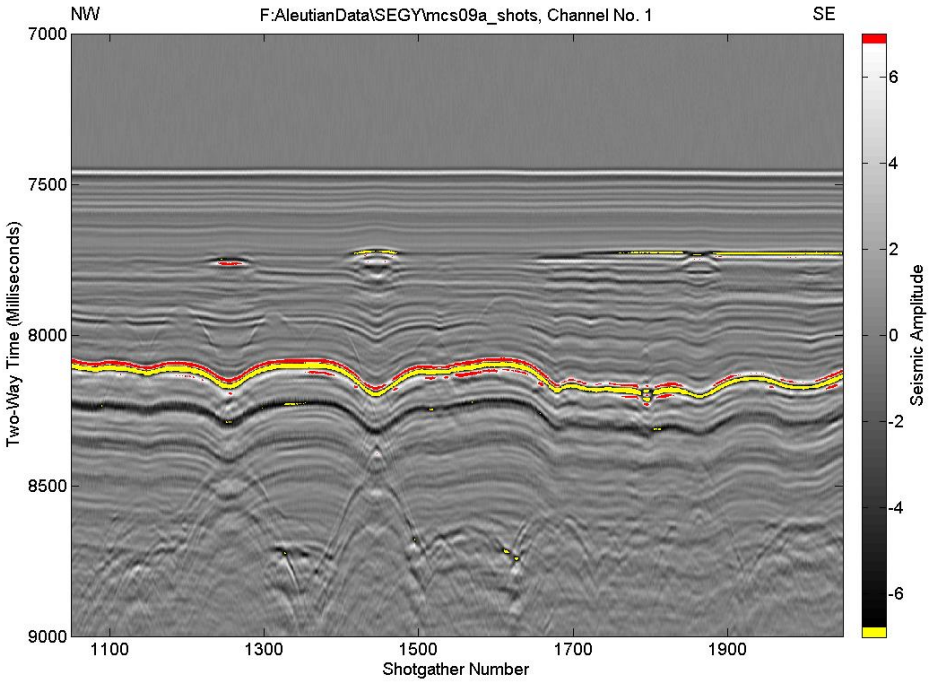

b)

Figure 6. MCS09A – very strong GH-BSR, minor plumes; plumes show up much better in far offset data.

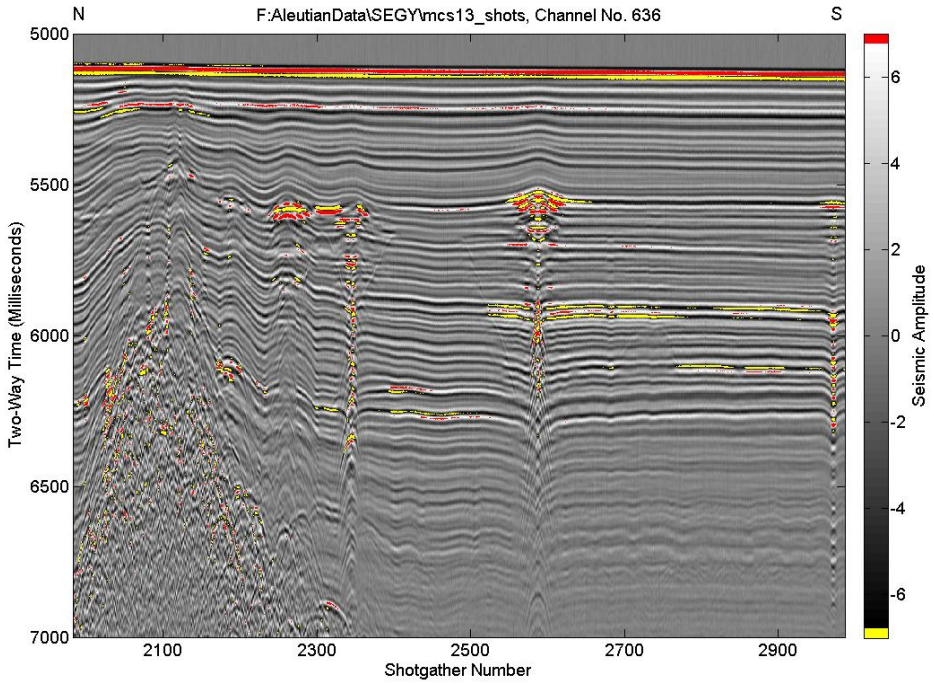

a)

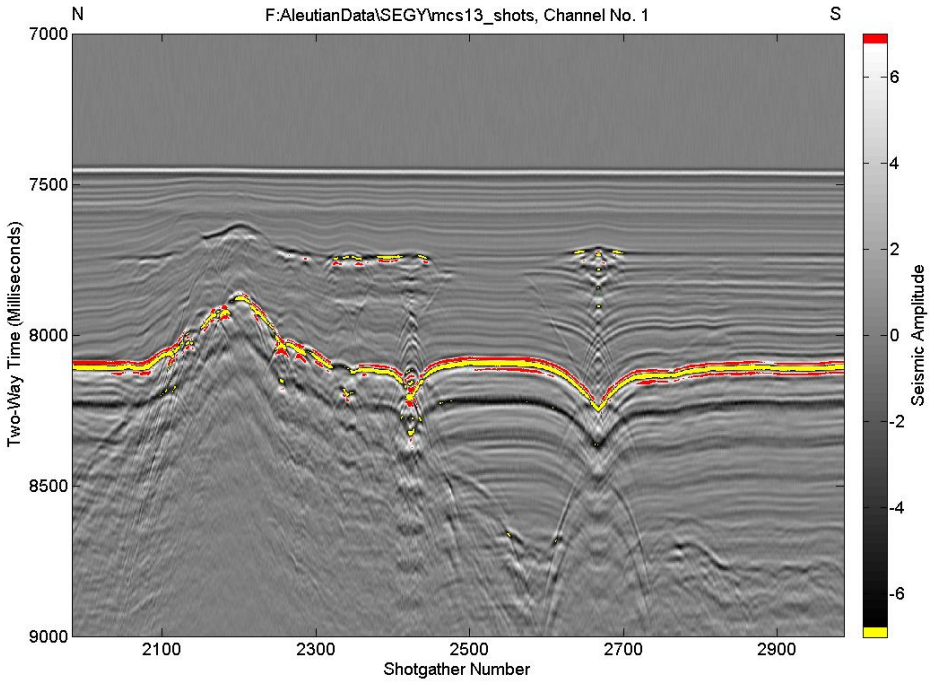

b)

Figure 7. MCS13 – interesting plume far to the side of basement high that intrudes near to the surface.

4.3 THERMAL AND CELLULAR CONVECTION IN A POROUS MEDIUM

Heat in the Earth is transported by three main mechanisms that can be described as radiative, conductive, and convective. Within the crust of the Earth, the dominant mechanism of transport for most of the depth of the crust is conductive (Jaupart and Mareschal, 2011). Yet within the top most layers of the crust, to depths sometimes as great as 10 km, heat may be transported by convective processes. As marine sediments are overwhelmingly fully saturated, the behavior of fluids in saturated porous geologic materials will be essential to understand the physical and chemical evolution of VAMP structures. Consider a horizontal saturated permeable layer heated from below analogous to Rayleigh-Bénard flow. To investigate convective processes in the upper layers of the crust it is frequently necessary to consider mathematical models of fluid flow in porous media. In general form we write a system of coupled partial differential equations in vector form that includes equations for momentum, mass, energy, and an equation of state, sometimes referred to as the equations of Horton, Rogers, Lapwood flow for saturated media..

4.3.1 Horton-Rogers-Lapwood Flow

Buoyancy-driven flows and their stability have been studied theoretically and experimentally for nearly 150 years (Batchelor, 1967; Turner, 1973). The early foundations for the momentum equation of fluid flow began with the development of Darcy's law (Darcy, 1856) to relate the mean flow and the pressure gradient at the macroscopic scale in a porous medium. Several decades later the Bénard problem of a homogeneous fluid heated from below and cooled from above was formulated through the laboratory experiments of Bénard (1900, 1901). The theoretical foundations of Rayleigh-Bénard cellular convection resulted from the interpretations

of Henri Bénard's experiments by Lord Rayleigh (1916). More recently, the so-called Horton-Rogers-Lapwood (or just Lapwood) problem provides the porous media analog to the Bénard problem (Nield and Bejan, 1992, 2006). Horton and Rogers (1945) investigated the temperature gradient needed for the onset of convection in a geologic medium; independently, Lapwood (1948) carried out a similar investigation and considered several boundary conditions.

Rogers and co-workers (Morrison, Rogers, and Horton, 1949; Rogers and Schilberg, 1951; Morrison and Rogers, 1952) reported on experiments to demonstrate thermal cellular convection in porous media. Wooding (1957, 1958, 1963, 1964) published a series of papers on his experimental results. Other important results are found in papers from Elder (1967), Katto (1967), and Bories (1970a, b). See also Saffman and Taylor (1958), Wooding (1960), and a review by Richardson (1961). The experiments reported above confirmed the onset criteria predicted from theory (Scheidegger, 1974).

4.3.2 Structural Deformation Studies

Experimental studies of density controlled deformations in soft, water-saturated sediments with reverse density gradient stratifications (Anketell and Dzulynski, 1968a, b; Anketell et al, 1970) provide a corroborative supplement to the Lapwood problem. Of interest are their results for sedimentary systems consisting of two layers differing in density, separated by an interface with a reversed density gradient. Deformation studies on sedimentary systems, which display viscous or plastic properties and consist of statistically homogeneous members, follow regular convective patterns and show the same patterns known to occur in the experimental results of Bénard (1901) with adverse thermal gradients in fluids.

Under conditions of perfect statistical heterogeneity, deformation of the interface produces regular hexagonal structures which are essentially identical to those produced by convection in fluids heated from below. The diameters of the columns are roughly proportional to the thickness of the members involved in the deformation (Anketell et al, 1970).

4.3.3 Thermals, Plumes, and Cellular Convection

Instabilities in fluids result when variations in fluid density are present as a result of variations in temperature, salinity, or both (Phillips, 1991). Isolated heat sources give rise to thermals and plumes. Sustained heat sources generate plumes, whereas if the heat source is of short duration the event is called a thermal as it becomes detached from its source (Jaupart and Mareschal, 2011). Thermals and plumes and may be either laminar or turbulent.

When the heat source extends over a large area, cellular convection may develop when a fully saturated porous medium is heated from below and cooled from above. Key difference from the case of an isolated source is that it takes a minimum amount of heating for convection to occur. This form of convection has been called a porous medium analog of Rayleigh-Bénard convection. With porous media convection, organized cellular motion, as a result of an internal instability, becomes significant in order to achieve equilibrium vs purely conductive heat flux in which the interstitial fluid can remain in equilibrium and at rest (Phillips, 1991).

4.4 RESEARCH GOALS

Buoyancy has long been recognized as an issue in formation and emplacement of marine gas hydrates, but has not been seen as a driving mechanism in early accumulation models. It is recognized that thermogenic methane, when found in hydrates in marine accumulations has likely originated elsewhere and transported to

its emplacement location through fractures by capillary or buoyancy forces. Liu and Flemings (2006, 2007) develop a reactive-front model to develop a multi-component, multi-phase model for the dynamic effects of salinity, temperature, pressure, and hydraulic properties within the hydrate stability zone. Moderately high heat flow in the Aleutian Basin and the presence of plume-like structures suggest buoyancy is a major force. We broaden the focus to methane-hydrate systems to better identify the relationship between the bottom of the hydrate stability zone with the stems of free methane gas as evident from VAMPs identified in the Aleutian Basin of the Bering Sea.

With the moderately-high heat flow of the Aleutian Basin and the abyssal waters just above freezing, we may anticipate the shallow sediments offer a porous medium analog of the classic Bénard problem. Seismic evidence (of the large scale plume-like structures and their areal abundance [Scholl and Hart, 1993]) further encourages this suggestion. With the sedimentary record largely undisturbed, the Aleutian Basin provides an opportunity to investigate the physical mechanisms that lead to these plume-like structures and their related methane-hydrate systems. In this section we focus attention on the physical mechanisms of buoyancy-driven flow.

The approach is outlined below to calculate the hydrodynamic stability in a horizontal layer between the BSR-GH and BSR-DB. We ask the question: "Do the presence, abundance, and density of velocity-amplitude anomaly structures (VAMPs) in the deep-waters of the Aleutian Basin represent cellular convection in a porous medium heated from below?"

Research Hypothesis: Velocity-amplitude anomaly structures (VAMPs) in the deep waters of the Aleutian Basin are the result of buoyancy-driven flow and cellular convection in a porous medium with heating from below.

Corollary: Cellular convection controls the distribution of the VAMPs.

Description: Unstable density structures above a quantifiable critical value seek stable structures that permanently alter the dynamics of the system. The Aleutian Basin may present an analog of the classical Bénard problem for a porous medium [Lapwood problem] testable with stability analysis and reaction-front modeling against evidence available from seismic analysis. Three types of buoyancy driven structures are possible:

A. Thermals – A fixed amount of energy is released and a volume of heated fluid called a thermal detaches from the source. The thermal grows due to diffusion or turbulent entrainment, but the total amount of energy remains constant.
B. Plumes – With an isolated steady source, a narrow upwelling structure called a plume extends vertically. A plume is characterized by a large head region at the top of a thinner stem region. Use term CHIMNEY also!
C. Cellular Convection – A homogeneous fluid layer that is heated from below and cooled from above takes a minimum amount of heating for convection to appear. As has been shown by laboratory experiments and theoretical modeling, the convection develops a cellular structure.

4.4.1 Critical Parameters for Cellular Convection

The Bénard problem is defined as a homogeneous fluid, lying between two infinite, parallel horizontal boundaries with heating from below and cooling from above, subjected to a linear temperature gradient. Heating from below is said to impose an adverse (unstable) temperature gradient. The natural tendency of the fluid to move because of buoyancy, will be inhibited by its own viscosity and thermal diffusivity. Therefore, thermal instability will manifest itself only when the adverse temperature gradient exceeds a certain critical value.

A non-dimensional Rayleigh number is used to characterize instability in both fluids and porous media. However, the formula's and meaning are somewhat different. To distinguish between the two, we will use Rayleigh number to represent the non-dimensional parameter for fluids and the name Rayleigh-Darcy number to represent the equivalent non-dimensional parameter for porous media. The non-dimensional Rayleigh number characterizes instability of a fluid column as the ratio of buoyancy forces to viscous forces. This Rayleigh number for fluids is written

$$Ra = \frac{\rho^2 g c_p \alpha |T_1 - T_2| Z^3}{\mu K_T}$$

The Rayleigh-Darcy number for porous media is

$$Ra_D = \frac{\rho^2 g c_e \alpha |T_1 - T_2| k_h Z}{\mu K_{Te}}$$

Alternatively, the Rayleigh-Darcy number can be written as the product of the Rayleigh number for fluids and the Darcy number (Da); i.e.

$$Ra_D = RaDa$$

where the Darcy number (Da) is the non-dimensional ratio of medium permeability (k_h) to the square of domain thickness (Z), written as

$$Da = \frac{k_h}{Z^2}$$

A necessary condition for instability is $dT/dz < 0$ when density $\rho(T)$ decreases with T over the range of T considered, or $dT/dz > 0$ when $\rho(T)$ increases with T; neither is a sufficient condition (Furbish, 1997).

The critical Rayleigh-Darcy number is

$$(Ra_D)_{CR} = 4\pi^2 \cong 40.0$$

This critical value given is specific to an isotropic medium with constant temperature and zero volume flux boundaries on the upper and lower surfaces (Phillips, 1991). Experiments have typically shown the number to be somewhat lower than the theoretical values. everal factors that may influence the value (above or below) to differ from the theoretical value (Furbish, 1997); these include:

1) Uncertainties in the parameters that comprise the Rayleigh-Darcy number.
2) Transversely anisotropic conditions, such as when $k_z < k_{xy}$, may actually increase the critical value.
3) The critical value of the Rayleigh-Darcy number for porous media is also influenced by the boundary conditions.

In addition, above the critical value, as the Rayleigh-Darcy number increases and changes modes, cell patterns and motions become more complex (Furbish, 1997).

4.4.2 Discussion on parameters

The parameters of the Rayleigh-Darcy equation are defined in Table 4-I. Values assigned for the calculations are detailed in Table 4-II.

TABLE IV. Parameter Definitions With Units and Derived Units

Parameter Definitions with Units:			
ρ	=	Fluid density	[kg m^{-3}]
g	=	Gravitational acceleration	[m s^{-2}]
c_e	=	Effective specific heat	[kJ/kg-K]
c_p	=	Specific heat at constant pressure	[kJ/kg-K]
α	=	Coefficient of thermal expansion	[K^{-1}]
T_1	=	Lower boundary temperature	[degrees K]
T_2	=	Upper boundary temperature	[degrees K]
k_h	=	Intrinsic permeability of porous medium	[mDarcy] (convert to m^2)
Z	=	Thickness	[m]
μ	=	Dynamic viscosity	[Pa-s]
K_T	=	Thermal conductivity	[W m^{-1} K^{-1}]
K_{Te}	=	Effective thermal conductivity	[W m^{-1} K^{-1}]
Derived Units:			
1 Joule		= 1 kg-m2 / s^2	
1 Pascal		= 1 kg / (m-s^2)	
1 Watt		= 1 kg-m2 / s^3	
1 mDarcy		= 10^{-15} m^2	
1 mCal / (cm-sec-deg C)		= 0.41868 Watts / (m-K)	

TABLE V. Parameter Values

	=		
ρ	=	Fluid density	1030.0 kg m^{-3} (seawater)
g	=	Gravitational acceleration	9.80665 m s^{-2}
c_e	=	Effective specific heat	2.093 kJ/kg-K (ice at freezing)
			2.512 kJ/kg-K (wet mud)
			1.381 kJ/kg-K (sandy clay)
			0.830 kJ/kg-K (quartz sand)
α	=	Coefficient of thermal expansion	52 X 10^{-6} K^{-1} (seawater at 0 degrees C)
			244 X 10^{-6} K^{-1} (seawater at 20 degrees C)
T_1	=	Lower boundary temperature	124 degrees C
			64 degrees C
T_2	=	Upper boundary temperature	4 degrees C
k_h	=	Intrinsic permeability of porous medium	5 to 500 mDarcy [convert to m^2]
Z	=	Thickness	2000 m
μ	=	Dynamic viscosity	20 X 10^{-3} Pa s to 250 X 10-3 Pa s (marine mud)
			1.787 X 10-3 Pa s (water at 0 degrees C)
			1.002 X 10-3 Pa s (water at 20 degrees C)
			0.547 X 10-3 Pa s (water at 50 degrees C)
			0.282 X 10-3 Pa s (water at 100 degrees C)
K_{Te}	=	Effective thermal conductivity	3.18 W m^{-1} K^{-1} (Quartz matrix [Lovell, 1985])
			1.6 W m^{-1} K^{-1} (0 degrees C)
			0.983898 W m-1 K-1 (Erickson, 1973 [DSDP Site 190])

4.5 DISCUSSION OF CALCULATIONS

For our calculations we consider two thermal gradients. For a typical value representative of the central Aleutian Basin we use a value of 60 degrees C/km. To compare we use a value of 30 degrees C/km typical of the Gulf of Mexico. There are other characteristics, such as salt domes and more complicated geology, of the Gulf of Mexico that suggest cellular convection is not likely in connection with formation of hydrates.

We show the effect from changing or varying the thermal gradient in Figure 11. First we show a plot of Rayleigh-Darcy number versus Dynamic Viscosity at the nominal layer thickness of 500 m. Curves are shown in the upper Figure 11 (a) for the two thermal gradients. The curves are exponential in character. On the right Figure 11 (b), the same calculated results are plotted as a Log-Log graph. As might be expected, the exponential curves become straight lines. The remaining results are plotted as Log-Log curves where we vary the thermal gradient, Effective specific heat, and intrinsic permeability at 4 different layer thicknesses.

We show results for thicknesses of 125 m, 250 m, 500m, and 750 m. The theoretical curve for onset of self-sustaining cellular convection is at a Rayleigh-Number of 40 represented with a dashed line. For a natural environment such as the central Aleutian Basin, it is expected that the critical onset would be greater than 40; even for a theoretical value, the value varies based on boundary conditions.

For the four cases shown in Figure 12 of Rayleigh-Darcy number versus Dynamic viscosity, the curve shifts upward as the layer thickness increases. For thicknesses greater than 250 m, cellular convection is highly likely to occur this area if the simple

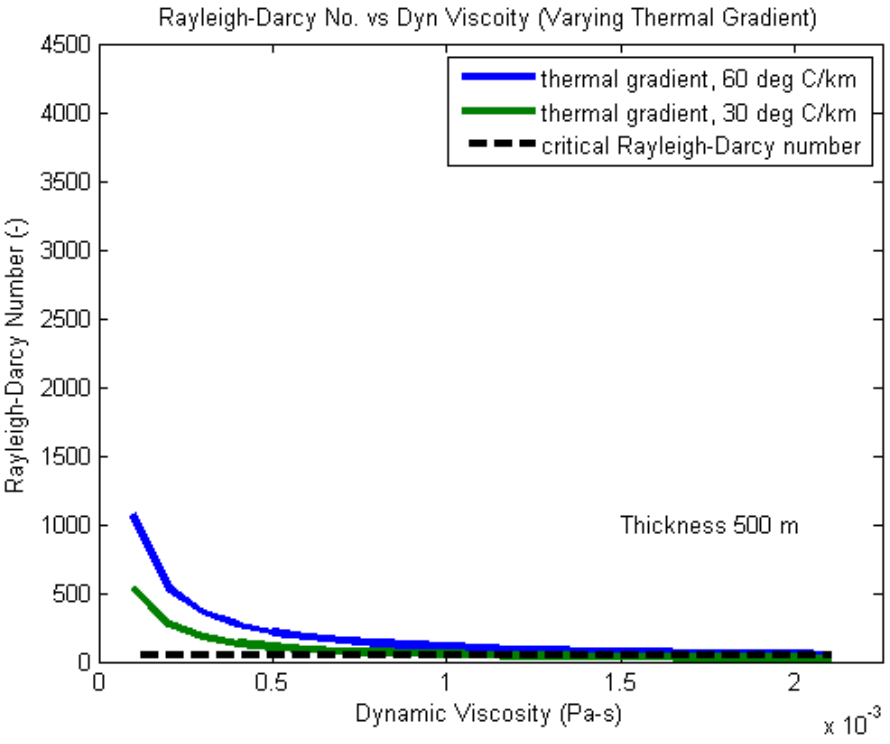

a)

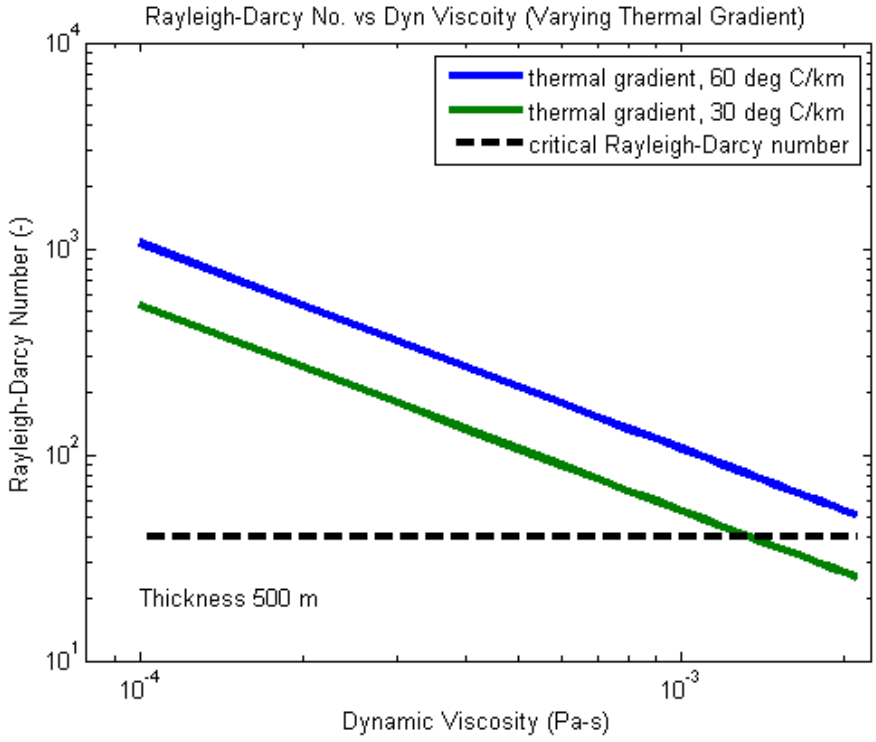

b)

Figure 8. Rayleigh-Darcy Number Versus Dynamic Viscosity for Two Values of Lower Boundary Temperature: a) Linear-Linear plot, and b) Log-Log plot..

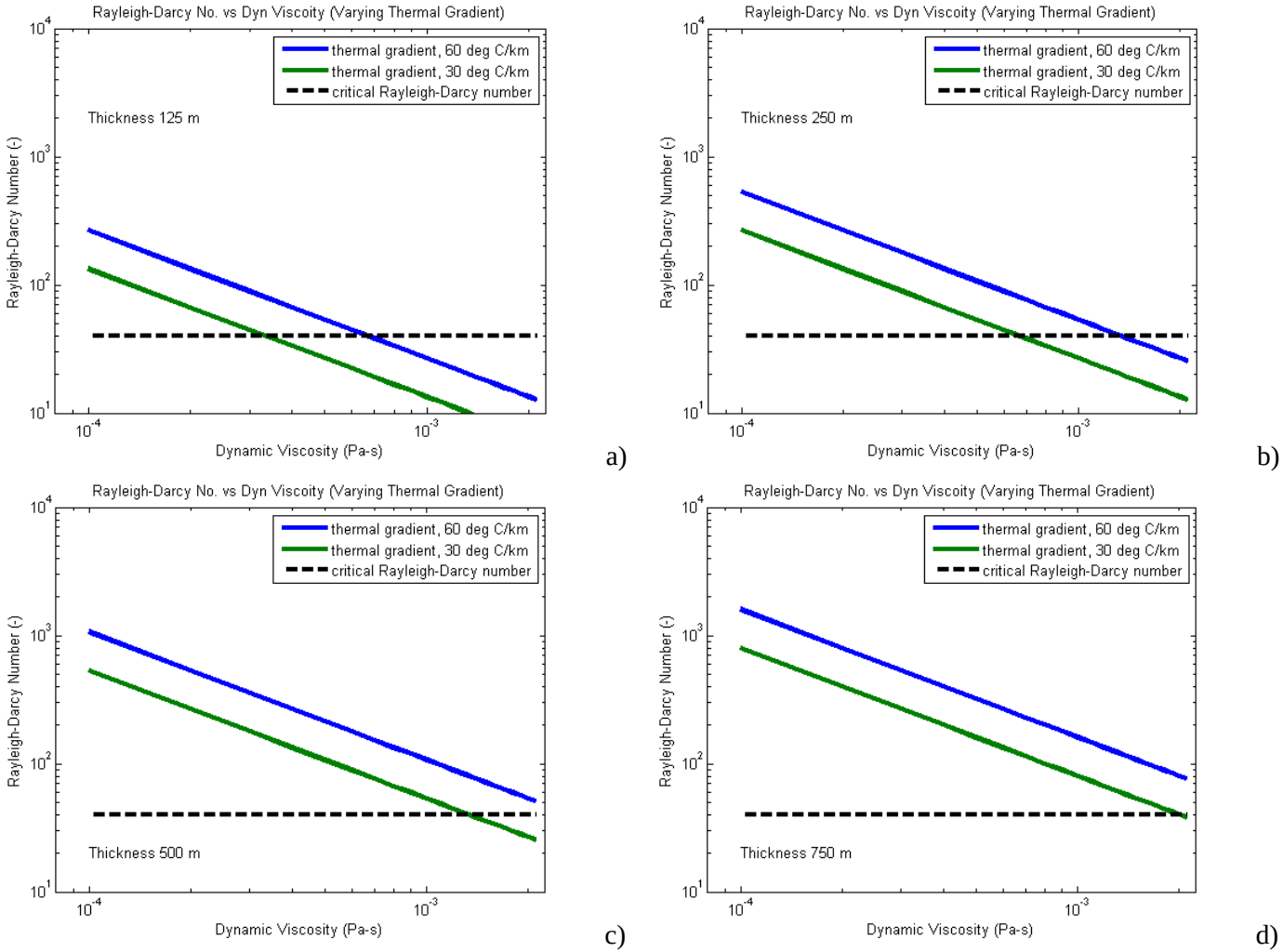

Figure 9. Rayleigh-Darcy Number versus Dynamic Viscosity for Two Values of Lower Boundary Temperature and Four Thickness Values.

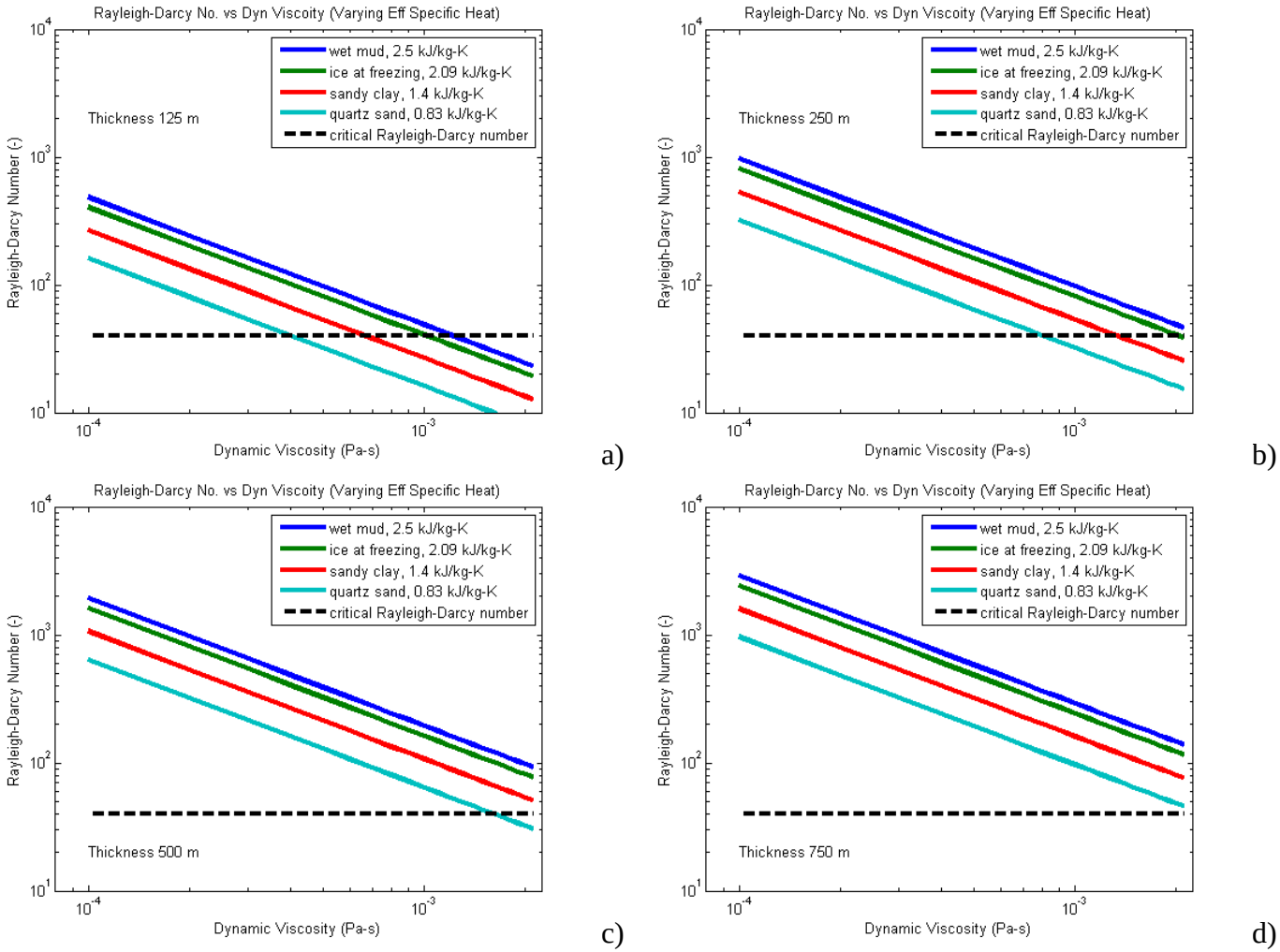

Figure 10. Rayleigh-Darcy Number versus Dynamic Viscosity for Four Values of Effective Specific Heat and Four Thickness Values.

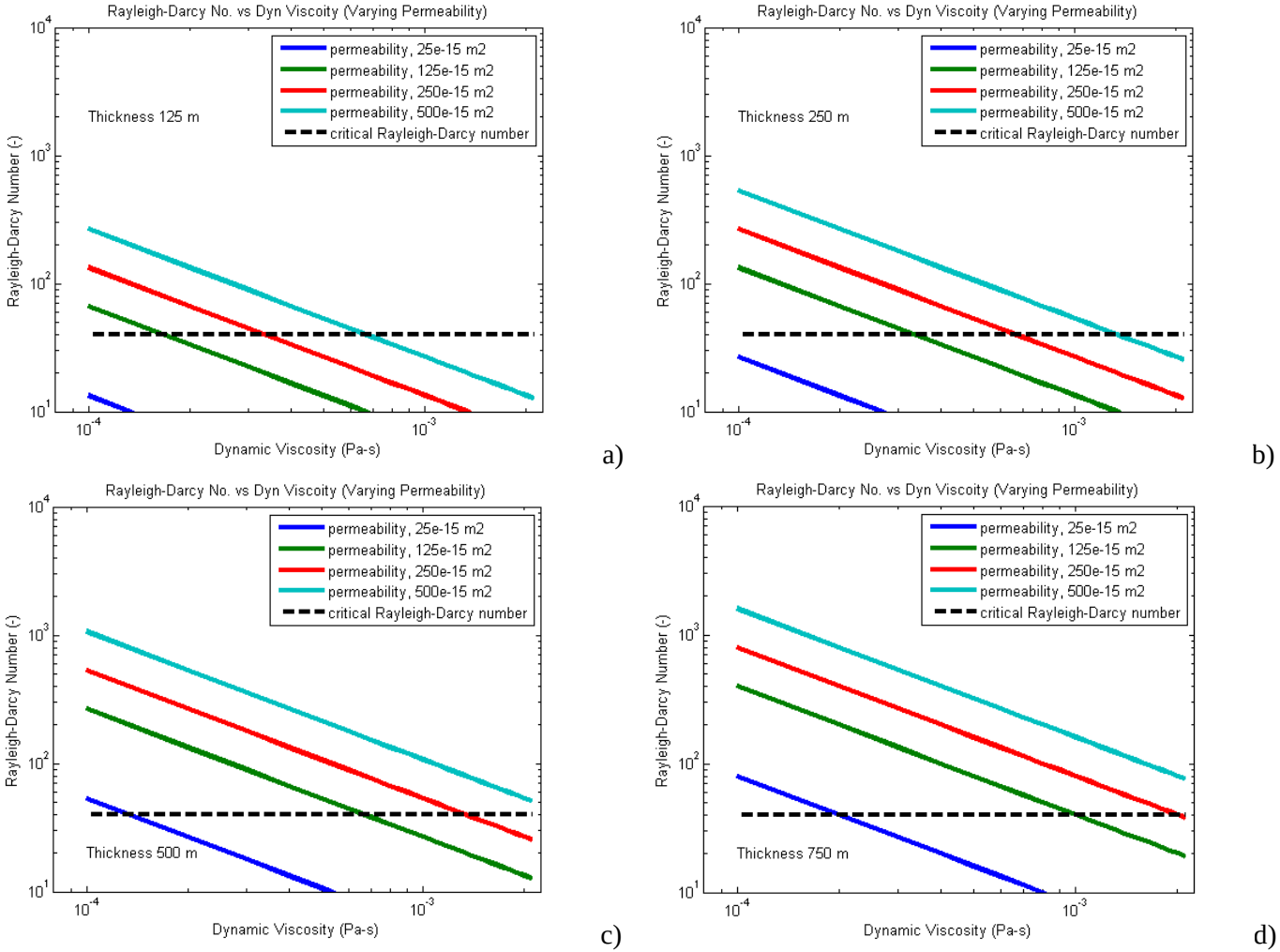

Figure 11. Rayleigh-Darcy Number versus Dynamic Viscosity for Four values of Permeability and Four Layer Thickness Values.

geometry and heating from below is maintained in porous media based on the parameter values used in these calculations.

As shown in Figure 13 we show calculated results of the Rayleigh-Darcy Number versus dynamic viscosity for four values of effective specific heat at each of the four layer thicknesses. All calculations are at the higher thermal gradient of 60 degrees C/km. Shown is Figure 14 are results of calculating the Rayleigh-Darcy Number versus dynamic viscosity at four values of layer thicknesses. Again, all calculations are at the higher thermal gradient.

4.6 CONCLUSIONS

In this paper outline our ongoing research into the speculative methane-hydrate structures of the central Aleutian Basin of the Bering Sea. We begin with a review of the areas tectonic history and the seismic evidence for presence of plume structures.

With the moderately-high heat flow of the Aleutian Basin and the abyssal waters just above freezing, we may anticipate the shallow sediments offer a porous medium analog of the classic Bénard problem. Seismic evidence of the large scale plume-like structures, and their areal abundance (Scholl and Hart, 1993) further encourages this suggestion. With the sedimentary record largely undisturbed, the Aleutian Basin provides an opportunity to investigate the physical mechanisms that lead to these plume-like structures and their related methane-hydrate systems.

Liu and Flemings (2007) developed a new conceptual model which describes the dynamic effects of a multi-component, multi-phase buoyancy-driven system to better understand how gas-rich fluids migrate into the GHSZ and how fluid focusing may influence the distribution of hydrate (Spence et al., 2010). In this system, and particularly

in low-flux systems hosted in fine-grained sediments, the gas hydrate (above the free-gas) becomes a barrier to free-gas intrusion into the GHSZ. Yet, in high flux systems, the potential exists for depletion of water and formation of pore-water too saline to promote continued hydrate formation (Liu and Flemings, 2007).

We have focused our attention to hydrodynamic processes relevant to VAMP structures (from the central Aleutian Basin) as identified from seismic analysis, and 1D inversion. Specific focus is to understand the dynamics of the layer between the two thermobaric boundaries notably present in the central Aleutian Basin. We have calculated the Rayleigh-Darcy Number for conditions relevant to establish that self-sustaining cellular convection is feasible for layer thicknesses greater than 250 m. The stability criteria of the Rayleigh-Darcy number in a porous medium heated from below is greatly exceeded in the central Aleutian Basin. Therefore, cellular convection is feasible, though not yet confirmed. However other conditions need to be met for cellular convection to occur.

ACKNOWLEDGEMENTS

The MGL1111 data sets were made available to us though the courtesies of Dr. Ginger Barth, U.S. Geological Survey, and Dr. Warren Wood, Naval Research Laboratory, and the support of Rose Anne Weissel, Marine Geoscience Data System, LDEO, Columbia University.

REFERENCES

Atwater T., 1970. Implications of plate tectonics for the Cenozoic tectonic evolution of western North America. *Geol. Soc. Am. Bull.*, v. 81, p. 3,513-3,536.

Barth G. A., Scholl D. W. and Childs, J. R.; 2006. Possible deep-water gas hydrate accumulations in the Bering Sea. *Fire in the Ice, Methane Hydrate Newsletter*, 6 (3), p. 10-11.

Barth G., Childs J. and Wood, W., 2013. Multi-Channel Seismic Shot Data from the Bering Sea acquired during the R/V Marcus G. Langseth expedition MGL1111 (2011). Interdisciplinary Earth Data Alliance (IEDA). doi:10.1594/IEDA/318037.

Bénard H., 1901. *Ann. Chim. Phys.*, Series 7, v. 23, p. 62-144.

Berndt C., Bunz S., Clayton T., Mienert J. and Saunders M., 2004. Seismic character of bottom simulating reflectors: examples from the mid-Norwegian margin. Marine and Petroleum Geology 21, 723-733.

Byrne T., 1979. Late Paleocene demise of the Kula-Pacific spreading center. *Geology*, 7 (7), 341-344.

Carcione J., 2009. Theory and modeling of constant-Q P- and S-waves using fractional time derivatives. *Geophysics*, 74 (1), T1-T11.

Christeson G.L. and Barth G.A., 2015. Aleutian basin oceanic crust. Earth and Planetary Science Letters, 426, 167-175.

Clark, R. A., Benson, P. M., Carter, A. J. and Guerrero Moreno C. A., 2009. Anisotropic P-wave attenuation measured from a multi-azimuth surface seismic reflection survey. *Geophys. Prosp.*, v. 57, p. 835-845.

Cooper A. K., Marlow M. S. and Scholl, D. W., 1977. The Bering Sea – A multifarious marginal basin. In: Talwani, M; Pitman, W. C; Editors. *Island Arcs, Deep Sea Trenches and Back-Arc Basins*, Am. Geophys. Union, p. 437-450.

Cooper A. K., Scholl D. W., Marlow M. S., Childs J. R., Redden G. D., Kvenvolden, K. A. and Stevenson, A. J.; 1979. Hydrocarbon potential of Aleutian Basin, Bering Sea. *Am. Assoc. Petr. Geol. Bull.*, v. 63 (11), p. 2070-2087.

Cooper A. K., Marlow M. S. and Scholl D. W., 1987. Geologic framework of the Bering Sea crust (Chapter Five). *Geology and Resource Potential of the Western North America and Adjacent Ocean basins – Beaufort Sea to Baja California*, Circum-Pacific Council Energy Miner. Resour., p. 73-102.

Cooper A. K., Marlow M. S., Scholl D. W. and Stevenson A. J., 1992. Evidence for Cenozoic crustal extension in the Bering Sea region. *Tectonics*, v. 11 (4), p. 719-731.

DeLong S. E., Fox P. J. and McDowell F. W., 1978. Subduction of the Kula Ridge at the Aleutian Trench. *Geol. Soc. Am. Bull.*, v. 89, p. 83-95.

Erickson A., 1973. Initial report on downhole temperature and shipboard thermal conductivity measurements, Leg 19, Deep Sea Drilling Project. *Initial Reports of the Deep Sea Drilling Project*, Vol. 19. U. S. Gov. Print. Off., p. 643-656.

Foster T. D., 1962. Heat-flow measurements in the Northeast Pacific and in the Bering Sea. *J. Geophys. Res.*, v. 67 (7), p. 2991-2993.

Hein J. R., Scholl D. W., Barron J. A., Jones M. G. and Miller, J., 1978. Diagenesis of late Cenozoic diatomaceous deposits and formation of the bottom simulating reflector in the southern Bering Sea. *Sedimentology*, v. 25 (2), p. 155-181.

Karl H. A., Carlson P. R. and Gardner J. V., 1996. Aleutian Basin of the Bering Sea. In: Gardner, J. V.; Field, M. E.; Twichell, D. C.; Editors. *Geology of the United States Seafloor: The View from Gloria*. Cambridge University Press, 374 pp.

Lee H. J., 1973. Measurements and estimates of engineering and other physical properties, Leg 19. *Initial Reports of the Deep Sea Drilling Project*, Vol. 19. U. S. Gov. Print. Off., p. 701-719.

Liu X. and Flemings P. B., 2007. Dynamic multiphase flow model of hydrate formation in marine sediments, *J. Geophys. Res.*, v. 112, B03101, doi: 1029/2005JB004227, 23 pp.

Lonsdale P., 1988. Paleogene history of the Kula plate: Offshore evidence and onshore implications. *Geol. Soc. Am. Bull.*, v. 100 (5), p. 733-754.

Marlow M. S. and Cooper A. K. 1983. Wandering terranes in southern Alaska: The Aleutia Microplate and implications for the Bering Sea. *J. Geophys. Res.*, v. 88 (B4), p. 3439-3446.

Marshall V. B., Cooper A. K. and Childs J. R., 1978. Recent heat flow measurements in the Aleutian basin, Bering Sea (abs). *EOS, Trans. Am. Geophys. Union*, v. 59, p. 384.

Ng D. and Martinson D., 2011. RV Langseth Data Reduction Summary, MGL1111, Dutch Harbor, AK – Dutch Harbor, AK, Not Final, V1.2, 2011-09-02. Lamont Doherty Earth Observatory, Columbia University, 64 pp, +5 Appendices.

Nichols H. and Perry R. B., 1966. *Bathymetry of the Aleutian Arc, Alaska*. Monograph 3, Environ. Sci. Serv. Admin.

Quan Y. and Harris J. M., 1997. Seismic attenuation tomography using the frequency shift method. *Geophysics*, v. 62 (3), p. 895-905.

Rayleigh L., 1916. On convection currents in a horizontal layer of fluid, when the higher temperature is on the under side. *Phil. Mag.*, Series 6, v. 32 (192), p. 529-546.

Rea D. K. and Dixon, J. M., 1983. Late Cretaceous and Paleogene tectonic evolution of the North Pacific Ocean. *Earth Planet. Sci. Lett.*, v. 65 (1), p. 145-166.

Rearic D. M., Williams S. R., Carson P. R. and Hall, R. K.; 1988. *Acoustic evidence for gas-charged sediment in the abyssal Aleutian Basin, Bering Sea, Alaska*. Dept. of the Interior, U. S. Geological Survey, Open-File Report 88-577.

Scholl D. W., Buffington E. C. and Hopkins D. M., 1968. Geologic history of the continental margin of North America in the Bering Sea. *Marine Geol.*, v. 6, p. 297-330.

Scholl D. W. and Creager, J. S., 1973. Geologic synthesis of Leg 19 (DSDP); Far North Pacific, and Aleutian Ridge, and Bering Sea. *Initial Reports of the Deep Sea Drilling Project*, Vol. 19. U. S. Gov. Print. Off., p. 897-913.

Scholl D. W., Buffington E. C. and Marlow M. S., 1975. Plate tectonics and structural evolution of the Aleutian-Bering Sea region. In: Forbes, R. B. Editor. *Contributions to the Geology of the Bering Sea Basin and Adjacent Regions*. Geol. Soc. Am., Special Paper 151, p. 1-32.

Scholl D. W. and Cooper A. K., 1978. VAMPs – Possible hydrocarbon-bearing structures in Bering Sea basin. *Am. Assoc. Petr. Geol. Bull.*, v. 62 (12), p. 2,481-2,488.

Scholl D. W., Vallier, T. L. and Stevenson A. J., 1983. Arc, forearc, and trench sedimentation and tectonics; Amilia Corridor of the Aleutian Ridge. Watkins, J. S.; Drake, C. L.; Editors. *Studies in Continental Margin Geology, AAPG Memoir No. 34*, p. 413-439.

Scholl D. W., Stevenson, A. J., Vallier T. L., Ryan H. F. and Geist E. L., 1989. Aleutian Arc-trench system: Perspective of ocean margin evolution controlled by regional changes in plate-boundary conditions (abs.). *Twenty-Eighth Intern. Geolog. Congr., Washington, DC, 9-19 July 1989*, v. 3, p. 52-53.

Scholl D. W. and Stevenson A., 1990. Was the Aleutian Basin more enclosed, its deeps oxygen deficient, and the geothermal gradient steepened in the Middle Tertiary? Implications for the petroleum potential of the Bering Sea (abs). *Fifth Circum-Pacific Energy and Mineral Resources Conference, Honolulu, HI, 29 July-3 August 1990*, p. 1000.

Scholl D. W. and Hart P. E., 1993. Velocity and amplitude structures on seismic-reflection profiles – Possible massive gas-hydrate deposits und underlying gas accumulations in the Bering Sea Basin. In: Howell, D. G.; Editor. *The Future of Energy Gases*. U. S. Geol. Survey., Professional Paper 1570, p. 331-351.

Scholl D. W., Barth G. A. and Childs, J. R.; 2009. Why hydrate-linked velocity-anomaly structures are common in the Bering Sea Basin: A hypothesis. In: Collett, T.; Johnson, A.; Knapp, C.; Boswell, R.; Editors. *Natural Gas Hydrates – Energy Resource Potential and Associated Geologic Hazards*, AAPG Memoir, Vol. 89, p. 308-323.

Sen M. and Stoffa P. L., 1995. *Global Optimization Methods in Geophysical Inversion*. Elsevier Science, B. V., 281 pp.

Shor G. G., 1964. Structure of the Bering Sea and the Aleutian Ridge. *Marine Geol.*, 1, 213-219.

Sliter, R., Barth, G., Wood W. T. and Childs, J., 2011. Processed multi-channel seismic data in the Bering Sea acquired during R/V Marcus G. Langseth expedition MGL1111 (2011). Academic Seismic Portal at UTIG, Marine Geoscience Data System. http://dx.doi.org/10.1594/IEDA/500056

Wallace W. K. and Engebretson,D. C., 1984. Relationships between plate motions and Late Cretaceous to Paleogene magmatism in southwestern Alaska. *Tectonics,* v. 3 (2), p. 295-315.

Watanabe T., Langseth M. G. and Anderson R. N., 1977. Heat flow in back-arc basins of the western Pacific. In: Talwani, M; Pitman, W. C; Editors. *Island Arcs, Deep Sea Trenches and Back-Arc Basins,* Am. Geophys. Union, p. 137-161.

Wood W. T., 1993. *Least Squares Inversion of Field Seismic Data for an Elastic 1-D Earth*. Ph.D. Dissertation, The University of Texas, Austin, May 2003, 284 pp.

.

CONCLUSIONS

Chapter 1: The purpose of this paper is to demonstrate that multiple gas hydrate models to predict sonic delays for unconsolidated sediments can be brought together into a single unified effective medium model and resolve the controversy of whether perfectly smooth or infinitely rough sphere models validate the Mallik well log data.

Sava and Hardage (2006) conclude that the smooth sphere end point of the Walton (1987) model is most appropriate to model the Mallik well log data. Cordon et al (2006) and Sriram et al (2014), each with differing modifications, use the Dvorkin-Nur model for an infinitely rough sphere to conclude the rough sphere model provides a good fit. In Chapter 1 (this Dissertation) we use the extended Walton Model (Jenkins, 2005), which brings the two end points of the original Walton model (Jenkins et al, 2005) into a single model, and show that the Dvorkin-Nur rough sphere model is mathematically equivalent to the rough sphere end point of the original and extended Walton models.

Results of this unified effective medium model show that the friction parameter is in the neighborhood of 0.2, much closer to the smooth sphere model than the rough sphere model contrary to assertions in Cordon et al (2006) and Sriram et al (2014). The modifications to the rough sphere Dvorkin-Nur model in Cordon et al (2006) are similar to the approach taken in our paper. Cordon et al (2006) did not recognize that the

Dvorkin-Nur model was mathematically identical to the rough sphere endpoint of the extended Walton model (Walton, 1987; Jenkins et al, 2006). As we have shown here, the starting models in Chapter 1 and in Cordon et al (2006) are identical.

The approach taken in Sriram et al (2014) for modifying the Dvorkin-Nur model offers merit for further development since it is based on physics rather than empirical parameters. Further work to compare this unified model with Sriram et al (2014) is warranted. And, as stated in the Chapter 1, statistical modeling approaches, though computationally intensive, should be more generally used to validate rock physics approaches.

Chapter 2: Calculation of the semblance velocity spectra can be reformulated as a spatial covariance problem to obtain a higher resolution velocity estimate yet has not received widespread acceptance because of the excessive computational cost. This Chapter demonstrates that the temporal covariance approach can be used as an intermediate step to obtain the identical spatial covariance solution at greatly reduced computational cost.

The merit of using a spatial covariance approach for semblance velocity calculations was first demonstrated in the early 1990s. Recently, while we were developing this approach for recovering the spatial covariance Eigenvectors from the temporal covariance Eigenvectors at greatly reduced computational cost, Barros et al (2015) published a paper calculating a temporal covariance solution. In Barros et al (2015) the spatial covariance solution is presented as a high resolution solution and the temporal solution is considered a low resolution solution. Barros et al (2015) make an important contribution to using the temporal covariance solution to obtain a semblance velocity spectra. However, their comparison is inadequate because they used spatial

averaging to speed up the computational times for the spatial covariance solution. A similar approach was not considered for the temporal covariance solution. This spatial averaging is likely the source of the improved resolution for the spatial covariance solution, contrary to our solutions and assertion that the spatial and temporal covariance solutions are identical. Our results provide a valid comparison and suggest a way to further improve computational times and resolution for temporal covariance approaches.

An important concept behind a covariance solution is the rank reduction that is achievable. This is noted in Barros et al (2015) and also referenced Golub, B. H. and Van Loan (1996)

There are several useful paths for future work

1. Investigate role of smoothing in achieving good results in spatial covariance approach in Barros' paper.
2. Develop a methodology to apply smoothing to obtain temporal covariance results.
3. Assess whether additional data conditioning will be needed to obtain good results, and improve our knowledge on application of MUSIC algorithms.

Chapter 3: This Chapter demonstrates that using single channel, far offset seismic images improves detection of BSRs and may expand the envelope of detection.

Using three example cases detection of the BSR for the diagenic boundary is overwhelming in the single channel, far offset seismic image as the critical reflection angle is reached. Though less apparent, the presence of the gas hydrate BSRs are also easier to visually detect. Of note are the abrupt discontinuities seen in BSR-GH. Comparisons are drawn relative to the near offset and CDP stacked seismic images.

For publication additional analysis and discussion is warranted in the following areas:

1. More work is warranted to provide a baseline AVO analysis. The utility of AVO to recognize gas as the cause should be succinctly stated and verified so that we have ground truth. This will be important to better understand the gaps noticed in what is believed to be a BSR. We should also consider applying NMO to the single channel, far offset displays to that comparisons with other displays are more easily made. Additional quantitative analysis, such as computation of seismic Q, should be considered.
2. Further discussion is needed on previous use of offset stacks for pore fluids as a "direct hydrocarbon indicator". Include discussion of previous use of offset stacks for pore fluids as a "direct hydrocarbon indicator".
3. We need to provide a better explanation for the permeability drop at the diagenic boundary. The discussion on inferred thermal anomaly example case should be more clearly written. We need to explain why the pure water curve is better match (figure now in Introduction).
4. More citations are needed throughout the Chapter to include references to Boswell's papers (Boswell, 2009; Boswell and Collett, 2011; Boswell et al, 2016) and document other locations where VAMPs have been identified. An additional source of references might be Barba-rojo, 2018; Behboudr, 2018; Chekhovich, 2012; Majumdar;Cook; Shedd; Frye; 2116; McGee, 2000; Shedd;Boswell; Frye; Godfriaux; 2012. A reference for VAMPs in the central Gulf of Mexico is Madof (2018).

Chapter 4: Calculations for the Rayleigh-Darcy number in the shallow sediments of the central Aleutian Basin show that cellular convection is a viable mechanism to drive the formation of velocity amplitude anomaly (VAMP) structures.

The stability criteria of the Rayleigh-Darcy number in a porous medium heated from below is greatly exceeded in the central Aleutian Basin. Therefore, cellular convection is feasible, though not yet confirmed. Many other conditions need to be met for cellular convection to occur. More effort should be made to back up choice of property values used for various parameters in the calculations to refine the results.

Modeling studies with an appropriate simulator for porous media should be conducted to better understand length scales and flow patterns that are appropriate, then assess how well the seismic data might compare. Significant mass transfer across the upper boundary could prevent establishment of cellular convection. This could be explored with additional modeling studies. However, it is noted that there is little evidence of chimneys or fractures penetrating into the hydrate stability zone. The BSR, as a thermobaric boundary seems to be a good seal.

First, we focus on the idealized flows for cellular convection such as the Bénard problem for fluid mediums and the Lapwood problem for saturated porous mediums. Second, we focus on the more general set of hydrodynamic equations for plumes, thermals, capillary flow, and dynamically-driven reactive-front models in porous media.

Furthermore, cellular convection in porous media in comparison with cellular convection in fluids is more complex due to the following. Therefore we should consider weakly nonlinear analysis studies to investigate (Riley and Winters, 1989; Siina and Hirshida, 2010)

1. Alternative stable flows for identical operating conditions.
2. Secondary bifurcations are required for the modal exchanges which take place as the aspect ratio changes.
3. Abrupt changes in preferred flow pattern at certain critical values of the aspect ratio.

REFERENCES

Barba-rojo P. K., Solorza-Calderon S., Gonzalez-Fernandez A. and Gonzalez-Escobar M., 2018. 2D multiresolution automated system for detecting BSRs on seismic reflection images. Journal of Geophysics and Engineering, 15, 2350-2369.

Barros T., Lopes R. and Tygel, M., 2015. Implementation aspects of eigendecomposition-based high-resolution velocity spectra. *Geophysical Prospecting*, v. 63, p. 99-115.

Boswell R., 2009. Is gas hydrate energy within reach? Science, 325, 957-958.

Boswell R. and Collett T. S., 2011. Current perspectives on gas hydrate resources. Energy and Environmental Science, 4, 1206-1215.

Boswell R., Shipp C., Reichel T., Shelander D., Saeki T., Frye M., Shedd, W., Collett, T. S. and McConnell D. R. 2016. Prospecting for marine gas hydrate resources. Interpretation, 4 (1), SA13-SA24.

Behboudr E., Keshavarz, N. and Naderi A., 2018. Identification of gas accumulation adjacent to the gas hydrate bearing zone by inversion utilizing AVO attribute. Journal of Petroleum Science and Technology, 8 (3), 42-52.

Chekhovich V. D., Sukhov A. N., Sheremet O. G. and Kononov M. V., 2012. Cenozoic geodynamics of the Bering Sea region. Geotectonics, 46 (3), 212-231.

Golub B. H. and Van Loan, C. F., 1996. Matrix Computations, 3rd ed. The Johns Hopkins University Press.

Madof A. S., 2018. Gas hydrates in coarse-grained reservoirs interpreted from velocity pull up: Mississippi Fan, Gulf of Mexico. Geology, 46 (6), 559-562.

Majumdar U., Cook A. E., Shedd W. and Frye M., 2016. The connection between natural gas hydrate and bottom-simulating reflectors. Geophysical Research Letters, 7044-7051. 10.1002/2016GL069443

McGee T. M. 2000. A single-channel seismic reflection method for quantifying lateral variations in BSR reflectivity. Marine Geology, 164, 29-35.

Riley D. S. and Winters K. H., 1989. Modal exchange mechanisms in Lapwood convection. Journal of Fluid Mechanics, 204 (July 1989), 325-358.

Shedd W., Boswell R., Frye M., Godfriaux P. and Kramer K., 2012. Occurrence and nature of "bottom simulating reflector" in the northern Gulf of Mexico. Marine and Petroleum Geology, 34, 31-40.

Shiina Y. and Hirshida M., 2010. Critical Rayleigh number natural convection in high porosity anisotropic horizontal layers. International Journal of Heat and Mass Transfer, 53 (7-8), 1507-1513.

PUBLICATIONS RECORD

DARRELL A. TERRY

OSU and USC Publications (Journal Papers. Presentations, Posters)

First Author Journal Papers

Terry, D. A.; Knapp, C. C.; 2018. A Unified Effective Medium Model for Gas Hydrates in Sediments. Geophysics, 83 (6), MR317-MR332, 13 Figures, 1 Table.

Terry, D. A.; Yankovsky, E. A.; Knapp, C. C.; 2019. Subspace Solutions for Seismic Velocity Analysis. Manuscript, 34 pages, 10 Figures.

Terry, D. A.; Knapp, C. C.; 2019. Identification of Bottom Simulating Reflectors in Far-Offset Seismic Images. Manuscript, 42 pages, 7 Figures.

Terry, D. A.; Knapp, C. C.; Wilson, A.; 2019. Stability Analysis of VAMP-Hydrate Systems in the Central Aleutian Basin. Manuscript, 50 pages, 14 Figures, 4 Tables.

Co-Author Journal Papers

Williams, A. Q.; Terry, D. A.; Knapp, C. C.; 2019. Three Dimensional Thermobaric Model of a Gas Hydrate System Applied to Woolsey Mound, Northern Gulf of Mexico. Manuscript n preparation, Marine and Petroleum Geology.

Almutairi, K. F.; Knapp, C. C.; Knapp, J. H.; Terry, D. A.; 2017. Assessment of Upper Cretaceous Strata for Offshore CO2 Storage, Southeastern United States. Modern Environmental Science and Engineering, 3 (8), 532-552.

Yankovsky, E. A.; Terry, D. A.; Knapp, C. C.; 2015. Seismic and Gravity Evidence for Methane Hydrate Systems in the Central Aleutian Basin. International Journal of Earth Science and Geophysics, 1 (1), 8 p.

International Conference Proceedings

Terry, D. A.; Knapp, C. C.; 2014. Cellular Convection and Methane-Hydrate Systems in the Central Aleutian Basin. Proceedings of the 8th International Conference on Gas Hydrates (ICGH-2014), Beijing, China, 28 July-1 August 2014, Paper T1-186, 12 p.

Terry, D. A.; Knapp, C. C.; Knapp, J. H.; 2011. Effective-Medium Models and Rock Physics Analysis for Marine Gas Hydrates in Northern Gulf of Mexico. Proceedings of the 7th International Conference on Gas Hydrates (ICGH-2011), Edinburgh, Scotland, United Kingdom, 17-21 July 2011, Paper ID 170, 9 p.

Invited Talks

Terry, D. A.; 2019. Rock Physics Models and Stability Analysis Applied to Gas Hydrates. National University of Singapore, Department of Mechanical Engineering, Department Seminar, 14 February 2019, Singapore.

Terry, D. A.; 2018. A Unified Effective Medium Model for Gas Hydrates in Sediments. Oklahoma State University, Boone Pickens School of Geology, Departmental Seminar, 9 November 2018, Stillwater, OK.

Terry, D. A.; 2014. Cellular Convection and Methane-Hydrate Systems in the Central Aleutian Basin. 24 July 2014, Schlumberger Well Services, Beijing, China.

Terry, Darrell A.; Knapp, Camelia C.; Knapp, James H.; 2010. Rock Physics Models for Marine Gas Hydrates. *Gulf of Mexico Hydrates Research Consortium Annual Meeting, 26-27 October 2010*, University of Mississippi, Oxford, MS, 23 slides (with notes).

Abstract, Posters, and Conference Papers

Knapp, C. C.; Williams, A. Q.; Terry, D. A.; Knapp, J. H.; 2018. Three Dimensional Thermobaric Model of a Gas Hydrate System at Woolsey Mound, Northern Gulf of Mexico. AGU Annual Fall Meeting, Washington, DC, December10-14, 2018. Poster OS31F-1866.

Knapp, Camelia C.; Almutairi, Khaled; T.; Knapp, J. H.; Terry, D. A.; Brantley, D.; 2018. Carbon Storage Assessment of the Southeastern United States Outer Continental Shelf. AGU Annual Fall Meeting, Washington, DC, December10-14, 2018. Poster GH41A-1421.

Terry, D. A.; Knapp, C. C.; 2018. Application of a Unified Effective Medium Model to Gas Hydrates in Sediments. SEG Workshop, Rock Physics and Digital Rock Applications, 20-23 May 2018, Beijing, China. Poster #21.

Almutairi, Khaled F.; Knapp, Camelia; Knapp, James; Terry, Darrell; 2018. Assessment of Upper Cretaceous Strata for Offshore CO2 Storage, Southeastern United States. AAPG Annual Convention and Exhibition, Salt Lake City, Utah, May 20-23, 2018 (AAPG Datapages/Search and Discovery Article #90323©2018)

Terry, D. A.; Yankovsky, E. A; Knapp, C. C.; 2014. Cellular Convection and Methane Hydrate Systems in the Central Aleutian Basin. Eight International Conference on Gas Hydrates (ICGH-2014), Beijing, China, 28 July-1 August 2014 [Poster P4.061 and Conference Proceedings (Paper T1-186, 12 p.)].

Yankovsky, E. A.; Terry, D. A.; Knapp, C. C; 2013. Plume Structures in the Central Aleutian Basin. American Geophysical Union (AGU) Fall Meeting, San Francisco, CA, 9-13 December 2013, Abstract B33K-0617.

Terry, D. A.; Knapp, C. C.; Knapp, J. H.; 2011. Effective-Medium Models for Marine Gas Hydrates, Mallik Revisited. American Geophysical Union (AGU), Fall Meeting, San Francisco, CA, 5-9 December 2011, Abstract OS13C-1540 [Poster and Manuscript (25 pp.)].

Terry, D. A.; Knapp, C. C.; Knapp, J. H.; 2011. Effective-Medium Models and Rock Physics Analysis for Marine Gas Hydrates (In Northern Gulf of Mexico). Seventh International Conference on Gas Hydrates (ICGH), Edinburgh, Scotland, United Kingdom, 17-21 July 2011 [Poster 170 and Conference Proceedings (Paper, 9 p.)].

Terry, D. A.; Knapp, C. C.; Knapp, J. H.; 2010. Comparison of Effective-Medium Models for Marine Gas Hydrates. American Geophysical Union (AGU), Fall Meeting, San Francisco, CA, 13-17 December 2010, Abstract OS53A-1361 [Poster and Manuscript (20 pp.)].

Terry, D. A.; Knapp, C. C.; Knapp, J. H.; 2010. Implementation of Rock Physics Models for Gas Hydrates. Gordon Research Conference, Natural Gas Hydrate Systems: Hydrate-Sediment-Fluid Interactions at Pore to Regional Scale, Colby College, Waterville, Maine, 6-11 June 2010. [Poster and Manuscript (20 pp.)]

Knapp, Camelia C.; Knapp, James H.; Terry, Darrell; Addison, Adrian; Macelloni, Leonardo; Waddell, Michael; 2010. *Geophysical Baseline Characterization of Subsurface Gas Hydrates at MC118, the Gulf of Mexico*. American Association of Petroleum Geologists, Annual Convention and Exhibition, 11-14 April 2010, New Orleans.

VITA

Darrell Andrew Terry

Candidate for the Degree of

Doctor of Philosophy

Thesis: BUOYANCY DRIVEN FLOW AND METHANE HYDRATE SYSTEMS

Major Field: Geology (Marine Geophysics)

Biographical:

Education:

Completed the requirements for the Doctor of Philosophy in Geology (Marine Geophysics) at Oklahoma State University, Stillwater, Oklahoma USA in May 2019.

Completed the requirements for the Doctor of Philosophy in Mechanical and Aerospace Engineering (Fluid/Thermal Sciences) University of California, Irvine, California USA in March 2006.

Completed the requirements for the Master of Science in Aeronautics and Astronautics at University of Washington, Seattle, Washington USA in December 1976.

Completed the requirements for the Bachelor of Science in Oceanography (Physical) at University of Washington, Seattle, Washington USA in 1973.

Experience:

The Mitre Corporation
Northrop Grumman Corporation
Lockheed Martin Corporation
Raytheon Corporation
Northrop Grumman Corporation
McDonald Douglas Corporation
Los Alamos National Laboratory
Western Geophysical

Professional Memberships:

American Geophysical Union
Society of Exploration Geophysicists
IEEE Aerospace Conf.: Session Chair - Computational Modeling, 2006-2020

Patent: LIDAR Droplet Size Monitor for In-Flight Measurement of Aircraft Engine Contrails, Droplets and Aerosols, Patent No. 5546183, Granted August 13, 1996.